SANDIA REPORT
SAND2013-2735
Unlimited Release
Printed April 2013

Structural Health and Prognostics Management for Offshore Wind Turbines: Case Studies of Rotor Fault and Blade Damage with Initial O&M Cost Modeling

Noah J. Myrent, Joshua F. Kusnick, Natalie C. Barrett, Douglas E. Adams, and D. Todd Griffith

Prepared by
Sandia National Laboratories
Albuquerque, New Mexico 87185 and Livermore, California 94550

Sandia National Laboratories is a multi-program laboratory managed and operated by Sandia Corporation, a wholly owned subsidiary of Lockheed Martin Corporation, for the U.S. Department of Energy's National Nuclear Security Administration under contract DE-AC04-94AL85000.

Approved for public release; further dissemination unlimited.

Issued by Sandia National Laboratories, operated for the United States Department of Energy by Sandia Corporation.

NOTICE: This report was prepared as an account of work sponsored by an agency of the United States Government. Neither the United States Government, nor any agency thereof, nor any of their employees, nor any of their contractors, subcontractors, or their employees, make any warranty, express or implied, or assume any legal liability or responsibility for the accuracy, completeness, or usefulness of any information, apparatus, product, or process disclosed, or represent that its use would not infringe privately owned rights. Reference herein to any specific commercial product, process, or service by trade name, trademark, manufacturer, or otherwise, does not necessarily constitute or imply its endorsement, recommendation, or favoring by the United States Government, any agency thereof, or any of their contractors or subcontractors. The views and opinions expressed herein do not necessarily state or reflect those of the United States Government, any agency thereof, or any of their contractors.

Printed in the United States of America. This report has been reproduced directly from the best available copy.

Available to DOE and DOE contractors from

U.S. Department of Energy
Office of Scientific and Technical Information
P.O. Box 62
Oak Ridge, TN 37831

Telephone:	(865) 576-8401
Facsimile:	(865) 576-5728
E-Mail:	reports@adonis.osti.gov
Online ordering:	http://www.osti.gov/bridge

Available to the public from

U.S. Department of Commerce
National Technical Information Service
5285 Port Royal Rd.
Springfield, VA 22161

Telephone:	(800) 553-6847
Facsimile:	(703) 605-6900
E-Mail:	orders@ntis.fedworld.gov
Online order:	http://www.ntis.gov/help/ordermethods.asp?loc=7-4-0#online

SAND2013-2735
Unlimited Release
Printed April 2013

Structural Health and Prognostics Management for Offshore Wind Turbines: Case Studies of Rotor Fault and Blade Damage with Initial O&M Cost Modeling

Noah J. Myrent, Joshua F. Kusnick, Natalie C. Barrett, and Douglas E. Adams,
Purdue Center for Systems Integrity
1500 Kepner Dr.
Lafayette, IN 47905

D. Todd Griffith
Wind Energy Technology Department
Sandia National Laboratories
P.O. Box 5800
Albuquerque, New Mexico 87185-MS1124

Abstract

Operations and maintenance costs for offshore wind plants are significantly higher than the current costs for land-based (onshore) wind plants. One way to reduce these costs would be to implement a structural health and prognostic management (SHPM) system as part of a condition based maintenance paradigm with smart load management and utilize a state-based cost model to assess the economics associated with use of the SHPM system. To facilitate the development of such a system a multi-scale modeling approach developed in prior work is used to identify how the underlying physics of the system are affected by the presence of damage and faults, and how these changes manifest themselves in the operational response of a full turbine. This methodology was used to investigate two case studies: (1) the effects of rotor imbalance due to pitch error (aerodynamic imbalance) and mass imbalance and (2) disbond of the shear web; both on a 5-MW offshore wind turbine in the present report. Based on simulations of damage in the turbine model, the operational measurements that demonstrated the highest sensitivity to the damage/faults were the blade tip accelerations and local pitching moments for both imbalance and shear web disbond. The initial cost model provided a great deal of insight into the estimated savings in operations and maintenance costs due to the implementation of an effective SHPM system. The integration of the health monitoring information and O&M cost versus damage/fault severity information provides the initial steps to identify processes to reduce operations and maintenance costs for an offshore wind farm while increasing turbine availability, revenue, and overall profit.

CONTENTS

FIGURES

TABLES

NOMENCLATURE

AEP	annual energy production
BEM	Blade Element Momentum
BPE	Beam Property Extraction
CBM	condition based maintenance
COE	cost of energy
dB	decibel
DOE	Department of Energy
DOWEC	Dutch Offshore Wind Energy Converter Project
FAST	Fatigue, Aerodynamics, Structures, and Turbulence
FCR	fixed charge rate
FEA	Finite Element Analysis
HAWT	horizontal axis wind turbine
ICC	initial capital cost
LRC	levelized replacement cost
LSS	low speed shaft
NREL	National Renewable Energy Laboratory
NuMAD	Numerical Manufacturing and Design Tool
NWTC	National Wind Technology Center
O&M	operations and maintenance
POMDP	Partially Observed Markov Decision Process
PS	power spectrum
RMS	root mean square
SHPM	structural health prognostics management
SNL	Sandia National Laboratories
SW	shear web
TE	trailing edge
TSA	time synchronous average

EXECUTIVE SUMMARY

Offshore wind energy could potentially play a significant role in helping the U.S. obtain an energy portfolio composed of clean, renewable and diversified resources. One current obstacle to the utilization of offshore wind energy is that most projections put the operations and maintenance (O&M) costs of offshore wind farms between 2 to 5 times the current average O&M costs for onshore wind farms [1]. One way in which those costs may be reduced is through the use of a simple yet effective structural health monitoring system as part of an overall condition based maintenance paradigm. A successful health monitoring system would be able to prevent catastrophic failures, reduce or eliminate unplanned or unnecessary maintenance, and as well reduce logistic lead times and optimize supply chain management through the use of prognostics. In addition to the use of prognostics management for maintenance process improvement, potential exists to also use prognostics to increase energy capture through smart loads management; for example, by derating the turbine so that damage growth is mitigated while revenue production continues until maintenance can be performed.

A methodology has been created to aid in the development, evaluation, and optimization of a structural health and prognostics management (SHPM) system for wind turbines using physics-based simulations and state-space cost modeling. The developed scheme is a multi-scale modeling and simulation approach **[16]** that propagates the effects of damage from high fidelity local simulations to full turbine simulations using reduced order models as illustrated in Figure 1. Fault and damage detection algorithms have been developed which provide information that feeds into a cost model to compare the cost of energy (COE) between a wind farm that would use a SHPM system to optimize the maintenance schedule and a wind farm which would not use such a system. Figure 2 shows the overall approach to utilizing SHM for optimizing O&M costs and Figure 3 shows the cost model flowchart for producing levelized O&M cost savings.

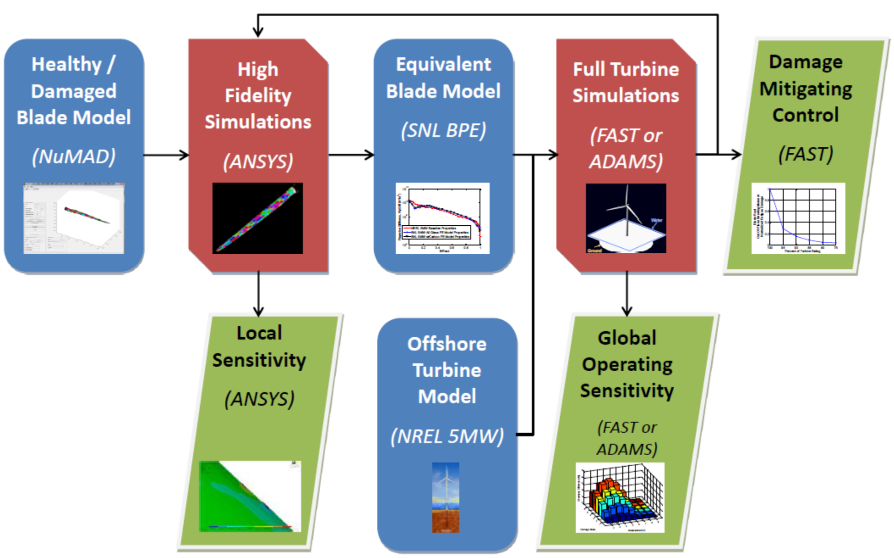

Figure 1. The multi-scale damage modeling and simulation methodology designed to aid in the development and optimization of health monitoring systems for wind turbine blades.

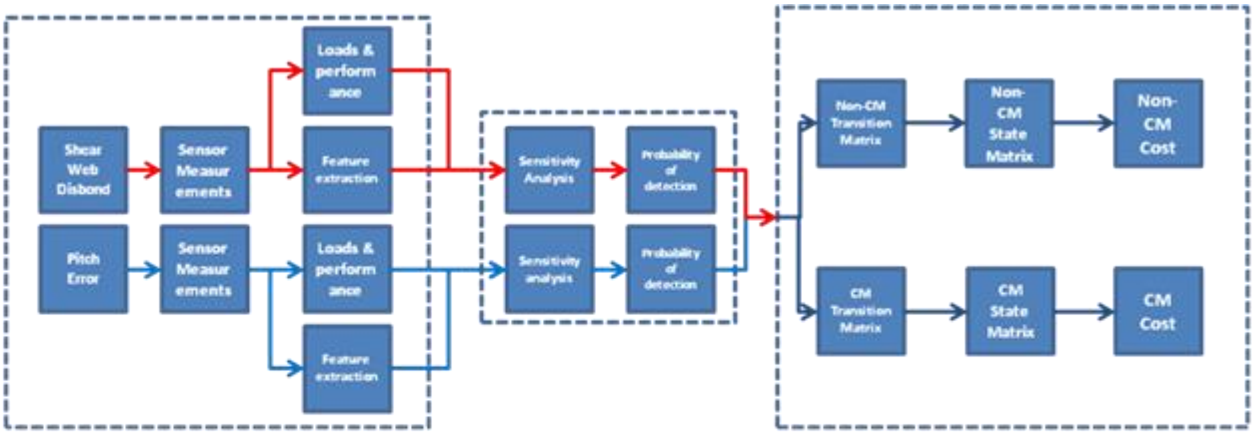

Figure 2. Overall approach for projecting COE benefits based on damage/fault detection strategies (Left Block: Operational Simulation of Damage (see Figure 1); Middle Block: Damage Sensitivity Analysis and Detection Evaluation; Right Block: Cost Analysis)

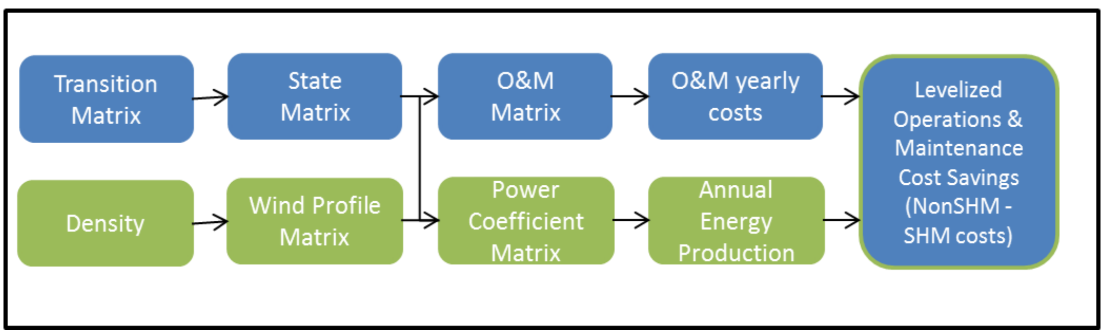

Figure 3. Cost Model Flowchart

To expand on work in FY11 [16] where we implemented the multi-scale modeling and simulation methodology and exercised the process in analyzing the effects of a trailing edge (TE) disbond, the work in FY12 was focused on the effects of a shear web (SW) disbond as well as aerodynamic and mass imbalance on a 5-MW offshore wind turbine. Local analyses based on linear loads analysis of high-fidelity blade finite element models due to laminar aerodynamic loading indicated that the SW disbond resulted in; for example, small increases in blade tip deflection as shown in Figure 4. In global simulations of the full turbine aeroelastic model incorporating the simplified blade structural model, blade tip accelerations and root pitching moments proved to be good indicators of an imbalance and/or SW disbond (Figures 5, 6). Although tip deflection is not sensitive to the presence of a shear web disbond, this damage mechanism affects the operational response of the turbine significantly. **The simulations results illustrated the benefit of the multiscale modeling approach for detection of rotor imbalances and shear web disbonds and the usefulness of this multi-scale approach to resolve the effects of damage as they are manifested as localized damage in the blade structure and global signatures in the operational sensor measurements.**

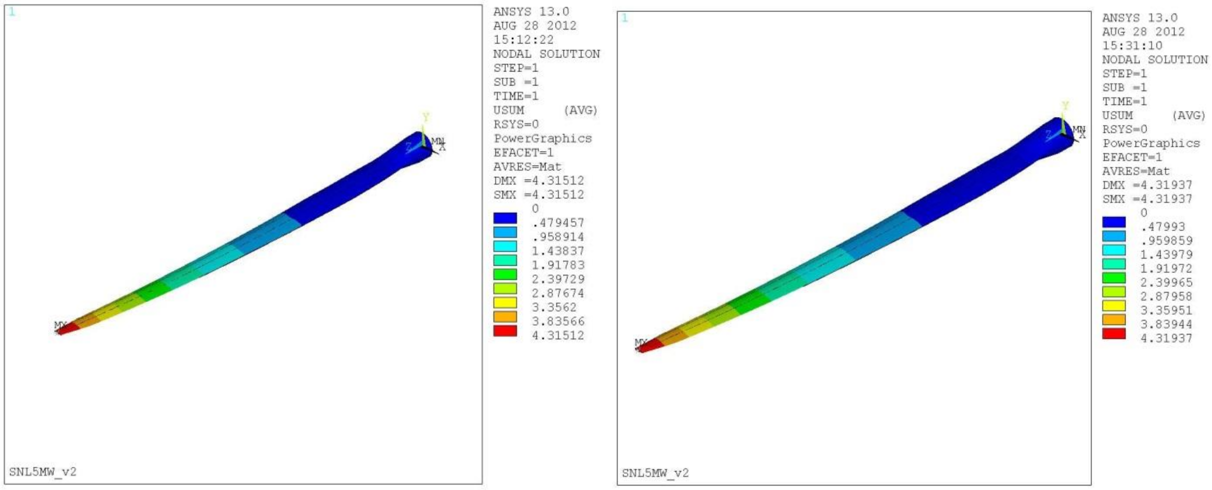

Figure 4. Blade deflection results for healthy blade (left) and blade with 5 meter shear web disbond originating at max chord (right)

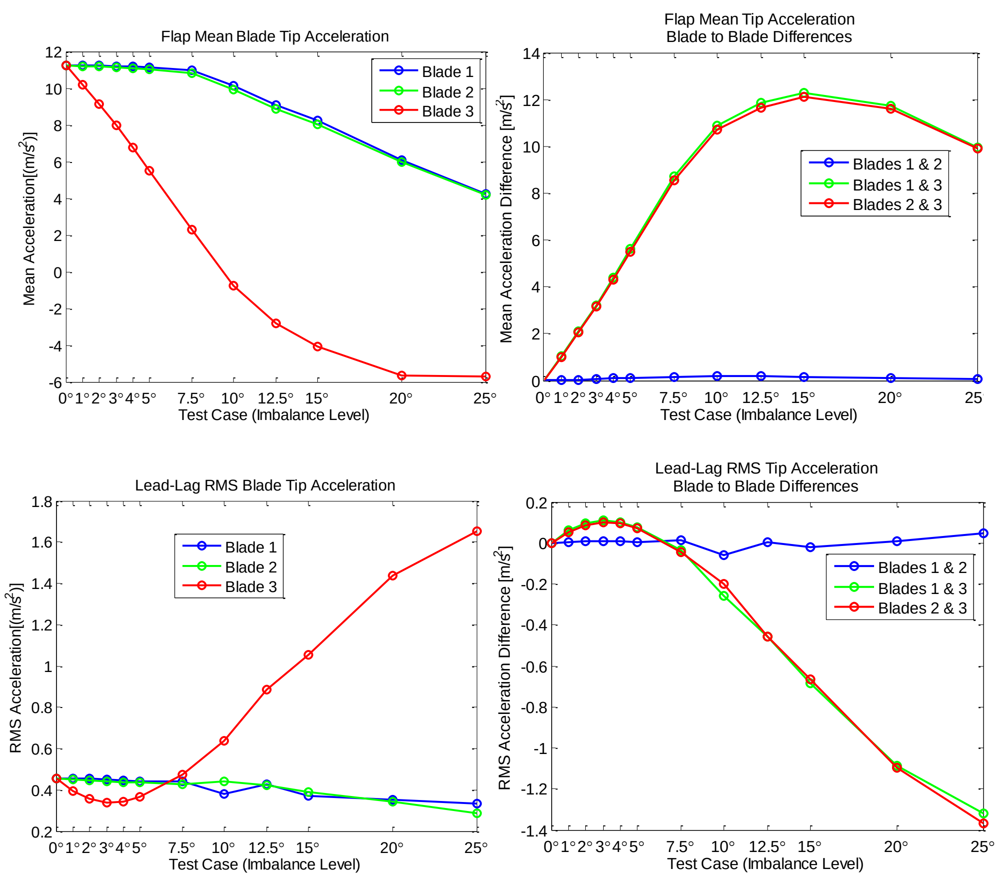

Figure 5. Flapwise and edgewise blade tip accelerations and blade-to-blade differences for pitch error.

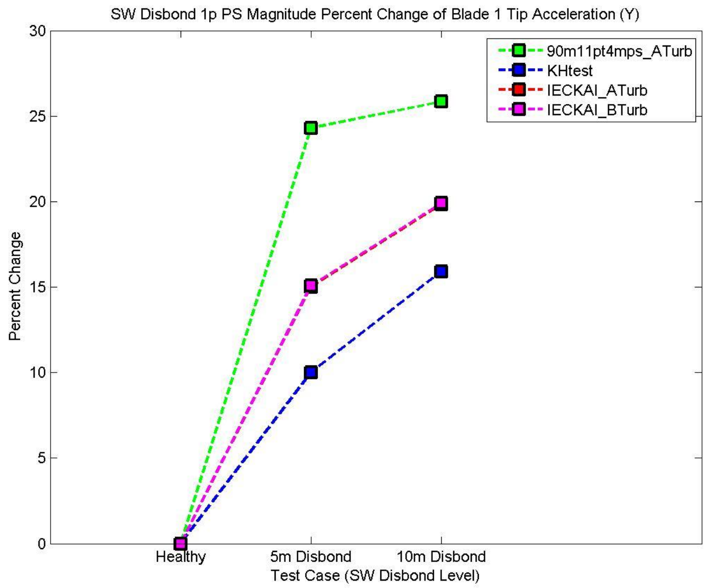

Figure 6. 1p magnitude percent change of edge-wise blade tip acceleration for shear web disbond for four different inflow conditions

A state-based cost model was developed to quantify the effect of a SHPM system on O&M costs. The cost sensitivity analysis shows that O&M COE is most sensitive to the O&M repair and replacement costs. The next most sensitive factor is the extent of damage (i.e. point at which the blade is repaired). Finally, of the factors evaluated in this initial cost sensitivity study, the O&M COE is the least sensitive to changes in the performance coefficient (rotor power coefficient). Figure 7 shows the base model of the cost savings as a result of implementing a SHPM system for the detection of a mass imbalance and/or shear web disbond.

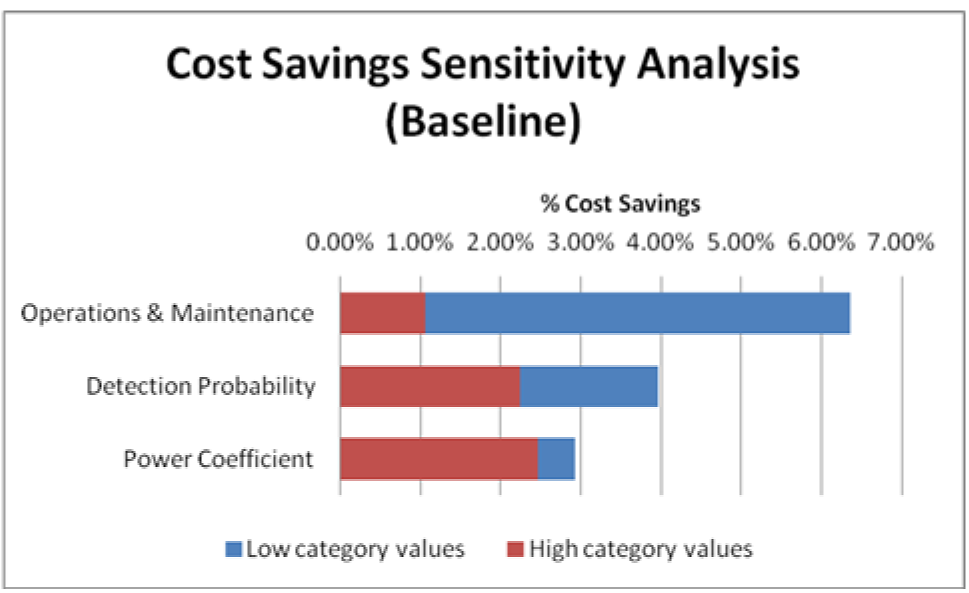

Figure 7. Cost savings sensitivity analysis for the proposed SHPM system.

1. INTRODUCTION

Offshore wind energy in the United States is an untapped energy resource that could play a pivotal role in helping the U.S. obtain an energy portfolio composed of clean, renewable and diversified resources. Some of the drivers for the utilization of offshore wind include the proximity of the offshore resources to population centers and the potential for higher capacity factors due to higher resource winds [1]. Because of these drivers and other potential benefits of offshore wind, the Offshore Wind Innovation and Demonstration initiative has developed an ambitious goal of deploying 10 GW of offshore capacity by 2020 at a cost of energy of only $0.10/kWh [2].

1.1. Drivers for Offshore SHPM

As of June 2011, while nine offshore projects totaling over 2 GW of capacity were in various stages of the permitting and development process, no offshore wind energy projects had been installed in the United States [4]. Part of the reason for this lack of development is that operations and maintenance (O&M) costs are expected to be significantly higher for offshore wind turbines than onshore wind turbines. Recent projections of O&M costs have ranged between $11 and $66 U.S. dollars per megawatt-hour with the majority of estimates being between 2 to 5 times the cost of land-based (onshore) O&M [1]. These higher O&M costs represent a larger overall proportion of the cost of energy than for onshore turbines even when the large initial investment required for the installation of offshore turbines is included [5]. One of the reasons that O&M costs are likely to be higher offshore is that the offshore environment will bring with it increased loading which is relatively uncharacterized due to the lack of existing offshore installations. Offshore turbines will also have to be built to withstand the environmental harshness of the offshore environment. Lastly, access to the turbines will be difficult, costly, and occasionally not possible due to high sea states [1,8].

1.2. SHPM Benefits

One potential way in which these O&M costs could be addressed is through the use of a structural health and prognostics management (SHPM) system as part of a condition based maintenance (CBM) paradigm [6-12]. By continuously monitoring the health, or condition, of structural components in each wind turbine, required maintenance actions can be scheduled ahead of time and performed when they are needed rather than on a preset schedule or only after failure has already occurred. The benefits of a CBM strategy are expected to include less regular maintenance, the avoidance or reduction of unscheduled maintenance and improved supply chain management [8-11].

Furthermore, because wind turbines are active systems, monitoring the health of wind turbine components will allow for smart turbine load management to optimize the profit of the entire wind plant. For example, if a turbine blade becomes damaged and that damage is detected at an early stage by the SHPM system, the turbine could be derated so that small less costly repairs could be performed on the turbine. While this action would reduce the amount of power generated by the turbine in the short-term, it may allow for less extensive maintenance actions to be performed, permit additional energy capture while maintenance is being planned, extend the overall life of the turbine, and allow for multiple turbines to be serviced during the same visit to maximize the overall profit of the wind power plant.

1.3 Summary of Prior Work in Wind Turbine Rotor SHPM Development

Although the fields of structural health monitoring and prognostics management are fairly rich in general, research in application to wind turbine rotor blades in either field is somewhat limited. Integration of the two disciplines is even more limited. Sandia has had an active program for several years to investigate sensored blades with several blade-build and field testing demonstration projects. Blades for utility-scale wind turbines typically have no sensors in the blades, but if they do they have been limited to strain gauges in the blade root. The Sandia research involved embedding sensors along the entire blade span, which included acceleration, strain, and temperature sensors. The proposed applications for this "enhanced" blade sensing capability include structural health monitoring and active control of the rotor. These Sandia studies provided some important lessons learned regarding manufacturing of sensors into blades and selection of sensors.

In an effort to map out the SHPM problem and also provide an example case study, an initial roadmap was developed by Sandia National Laboratories for a combining structural health monitoring and prognostics assets into a SHPM system with application to wind turbine rotor blades as documented in Reference 16. The key element established in this initial roadmap, the so-called multi-scale damage modeling and simulation methodology, addresses both how damage is modeled at multiple resolutions of the model and also the resulting manifestation (or effects) of damage in both the global operating dynamic response and the localized effects related to remaining life (state of health). The intent of this approach is to combine structural health monitoring and prognostic management so as to bridge the gap between being able to detect and characterize the presence of damage and then being able to make revenue-optimizing operations and maintenance decisions.

This report provides the results for a few additional case studies. The aim of these studies is to provide some additional information to mature the SHPM technology development for wind turbine rotors. The key elements addressed in the report include an assessment of operating sensitivity of damage to additional damage/fault mechanisms and development/evaluation of an initial O&M cost model.

2. THE APPROACH: COMBINING SHM SYSTEM PERFORMANCE AND COST ANALYSES

To quantify the benefits of implementing an offshore structural health and prognostics management system, a multi-model methodology was developed that combines an evaluation of SHPM system performance with state-of-health based cost analysis. The approach permits an evaluation of O&M scenarios (O&M strategies) to identify; for example, turbine conditions strongly influenced by particular fault or damage mechanisms, detection strategies based on various measurement analysis approaches tailored for a wind turbine system, and project operations and maintenance costs with and without such a condition monitoring system. Figure 8 shows the overall approach.

The left-most block in Figure 8 describes modeling of the turbine and damage simulations. The middle block describes the sensitivity analysis performed on the operating response of the turbine including an assessment of sensors and their performance in detecting the modeled damage. The right-most block in Figure 8 describes the cost analysis for the SHPM system. The approach starts with simulations of turbines with damage then the operational response from these simulations is fed to the middle block were the data is analyzed via sensitivity of damage studies. This middle block addresses the performance of the SHPM system to identify which sensors are viable options to detect damage and also to quantify the ability to detect damage (i.e. probability of detection). State of health information and SHPM performance information is fed to the right-most block where SHPM economics is assessed. This concept should prove useful in assessing both performance and cost of SHPM system, and in the future it could prove useful in design of the SHPM system and in evaluation of SHPM return of investment. This approach could also be applied in real-time operation such that information from the right-most economics module could feedback to the turbine operator or turbine control system for decision making.

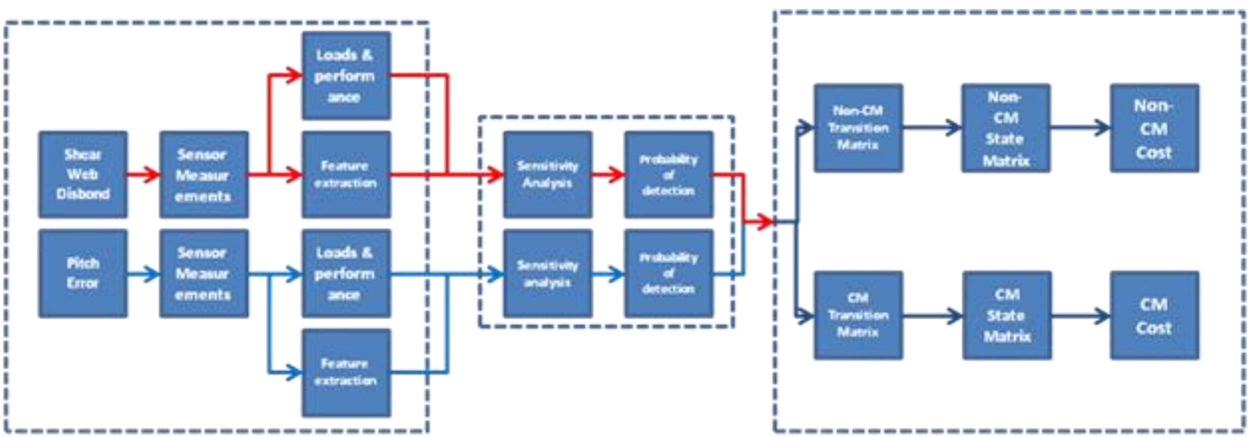

Figure 8. SHPM system feasibility quantification concept approach

Utilization of simulations is a cost-effective method to investigate the sensitivity of many different potential measurements and measurement locations while controlling/eliminating variability from sources other than the damage or fault that is being studied. The simulation approach of this work used high fidelity blade and damage models to represent the influence of damage. This model was then reduced to an equivalent blade model of sufficient resolution to capture the influence of the damage while still being able to be integrated into simulations of a full offshore wind turbine operating under various inflow conditions. In addition to the analysis of the results from these full turbine simulations, the loads from these simulations can then be fed back into the high fidelity blade model so that localized damage sensitivity measures or effects can be obtained.

In order to perform the desired simulations, a variety of different software packages were integrated in order to obtain the results of interest. Sandia National Laboratories' (SNL's) NuMAD software was used to create a high fidelity blade model in the software package ANSYS. A shear web disbond was then created in the model and equivalent beam parameters were extracted which could be integrated with a turbine model for simulations of the damaged turbine in either FAST [13] or MSC.ADAMS [14]. Results from each stage of this modeling process were then used to assess the influence of the damage on the response of the blade and the turbine as a whole and to identify a subset of measurements that could prove beneficial for future SHPM investigations.

The cost model used for this study is a state-space Matlab model that calculates O&M costs ($/MWh) of a wind turbine for scenarios such as a turbine with and without an enhanced blade condition monitoring system. In the initial model, four states are defined in the cost model that correspond to different extents of damage and the associated different types of maintenance that would be required in each state; for example, state 1 is associated witha blade in a new or repaired condition and at the other extreme state 4 would be associated with a blade damaged to the point beyond which it can be repaired and must be replaced.

3. 5-MW OFFSHORE TURBINE MODEL

3.1. Turbine Model Description

As part of an ongoing structural health and prognostics management project for offshore wind turbines, the simulations in this report were performed using a representative utility-scale wind turbine model. The model, known as the NREL offshore 5-MW baseline wind turbine model, was developed by NREL to support studies aimed at assessing offshore wind technology [15]. It is a three-bladed, upwind, variable-speed, variable blade-pitch-to-feather-controlled turbine and was created using available design information from documents published by wind turbine manufacturers, with a focus on the REpower 5-MW turbine. Basic specifications of the model configuration are listed in Table 1.

Table 1. Gross Properties of the NREL 5-MW Baseline Wind Turbine [16].

Property	Value
Rating	5MW
Rotor Orientation, Configuration	Upwind, 3 blades
Control	Variable Speed, Collective Pitch
Drivetrain	High Speed, Multiple-Stage Gearbox
Rotor, Hub Diameter	126 m, 3 m
Hub Height	90 m
Cut-in, Rated, Cut-out Wind Speed	3 m/s, 11.4 m/s, 25 m/s
Cut-in, Rated Rotor Speed	6.9 rpm, 12.1 rpm
Rated Tip Speed	80 m/s
Overhang, Shaft Tilt, Precone	5m, 5°, 2.5°
Rotor Mass, Nacelle Mass, Tower Mass	110,000 kg; 240,000 kg; 347,460 kg
Water Depth	20 m
Wave Model	JONSWAP/Pierson-Moskowitz Spectrum
Significant Wave Height	6 m
Platform	Fixed-Bottom Monopile

A new blade model was developed to be used with the NREL 5-MW turbine model, which is the same model used in the initial studies (Ref). A detailed blade model did not exist and was needed so that damage could be introduced into the blade structure within the multi-scale modeling and simulation framework (as described above). The detailed blade model was developed by Sandia National Laboratories using blade geometry data from the Dutch Offshore Wind Energy Converter Project (DOWEC) and composite layup information from the European Union's UpWind program. The distribution of material layers along the blade span is illustrated in Figure 9.

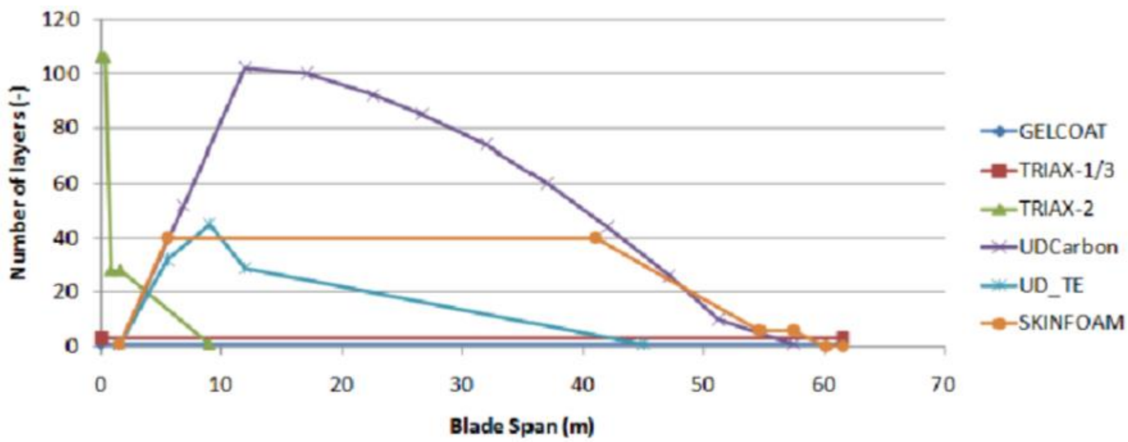

Figure 9. Model of the Distribution of Material Layers along the Span of the Blade, (Griffith, et al. 2011).

Two thirds of the blade span utilizes the TU-Delft family of airfoils, while the final one-third of the blade span utilizes the NACA 64-series airfoils. Intermediate airfoil shapes were developed that preserve the blending of camber lines as well as a smooth blade thickness profile. Figure 10 shows the finite element model of the blade in ANSYS with the colored sections representing different composite materials. This high degree-of-freedom model was translated into a model consisting of several beam elements using Sandia's Blade Property Extraction tool (BPE). BPE works by applying loads in each of the six degrees of freedom at the tip of the blade model in ANSYS, then processing the resulting displacements at selected nodes along the blade to generate the 6x6 Timoshenko stiffness matrices for the beam discretization. This reduced degree-of-freedom model is subsequently used to define the blade properties in FAST. For a more detailed description of BPE, see [16].

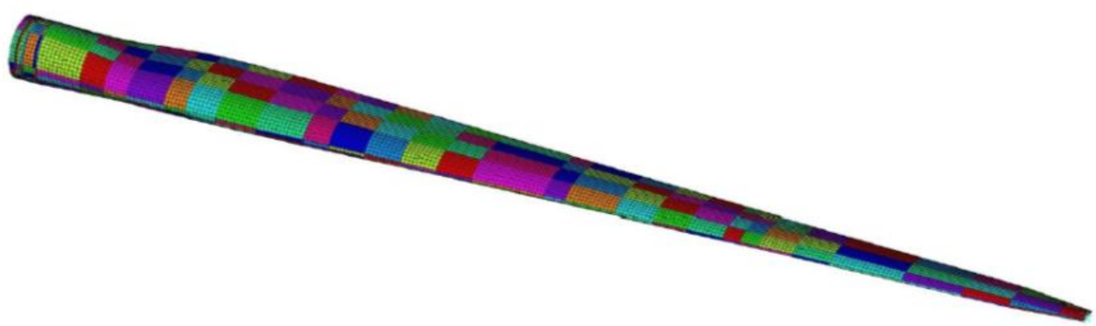

Figure 10. ANSYS finite element mesh for the 5-MW blade model.

3.1.1. *FAST Simulation Turbine Coordinate Systems*

FAST uses six coordinate systems for input and output parameters. Some of these coordinate systems will be referred to throughout this report, so they are reproduced here from the FAST User's Guide for convenience. Note that the FAST User's Guide coordinate system images use a downwind turbine configuration; however, the same coordinate systems apply in the case of the upwind turbine being referred to in this work, but the orientation of the x axis changes so that in either configuration it is pointing in the nominally downwind direction. The rotor shaft coordinate system is shown in Figure 11. This coordinate system does not rotate with the rotor, but it translates and rotates with the tower and yaws with the nacelle. In addition to output variables related to the low speed shaft, the nacelle inertial measurements also use this coordinate system. Some shaft outputs, such as shear force in the low speed shaft, are measured in both a non-rotating coordinate system and a rotating coordinate system; these are differentiated by using an "s" or "a" subscript, respectively. The tower base coordinate system shown in Figure 12 is fixed in the support platform, thus rotating and translating with the platform. The tower-top/base-plate coordinate system shown in Figure 13 is fixed to the top of the tower. It translates and rotates with the motion of the platform and tower top, but it does not yaw with the nacelle.

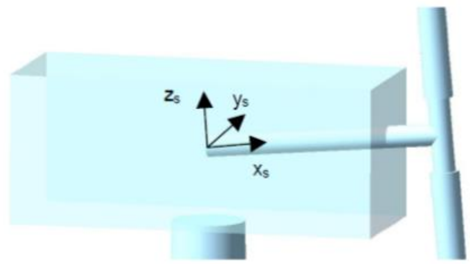

Figure 11. Shaft Coordinate System (Jonkman and Buhl 2005).

Figure 12. Tower Base Coordinate System (Jonkman and Buhl 2005).

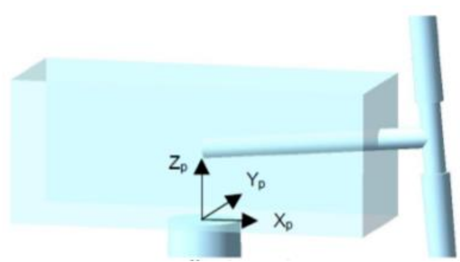

Figure 13. Tower-top/base-plate coordinate system (Jonkman and Buhl 2005).

4. ROTOR MASS/AERODYNAMIC IMBALANCE SENSITIVITY STUDY

4.1. Introduction

In order to evaluate the applicability of the pitch error detection method discussed in Section 4.7 on larger utility-scale wind turbines, computer simulations were carried out using the 5-MW turbine model described in Section 3.1. Modeling was performed using NREL's Fatigue, Aerodynamics, Structures and Turbulence (FAST) code, which is a comprehensive aeroelastic simulator for two and three-bladed horizontal axis wind turbines (HAWTs). The code provides the means to manipulate a variety of input parameters, including turbine control settings, environmental conditions, blade and tower models, drivetrain and generator parameters, and many others. There are also hundreds of possible outputs, including blade inertial measurements and generator power.

FAST uses AeroDyn to calculate the aerodynamics of HAWTs. AeroDyn is an aeroelastic simulation code which uses several subroutines for wind turbine applications, including the blade element momentum theory, the generalized dynamic-wake theory, the semi-empirical Beddoes-Leishman dynamic stall model, and a tower shadow model. The FAST model combines a modal and multibody dynamics formulation, and performs a time-marching analysis of the nonlinear equations of motion. For a more detailed description of the working principles of the code, see the FAST User's Guide [17].

Imbalance of the rotor can occur for a number of reasons, although the imbalance can generally be divided into two categories: mass imbalance or an aerodynamic imbalance. Pitch error is a common problem that fits into a more general class of turbine faults referred to as aerodynamic asymmetries. This means that the individual blades are not generating the same thrust and tangential forces when subjected to the same wind profile. Other reasons this can occur are blade profile differences as a result of manufacturing tolerances, blade surface roughness changes, and degradation or damage to a blade, such as tip delamination, erosion, or deformation of the structure. Since the effects of aerodynamic asymmetries are closely related to rotor mass imbalances and information to-date indicates that 20% of utility-scale wind turbines have a mass or aerodynamic imbalance [18], both types of imbalances were simulated in this work. Mass imbalances result from inhomogeneous mass distributions in the blades caused by manufacturing, water inclusions, icing, and loose material from manufacturing moving inside the blade towards the tip during rotation [19]. Existing or proposed imbalance detection methods in wind turbines use inertial measurements in the nacelle. However, there are difficulties using this method which are illustrated using a simplified rotor dynamics model in the next section. Therefore, several methods of detection were evaluated in order to compare the use of blade and non-blade measurements, and a detection algorithm was proposed and summarized in a flow chart in Section 4.7.

4.2. Simplified Rotor Dynamics Model

In order to demonstrate the dynamics effects at the nacelle, consider the simplified model formulated by [20]. To start, the mass imbalance of the rotor is modeled as a point mass *m* located in the rotor plane at a distance *r* from the center of rotation, O, and an angle ϕ_m from the zero mark of blade A, as shown in Figure 14. This is the typical setup for a static unbalance, which is defined as the eccentricity of the center of gravity of a rotor caused by a point mass located a specified radial distance from the center of rotation. Correcting a static unbalance requires placing a point mass of equal magnitude in the rotor plane, diametrically opposed to the unbalance mass. Dynamic imbalance on the other hand acts like an equivalent radial co-rotational moment fixed in the rotor [21]. Physically this means that the direction of the angular momentum vector is changing as the rotor rotates, and a rotor is dynamically balanced only if its angular velocity vector points along one of its principal axes of mass distribution [22, 23]. Correcting a dynamic imbalance requires balancing the rotor in two axial planes. A general rule of thumb; however, is that a rotor with bladed diameter that is more than 7 to 10 times its width is treated as a single-plane rotor [24]. This is certainly true for horizontal axis wind turbines, and therefore this work will only consider static mass imbalance. The blades in the simplified rotor dynamics model are separated by an angle φ and ϕ is the angle between blade A and the x axis. The rotor spins with angular velocity ω, therefore the point mass m generates a centrifugal force, F_c, with magnitude:

$$F_c = m\omega^2 r. \tag{1}$$

There will also be a gravitational load P due to the mass imbalance, but this load and its associated moments about the tower will be considered small relative to the centrifugal load and will be neglected. If a time variable, *t*, is introduced, then $\omega t = \phi$, and the projection of the centrifugal force onto the x and z axes are:

$$\begin{aligned}(F_c)_z &= F_c \sin(\omega t + \phi_m) \\ (F_c)_x &= F_c \cos(\omega t + \phi_m).\end{aligned} \tag{2}$$

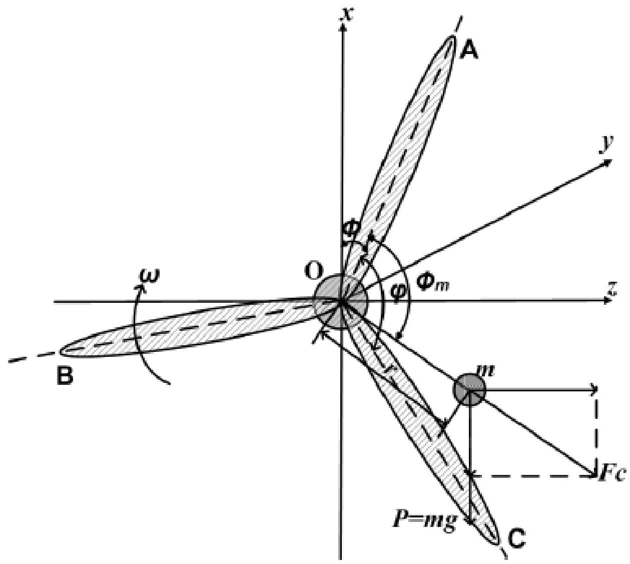

Figure 14. Mass imbalance model (Niebsch, Ramlau and Nguyen 2010).

The plane of rotation is located a distance L along the y-axis from the turbine's tower, therefore the forces $(F_c)_z$ and $(F_c)_x$ also create moments about the x and z axes centered on the tower, given by equation (3):

$$M_x^1 = (F_c)_z \cdot L$$
$$M_z^1 = (F_c)_x \cdot L. \tag{3}$$

The aerodynamic imbalance is modeled using an equivalent load formulated from the Blade Element Momentum (BEM) theory. BEM is a commonly used method for determining aerodynamic loads on a blade. The blade is divided into a finite number of elements in the radial direction, and the lift and drag forces are approximated at each radial position using the lift and drag coefficients of the two-dimensional airfoil profile. The local pitch angle, θ, for each element can be defined as the angle between the chord-line and the plane of rotation, as shown in Figure 15.

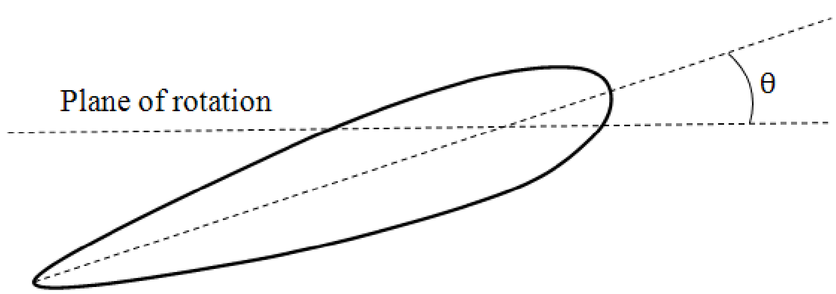

Figure 15. Local pitch angle.

The local pitch angle, θ, is a sum of the blade pitch angle at the root, θ_p, commanded by the turbine's control system, and the blade twist angle, β, at the blade element:

$$\theta = \theta_p + \beta. \qquad (4)$$

Calculating the tangential and thrust (normal to the rotor plane) forces at each blade element results in force distributions along the blade. The distributed load can be rewritten as a single equivalent thrust force and single tangential force on each blade, as shown in the example of Figure 16. The distributed load is denoted by *f(x)*, and the blade elements are of width *dx*. Integrating the differential forces *df* along the length of the blade, *R*, results in the equivalent load, *F*:

$$F = \int_0^R df = \int_0^R f(x)dx. \qquad (5)$$

The location *l*, where the equivalent load acts, is found using a moment balance: the total moment of all of the differential forces, *df*, about the root of the blade, *x* = 0, must equal the moment of *F* about the same point. Therefore, *l* is found with equation (6):

$$F \cdot l = \int_0^R x df = \int_0^R x f(x)dx. \qquad (6)$$

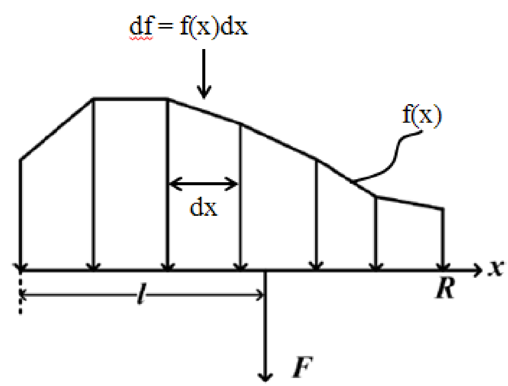

Figure 16. Equivalent Blade Point Loads (Niebsch, Ramlau and Nguyen 2010).

Thus, the aerodynamic forces can be modeled as three thrust forces and three tangential forces, one pair from each blade, as shown in Figure 17.

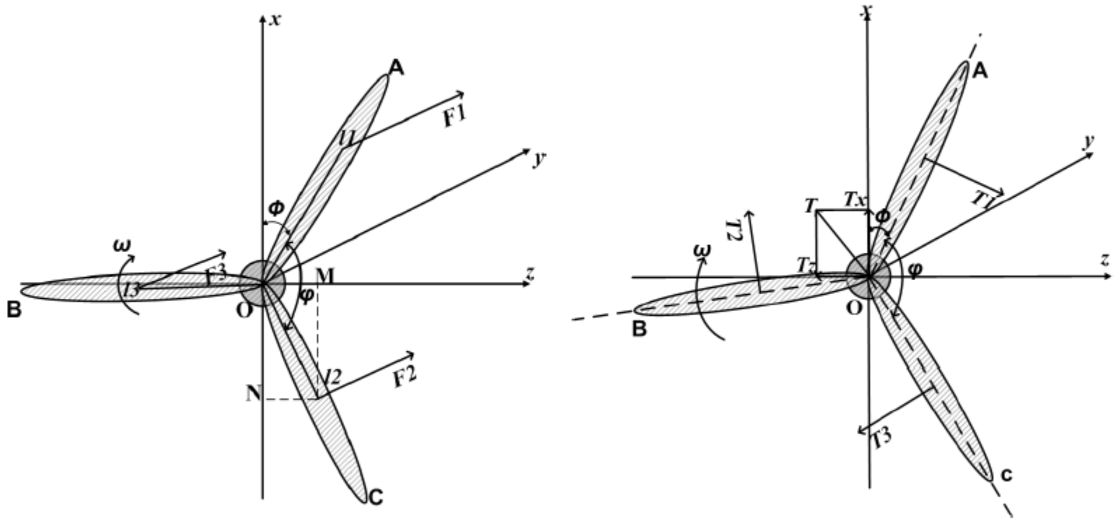

Figure 17. Equivalent blade thrust forces (Left); Equivalent blade tangential forces (Right) (Niebsch, Ramlau and Nguyen 2010).

The aerodynamic forces also generate moments about the x and z axes centered on the rotor, which are given by:

$$\begin{aligned} M_x^{\ 2} &= F_1 l_1 \sin(\omega t) + F_2 l_2 \sin(\omega t + \varphi) + F_3 l_3 \sin(\omega t + 2\varphi) \\ M_z^{\ 2} &= F_1 l_1 \cos(\omega t) + F_2 l_2 \cos(\omega t + \varphi) + F_3 l_3 \cos(\omega t + 2\varphi), \end{aligned} \tag{7}$$

where φ=120° for a three-bladed rotor. Furthermore, the tangential forces can be projected onto the x and z axes, yielding the following equations:

$$\begin{aligned} T_z &= T_1 \cos(\omega t) + T_2 \cos(\omega t + \varphi) + T_3 \cos(\omega t + 2\varphi) \\ T_x &= T_1 \sin(\omega t) + T_2 \sin(\omega t + \varphi) + T_3 \sin(\omega t + 2\varphi). \end{aligned} \tag{8}$$

These forces also produce moments about the x and z axes centered on the tower as a result of the distance L between the rotor plane and the tower center which are shown in the following equations:

$$\begin{aligned} M_x^{\ 3} &= T_z \cdot L \\ M_z^{\ 3} &= T_x \cdot L. \end{aligned} \tag{9}$$

Note that if all of the blades are identical (i.e. have the same airfoil profile), and have the same pitch angle, then $F_1 = F_2 = F_3$ and $l_1 = l_2 = l_3$, which means that the torques M_x^2 and M_z^2 are equal to zero. Finally, summing the forces and moments at the nacelle are shown in the following equations:

$$
\begin{aligned}
F_y &= F_1 + F_2 + F_3 \\
F_z &= T_z + (F_c)_z \\
M_x &= M_x^{\,1} + M_x^{\,2} + M_x^{\,3} \\
M_z &= M_z^{\,1} + M_z^{\,2} + M_z^{\,3}.
\end{aligned}
\tag{10}
$$

It is evident from equations (7) through (10) that mass and aerodynamic imbalances contribute to the same moments and forces measured in the nacelle, and the fundamental frequency of that forcing function is ω, the rotational speed of the rotor, denoted 1p (once per revolution) in the order domain. Many of the recommended imbalance condition monitoring systems, which use accelerometers located in the nacelle to measure the transverse and axial (z- and y-directions in shown in Figure 11, respectively) accelerations, attribute 1p transverse responses to mass imbalance and the 1p axial and M_x responses to aerodynamic asymmetries [19, 25]. However, this analysis shows that those responses are coupled to both types of imbalances. Thus, in this work we also consider that blade response measurements also be used to detect and characterize imbalance. These methods are compared to the nacelle measurement based methods presented in the literature in sections 4.4 and 4.5.

4.3. Imbalance Simulation Methods

To eliminate possibilities of some confounding variables such as yaw error and to study the effects of aerodynamic asymmetries and mass imbalances alone, simulations were carried out in a unidirectional, constant-speed, vertically sheared wind environment, rather than using the random and turbulent wind input conditions that are also available as inputs in FAST. The wind direction was oriented at 0°, directly perpendicular to the rotor plane, and the yaw degree of freedom was turned off in the FAST input file. The wind speed was set to 11 m/s, with a 1/7 power law vertical shear profile. Setting the wind speed to just below the rated speed of 11.4 m/s ensured that in the case of pitch error of a single blade, the two actively-pitching blades would always pitch to zero degrees to maximize the power output of the turbine, thus keeping those variables constant. The sample time spacing was set to 0.01 seconds, corresponding to a sample rate of 100 Hz. Because the per-revolution harmonics were mainly of interest and the maximum rotor speed was 12.1 rpm, or 0.2 Hz, this sample rate was sufficient. Simulations were conducted in three phases: (1) aerodynamic asymmetries, (2) mass imbalances, and (3) simultaneous aerodynamic and mass imbalances. The simulation methods for each of the phases are detailed in sections 4.3.1 through 4.3.3. Two hundred output variables were recorded from the simulations, including generator power, low speed shaft torque, tri-axial blade accelerations along the span, nacelle accelerations, and many others for use in the sensitivity of damage/fault studies.

4.3.1. *Pitch Error Simulation Methods*

While aerodynamic asymmetries can also be caused by blade profile differences and damage, this work focused on the problem of pitch error in a single blade, as discussed in the previous chapter. Initial and final pitch positions for individual blades are user-defined input parameters in the FAST primary input file, as well as the simulation times at which the blades reach those positions. It is possible to adjust these settings for a single blade while allowing the other two blades to actively pitch. To allow the rotor to reach its steady state operating speed within the first 30 seconds of simulation time, blade three, the blade with simulated pitch-error, was gradually adjusted from the start of the simulation to reach its final pitch error position after 15 seconds had elapsed. The first 30 seconds of simulations were discarded in analyzing the data to remove startup transients from the analysis – the FAST User's Guide recommends at least five seconds (Jonkman and Buhl 2005). The total simulation time for each test, eliminating the first 30 seconds, was ten minutes, allowing for averaging to take place. With all other variables remaining constant, tests were conducted with the pitch angle of blade three set to 0°, 1°, 2°, 3°, 4°, 5°, 7.5°, 10°, 12.5°, 15°, 20°, and 25°.

4.3.2. Rotor Mass Imbalance Simulation Methods

In this phase of simulation, a rotor mass imbalance was applied by increasing the mass density of blade three at a particular blade span-wise section in the FAST blade input file. The magnitudes of the mass imbalances chosen were based on two references. The first is the acceptable residual imbalance method employed by Pruftechnik Condition Monitoring GmbH, a German company which performs field-balancing of wind turbine rotors [18]. This company applies a fairly standard field balancing procedure: initial vibration measurements are taken from within the nacelle, a trial mass is added to the rotor and its effects are measured, and the balancing software then determines suggested balancing weights and locations. A detailed explanation of the general rotor balancing procedure and calculations can be found in Bruel & Kjaer's application notes [24]. Pruftechnik quantifies the permissible residual imbalance based on the standard DIN ISO1940-1: Mechanical Vibration – Balance Quality Requirements for Rotors in a Constant (Rigid) State – Part 1: Specification and Verification of Balance Tolerances. This standard provides permissible residual imbalance levels in the rotor, with different quality grades, G, depending on the application. The imbalance magnitude is found using the rotor's operational speed, rotor weight, and the balancing radius, which is the span location of the mass imbalance. Plots in the standard provide the permissible imbalance in gram-mm/kg which are based on the rotor speed and G grade. Alternatively, these curves can be written in the equation form [26]:

$$U_{per}(g-mm) = 9549 \cdot G \cdot \frac{W}{N}, \tag{11}$$

where U_{per} is the permissible residual imbalance in g-mm, G is the balance quality grade, N is the operating speed of the rotor in rpm, and W is the rotor weight in kg. Based on experience, Pruftechnik uses balancing grade G16. Sample calculations from their literature are shown in Figure 18 and equation (12).

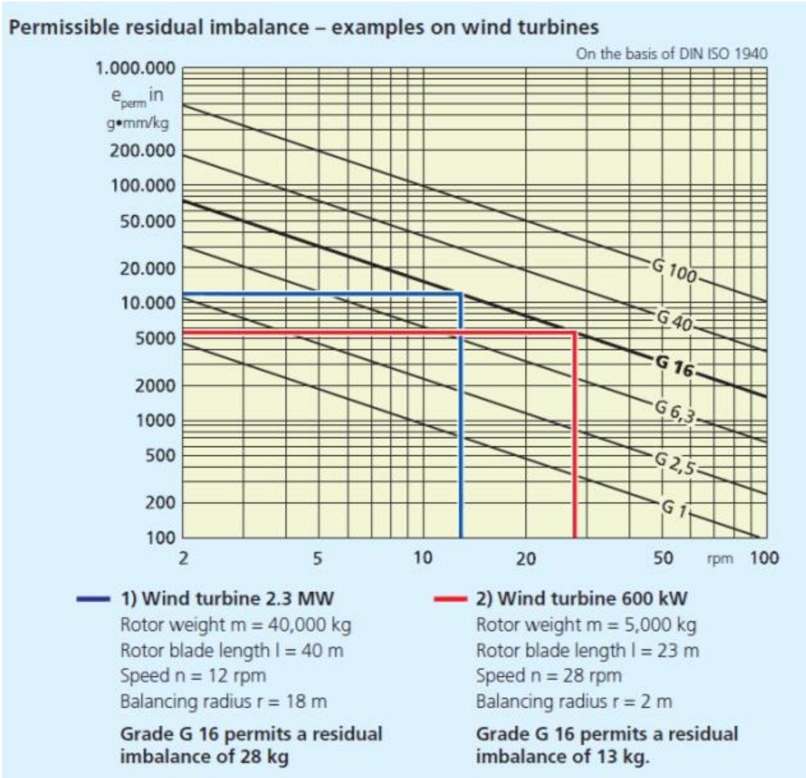

Figure 18. Permissible Residual Imbalance Examples (Losi and Becker 2009).

For the 2.3 MW turbine case, the permissible residual imbalance at 18 meters with quality grade 16 is calculated as follows:

$$U_{per} = 9549 \cdot 16 \cdot \frac{40,000kg}{12rpm} \cdot \frac{1kg \cdot m}{10^6 g \cdot mm} \cdot \frac{1}{18m} = 28kg. \tag{12}$$

Note that a conversion factor of 10^{-6} was added to convert the result for U_{per} from g-mm to kg-m, and that result was further divided by the balancing radius of 18 meters so that the output would be a mass, rather than mass times distance. The 28 kg result represents the maximum additional mass that could be added to the rotor at a distance of 18 meters from its center without exceeding the G16 quality grade.

A second source for determining mass imbalance testing levels was Moog Incorporated's fiber-optic based rotor monitoring system, which claims imbalance detection down to 0.5% of the total blade mass of all three blades [27]. For consistency and ease of comparison, it will be assumed that this imbalance is acting at the mass center of a single blade, and it will be translated to an ISO1940-1 G quality grade.

The FAST blade input file for the Sandia National Laboratories's blade model contains 23 section locations for specifying section properties. However, for computational purposes, the 23 locations are interpolated down to 17 nodes as specified in the AeroDyn input file for application of the aerodynamic forces in FAST. Therefore, the following procedure was followed to ensure that mass imbalance specified in the 23-section FAST blade input file would result in the intended G grade after interpolation:

1.) A MATLAB script was written to apply the same piecewise linear interpolation found in FAST's FORTRAN source code. The accuracy of the code was verified by adjusting the FAST input blade properties and comparing the output of the script to the interpolated blade properties that are output from FAST.

2.) The mass density of one or more of the 23 blade sections was altered and the interpolated blade section properties were then computed by the script.

3.) The script determined which interpolated blade sections incurred mass density changes compared to the interpolated properties of the unaltered blade.

4.) The effective span-wise location of the added mass was computed using a moment balance as follows in equation (13):

$$R_{eff} = \frac{\sum_{i=1}^{N} (dm)_i \cdot (dr)_i \cdot r_i}{\sum_{i=1}^{N} (dm)_i \cdot (dr)_i}, \tag{13}$$

where R_{eff} is the effective span-wise location of the added mass, N is the number of blade sections, $(dm)_i$ is the change in mass density of blade section *i* in kg/meter, $(dr)_i$ is the length of the i^{th} blade section in meters, and r_i is the radial location of the blade section in meters.

5.) Equation (11) was used to solve for the G grade. The rotor mass, W, was computed using the newly interpolated blade mass properties in addition to the hub mass. The rotational speed N was found by running the simulations, which was 11.8 rpm regardless of the mass imbalance applied in these tests. The imbalance being applied was equal to the calculated change in mass in step 4, which was input as U_{per}. Finally, the mass imbalance was applied at R_{eff}, and the equation was formulated as in equation (12) and solved for G:

$$G = \frac{U_{per} \cdot N}{9549 \cdot W} \cdot 10^6 R_{eff}. \tag{14}$$

To apply the 0.5% increase in blade mass (Moog), it was assumed that the added mass was distributed evenly along one blade and would therefore act at its center of mass. The center of mass of the unaltered blades was known to be 18.392 meters, and the total rotor mass was 105,773 kg, both indicated in the FAST *.fsm output file. The mass of each individual blade was 16331 kg, so 0.5% of the total blade mass was 245 kg. Therefore, applying equation (14), a mass of 245 kg acting at 18.392 meters corresponds to a G grade of approximately 53, which is quite a bit higher than the permissible level of 16 used in field balancing. These two imbalance levels provided reference points for simulations. Two additional imbalance grades were tested:

G6.3 and G40. As a reference, see Table 2 for groups of representative rigid rotors and their common balance quality grades. Note that a rigid rotor is defined as one whose operating speed is less than 50% of its first critical speed [24]. To verify this assumption, FAST was used as an ADAMS preprocessor to construct an ADAMS dataset of the complete aeroelastic properties of a wind turbine. ADAMS is a multibody dynamics simulation software package, and it was used to perform the linearization and eigenanalysis of the turbine model to obtain its modal frequencies and vectors. The first flexible rotor mode has a natural frequency of 0.65 Hz and the maximum rotor speed is 12.1 rpm, or 0.2 Hz, thus satisfying the rigid rotor assumption for the purposes of mass imbalance qualification.

Table 2. ISO 1940-1 Balance quality grades for groups of representative rigid rotors (IRD Balancing 2009).

Balance Quality Grade	Product of the Relationship ($e_{per} \times \omega$) [1] [2] mm/s	Rotor Types - General Examples
G 4 000	4 000	Crankshaft/drives[3] of rigidly mounted slow marine diesel engines with uneven number of cylinders[4]
G 1 600	1 600	Crankshaft/drives of rigidly mounted large two-cycle engines
G 630	630	Crankshaft/drives of rigidly mounted large four-cycle engines Crankshaft/drives of elastically mounted marine diesel engines
G 250	250	Crankshaft/drives of rigidly mounted fast four-cylinder diesel engines[4]
G 100	100	Crankshaft/drives of fast diesel engines with six or more cylinders[4] Complete engines (gasoline or diesel) for cars, trucks and locomotives[5]
G 40	40	Car wheels, wheel rims, wheel sets, drive shafts Crankshaft/drives of elastically mounted fast four-cycle engines with six or more cylinders[4] Crankshaft/drives of engines of cars, trucks and locomotives
G 16	16	Drive shafts (propeller shafts, cardan shafts) with special requirements Parts of crushing machines Parts of agricultural machinery Individual components of engines (gasoline or diesel) for cars, trucks and locomotives Crankshaft/drives of engines with six or more cylinders under special requirements
G 6.3	6.3	Parts of process plant machines Marine main turbine gears (merchant service) Centrifuge drums Paper machinery rolls; print rolls Fans Assembled aircraft gas turbine rotors Flywheels Pump impellers Machine-tool and general machinery parts Medium and large electric armatures (of electric motors having at least 80 mm shaft height) without special requirements Small electric armatures, often mass produced, in vibration insensitive applications and/or with vibration-isolating mountings Individual components of engines under special requirements
G 2.5	2.5	Gas and steam turbines, including marine main turbines (merchant service) Rigid turbo-generator rotors Computer memory drums and discs Turbo-compressors Machine-tool drives Medium and large electric armatures with special requirements Small electric armatures not qualifying for one or both of the conditions specified for small electric armatures of balance quality grade G 6.3 Turbine-driven pumps
G 1	1	Tape recorder and phonograph (gramophone) drives Grinding-machine drives Small electric armatures with special requirements
G 0.4	0.4	Spindles, discs and armatures of precision grinders Gyroscopes

4.3.3. *Simultaneous Pitch Error and Mass Imbalance Simulation Methods*

It is possible that aerodynamic asymmetry and mass imbalance are present simultaneously in a wind turbine rotor. This presents the greatest challenge for a rotor imbalance condition monitoring system, that is, distinguishing between mass and aerodynamic imbalance. Two basic cases are considered: (1) the mass imbalance was located on blade three, while the pitch error occurred for blade two, and (2) the mass imbalance and pitch error both occurred on blade three. Only a small number of test cases were run with the goal of determining which detection algorithms were successful at detecting the simultaneous imbalances, ignoring the sensitivity of the algorithms to simultaneous imbalances. The same mass imbalance grading system and pitch error methods described in the earlier sections were used for these tests.

4.4. Analysis of Imbalance without Blade Sensors

In order to compare the effectiveness of imbalance detection methods with and without blade sensors, algorithms were first generated for determining imbalance using only the outputs from FAST that would not require blade-mounted sensors. From the 200 variables which were generated at outputs from the FAST simulation, those which displayed a significant percentage change in their RMS value or frequency response magnitude at multiples of the operating speed for a given a mass imbalance or pitch error were identified as key measurement channels. As was shown in section 4.2, imbalance tends to excite the 1p frequency in the order domain. It has also been shown that the 2p and 3p harmonics can be influenced by aerodynamic imbalances, especially in the presence of wind shear [28], thus the 1p, 2p, and 3p frequencies were reviewed for changes in magnitude from the baseline tests.

The rotor azimuth position output from FAST was used as the reference signal for time synchronous averaging (TSA). To perform rotational resampling, the azimuth signal was converted to radians, was unwrapped and then the measurement signal was interpolated so that each revolution contained the same number of data samples with each sample corresponding to the same azimuth position of the rotor's rotation. Finally, blocks of three revolutions were averaged together; more than one revolution was used in the block size to increase the length of the block's time history, thereby increasing the frequency resolution of the DFT of the averaged signal. The imbalance detection algorithms for non-blade sensors all functioned similarly through the detection of changes from baseline measurements either in the RMS response or in the power spectral density magnitude at 1p, 2p, or 3p.

4.4.1. *Pitch Error Analysis Results*

The following sections summarize the trends in the results for pitch error aerodynamic imbalance, as measured in the generator power output, nacelle inertial sensors, and low speed shaft bending moments (a subset of non-blade virtual measurements with most significant sensitivity to imbalance).

4.4.1.1. Generator Power

The generator power output displayed unique and readily identifiable changes due to pitch error when the wind speed is below the rated speed for the turbine, as it was for these simulations.

Figure 19 shows the expected result that as the pitch error of blade three increases, the mean power output of the turbine decreases significantly due to the reduced aerodynamic efficiency of the incorrectly pitched blade. Moreover, the zoomed-in view of one revolution of the TSA power signal in Figure 20 shows that the power output shifts from having predominantly 3p oscillations for zero pitch error to a progressively larger 1p fluctuation with increasing pitch error. The magnitude of the 1p component most likely decreases as pitch error moves above 7.5° because the reduced rotor speed has consequently reduced the loading magnitude. The 3p oscillation for zero pitch error is a common occurrence due to the increased wind speeds caused by vertical wind shear and seen by the upright, 0° azimuth positioned blade. This occurs three times per revolution, once as each blade passes the 0° position, resulting in larger aerodynamic forces on that blade and thus a 3p oscillation in rotor torque. It should also be noted that the rotor torque signal displayed very similar characteristics to the generator power output. Because the generator power can be subject to electrical faults as well, analyzing rotor torque measured at the low speed shaft may be a better indicator of mechanical behavior in the field.

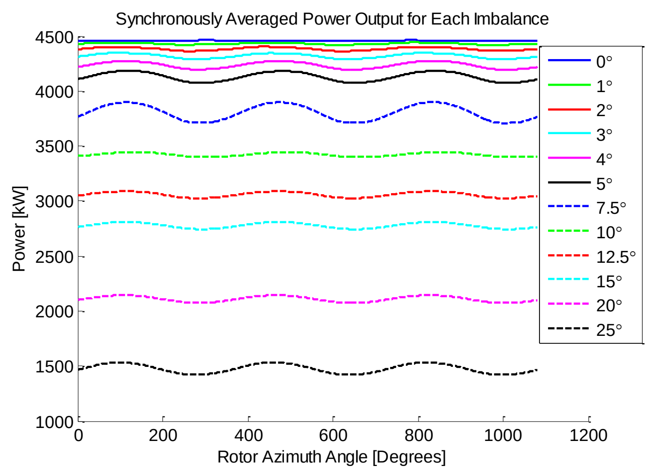

Figure 19. Three revolution time synchronously averaged power output for each pitch error test.

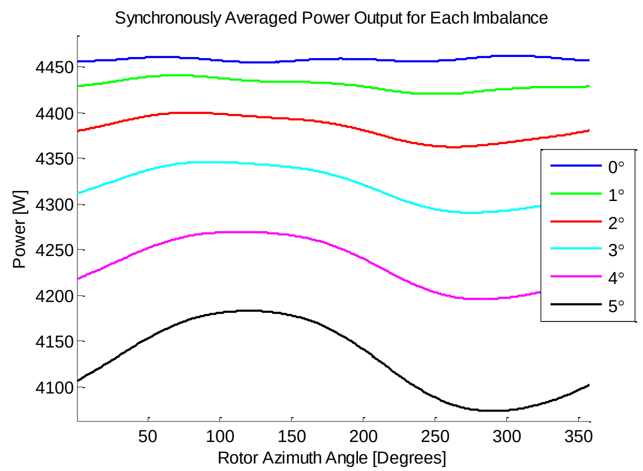

Figure 20. Single revolution zoomed-in single revolution TSA power output for pitch errors of 0° to 5°.

Figure 21 summarizes these findings by plotting the magnitude of the 1p component in the power spectrum (PS) of the generator power signal as well as the mean power. The 1p PS magnitude increases dramatically until a pitch error of 7.5°, after which the mean power is significantly reduced, and the 1p trend restarts at a lower initial level. Therefore, using the turbine's known power versus wind speed curve along with this data can help determine if a pitch error is present and could be used to estimate its level of severity. Significant deviations from the expected mean power output, given a particular wind speed, can indicate a possible pitch error. The magnitude of the 1p PS component, given the mean power, can help determine the severity of the pitch error.

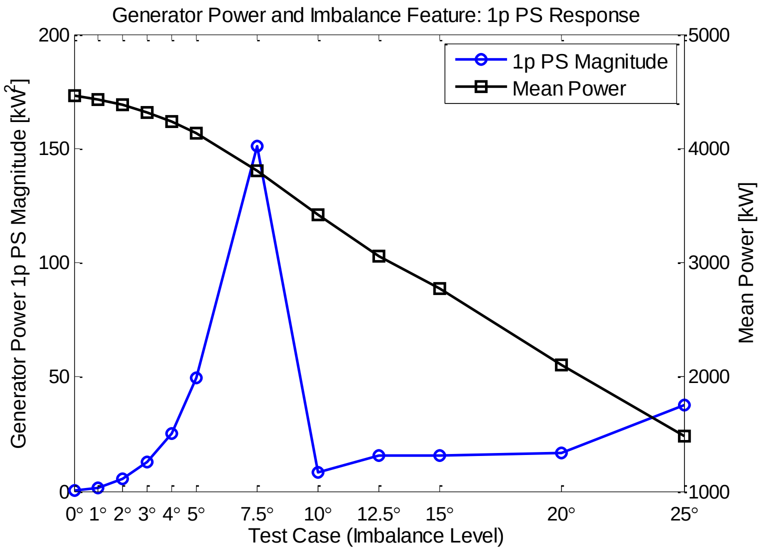

Figure 21. Mean generator power and 1p PS magnitude.

4.4.1.2. Nacelle Inertial Measurements

Nacelle inertial measurements are often recommended in wind turbine condition monitoring literature for detecting rotor imbalance. For all subsequent discussion, axial nacelle acceleration will refer to acceleration in the x_s direction in Figure 11, which is equivalent to the y direction in Figure 14. Transverse nacelle motion is in the side-to-side direction, which is the y_s axis in Figure 20 or the z axis in Figure 14. As was demonstrated in the dynamics model of section 4.2, the 1p component of the axial acceleration of the nacelle should be indicative of an aerodynamic imbalance. Similarly, the moments about the transverse and vertical axes, y_s and z_s shown in Figure 20, respectively, should also be affected in their 1p response by aerodynamic imbalance. However, instead of plotting the moment outputs from FAST, the nacelle angular acceleration outputs were used and the magnitude of the 1p PS of each of those measurements, as well as the nacelle axial and transverse accelerations, are shown in Figure 22.

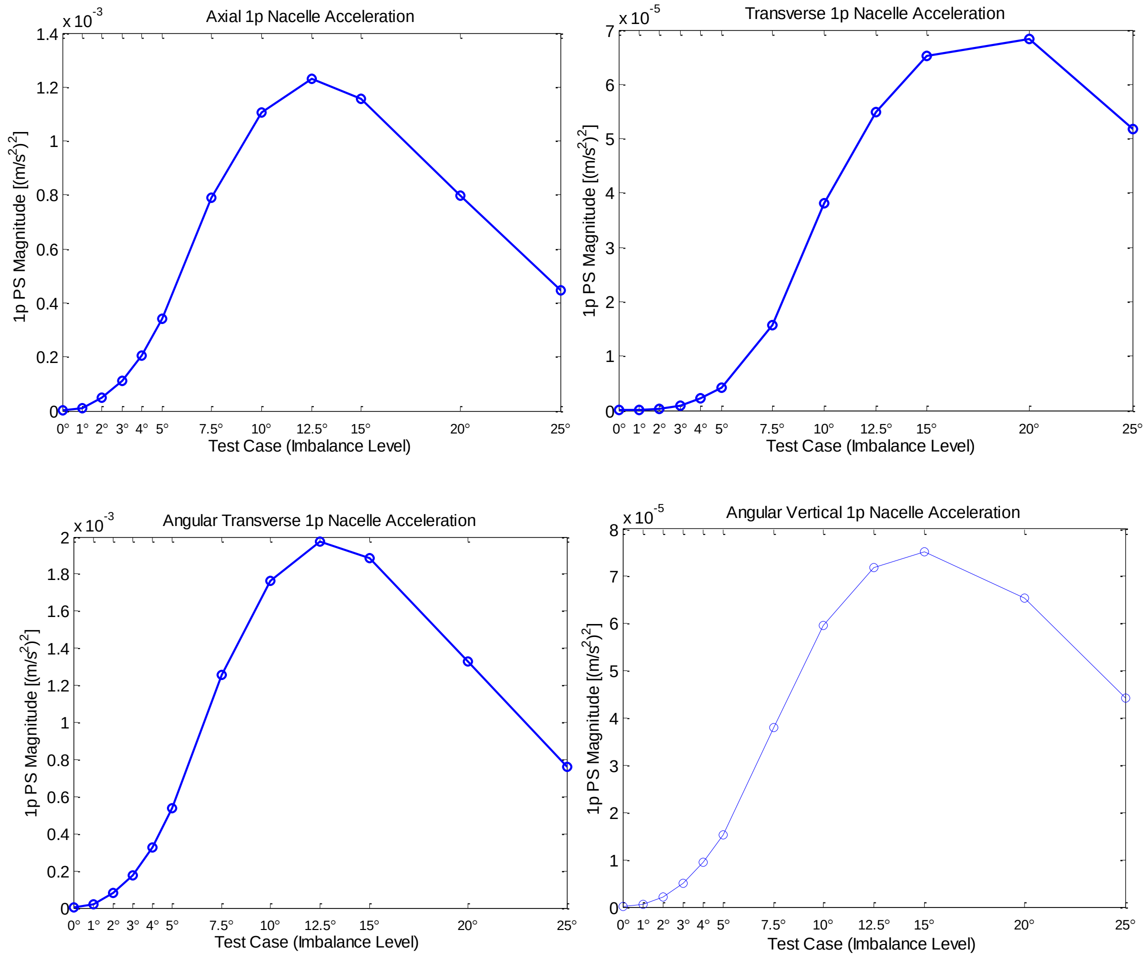

Figure 22. Nacelle axial and transverse accelerations and angular accelerations about the transverse and vertical axes vs. pitch error.

The 1p PS magnitude follows a similar trend in both the axial nacelle acceleration and the angular nacelle acceleration about the transverse axis. For 12.5° pitch error and greater, the 1p magnitude begins to fall, which is again likely due to decreased loading magnitude from the reduction in rotor speed. Interestingly, the transverse nacelle acceleration shows a similar trend and does not begin to fall off until 25° pitch error. However, these oscillations are two orders of magnitude lower than the axial acceleration, and the 1p magnitude changes less rapidly in the 0°-5° range, making this a less sensitive measurement channel for low pitch error. Finally, the angular acceleration about the vertical nacelle axis displays a similar trend to the transverse angular acceleration, but is two orders of magnitude lower.

4.4.1.3. Low Speed Shaft Bending Moments

The low speed shaft (LSS) bending moments also displayed significant changes due to pitch error. FAST outputs the bending moment in rotating and non-rotating frames, as well as shaft tip locations or strain gage locations. To coincide with measurements that would be taken on operating wind turbines in the field, the low speed shaft bending moment at the shaft's strain gage in the rotating frame of reference was used in this analysis. The rotating frame can be referred to in the discussion in Section 3.0. Figure 23 shows a significant increase in the magnitude of the low speed shaft bending moment with increasing pitch error, and Figure 24 shows the increase in the magnitude of the low speed shaft bending moment in terms of the root mean square (RMS) value for each pitch error. Unlike the nacelle inertial measurements, the RMS LSS bending moment continues to increase up to 25° pitch error.

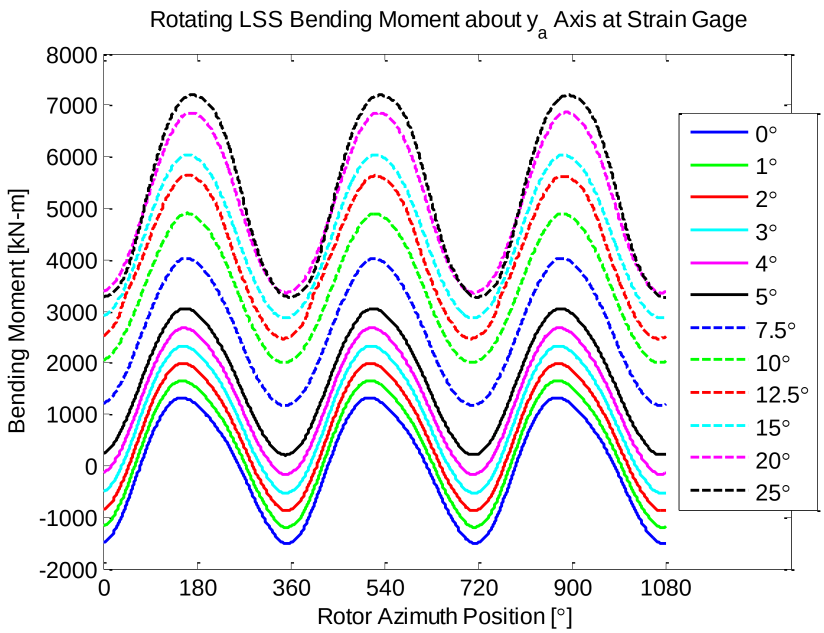

Figure 23. Three-revolution TSA rotating low speed shaft bending moment.

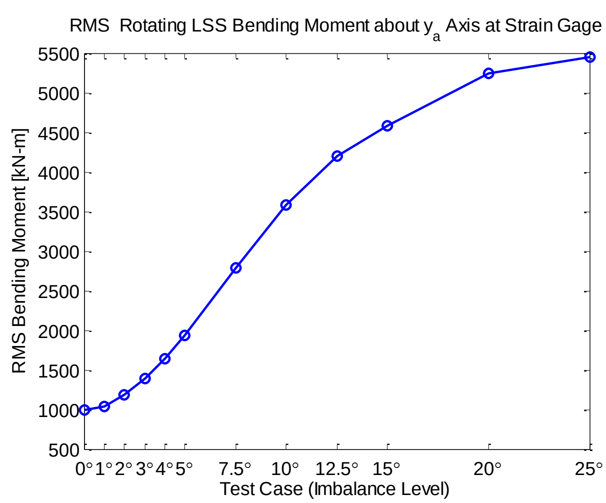

Figure 24. RMS rotating LSS bending moment vs. pitch error.

4.4.2. *Mass Imbalance Analysis Results*

The following sections summarize the trends in the results for mass imbalance, as measured in the same three non-blade measurements of generator power output, nacelle inertial sensors, and low speed shaft bending moments.

4.4.2.1. Generator Power

Figure 25 and Figure 26 indicate that the mean power remained unchanged with the five varying levels of rotor mass imbalance evaluated: G0 (baseline, no imbalance), G6.3, G16, G40, and G53 (representing the 0.5% total blade mass imbalance). However, the 1p PS magnitude of the generator power signal increased with increasing mass imbalance, and in the case of pitch error, the power oscillations shifted from a predominantly 3p frequency to 1p frequency when an imbalance was present. These results indicate that a decrease in mean power can be an indicator of aerodynamic imbalance, but an increase in the 1p PS magnitude of the generator power over the baseline test can be a result of either a mass or an aerodynamic imbalance. Therefore, further measurements are required to distinguish between the two.

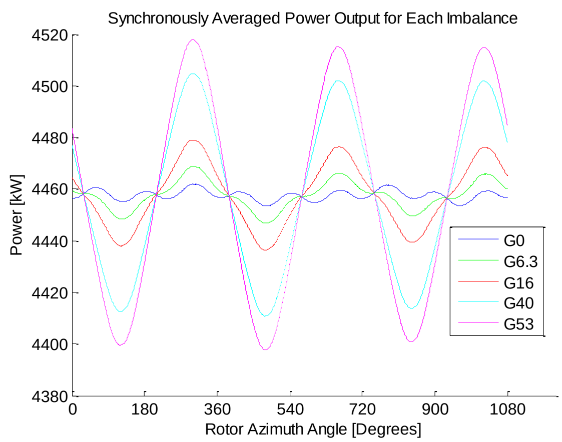

Figure 25. Three-revolution time synchronously averaged power output for each mass imbalance test.

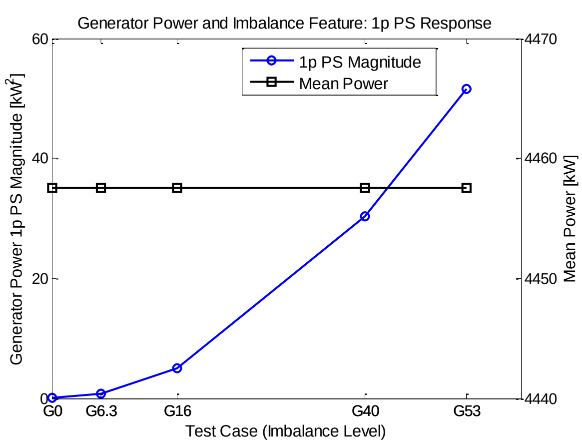

Figure 26. Mean generator power and 1p PS magnitude

4.4.2.2. Nacelle Inertial Measurements

In the case of mass imbalance, the magnitude of the 1p PS of the inertial measurements was three or more orders of magnitude lower than the acceleration generated by the pitch errors. The trend of increasing 1p PS is very similar in all four inertial measurements in Figure 27. The transverse nacelle acceleration is greater than the acceleration in the axial direction in agreement with the literature, but all four accelerations are so small that they would be very difficult to measure.

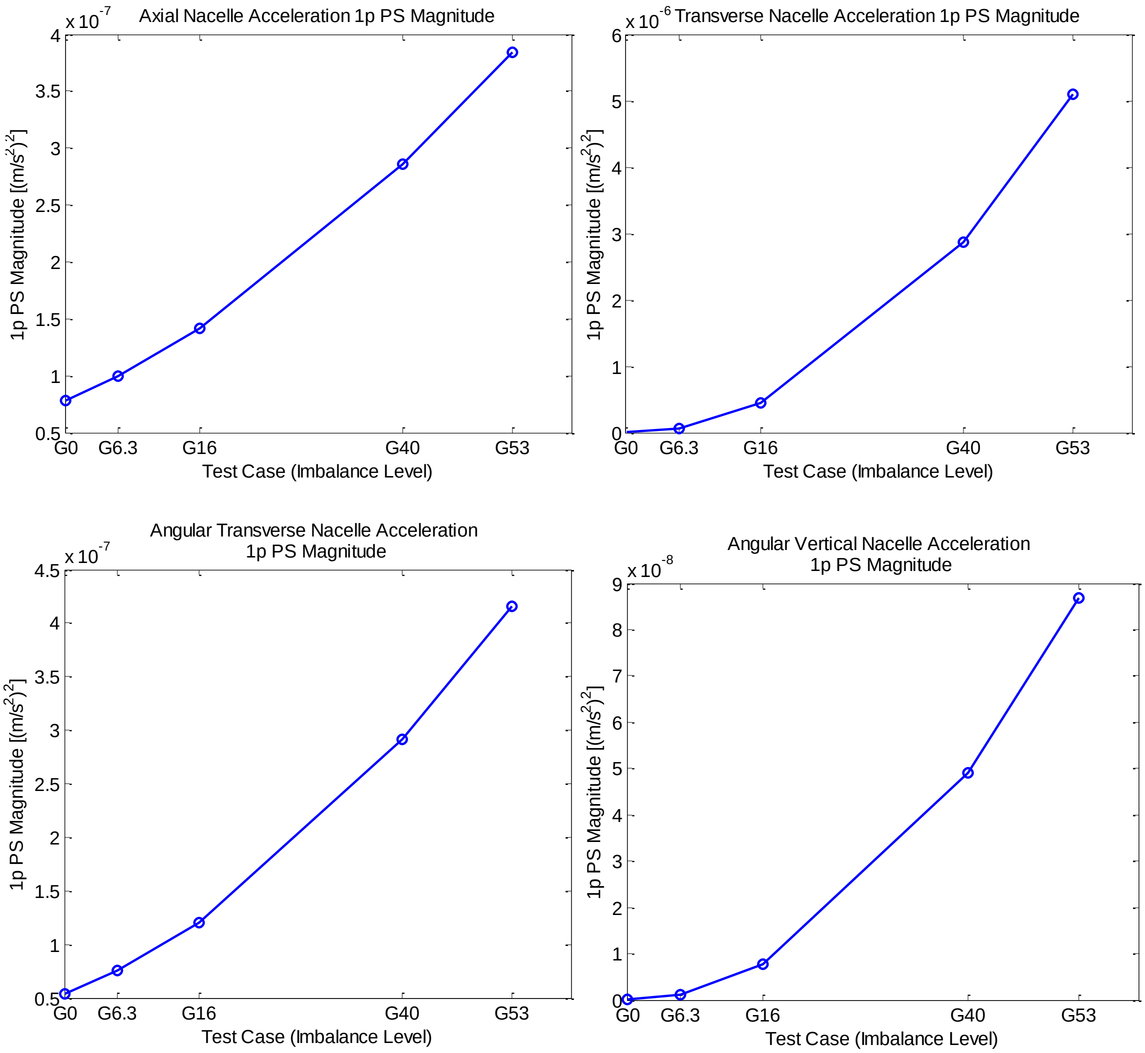

Figure 27. Nacelle axial and transverse accelerations and angular accelerations about the transverse and vertical axes for mass imbalance

4.4.2.3. Low Speed Shaft Bending Moments

The low speed shaft bending moment was virtually unaffected by mass imbalance, as demonstrated in the TSA signal in Figure 28. There was only a 0.46% increase in the shaft bending moment due to the largest mass imbalance simulated. Pitch error on the other hand caused a 5.5% increase in the RMS shaft bending moment for the smallest error of 1°. So, while some measurements have been shown to be largely insensitive to mass imbalance and highly sensitive to aerodynamic imbalance, the converse situation has not presented itself in any of the non-blade outputs. Therefore, distinguishing between mass and aerodynamic imbalance using non-blade measurements is difficult, as will be expanded upon in the next section which considers simultaneous mass and aerodynamic imbalances.

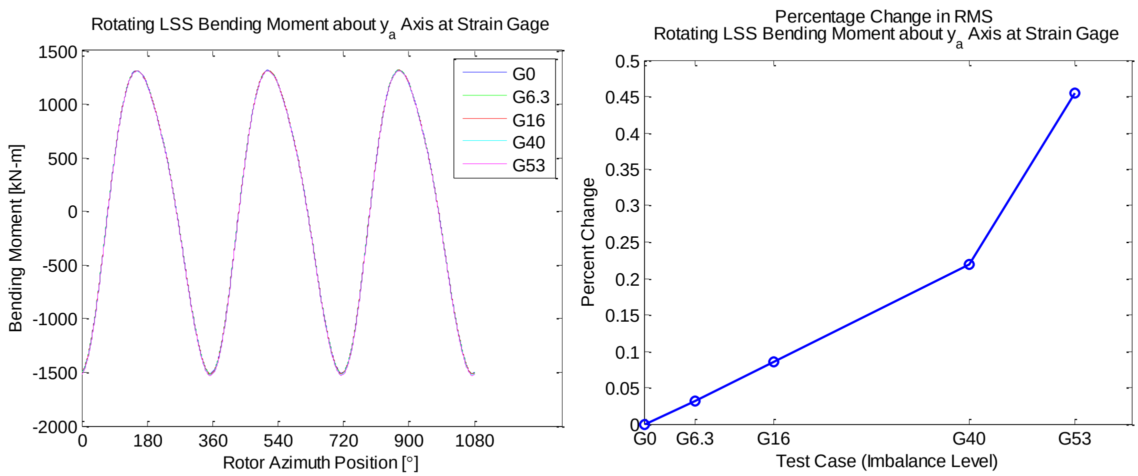

Figure 28. Three-revolution TSA rotating low speed shaft bending moment and percent change in RMS

4.4.3. *Simultaneous Mass Imbalance and Pitch Error Results*

The following sections will analyze the results of simulations performed with a simultaneous mass and aerodynamic imbalance applied to the rotor. Included are tests with mass and aerodynamic imbalances applied to the same blade, blade three, as well as tests in which blade three contained the increased mass and blade two exhibited pitch error. The syntax for the plot legends and axis labels referring to the different test cases is as shown in Figure 29. If no mass or aerodynamic imbalance was applied in the test, the “B” corresponding to that imbalance will be followed by a zero. Moderate mass and aerodynamic imbalance levels were chosen for these simulations: G16 and G40, and 3° and 5° pitch errors. To aid in quantifying the difference between the simultaneous imbalance cases, each mass imbalance was also applied with no simultaneous pitch error for comparison. The same three non-blade measurements, generator power output, nacelle inertial sensors, and low speed shaft bending moments are once again examined.

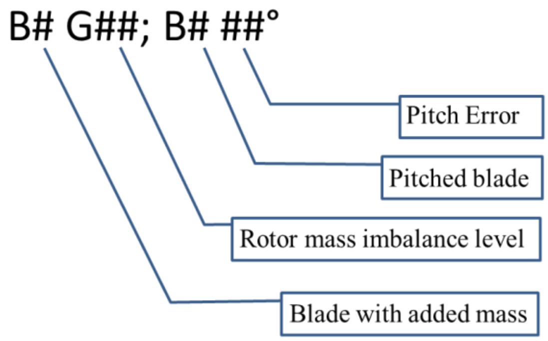

Figure 29. Simultaneous mass and aerodynamic imbalance test designation syntax

4.4.3.1. Generator Power

The generator power output for these tests coincides with what is expected from the results of individual mass and aerodynamic imbalance in the previous sections. Figure 30 and Figure 31 show that there are three distinct groups of test conditions with the same mean power output: those tests with the same pitch error, regardless of the mass imbalance or which blade was pitched, generate the same mean power. The mean power levels were 4458 kW, 4319 kW, and 4130 kW for pitch errors of 0°, 3°, and 5°, respectively.

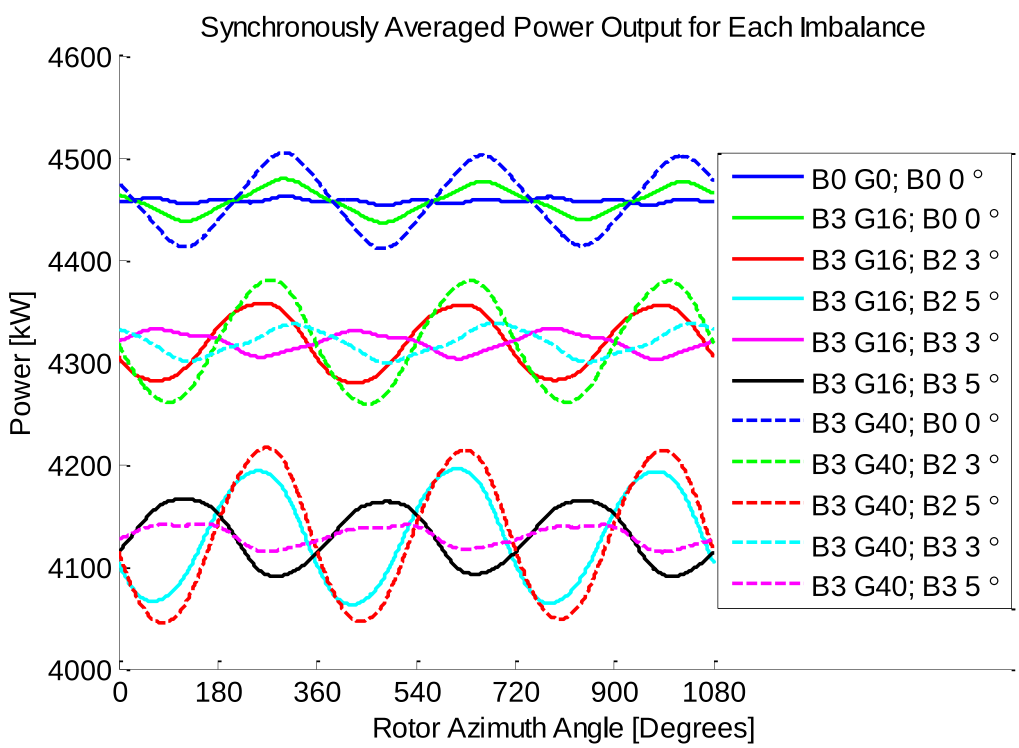

Figure 30. Three-revolution TSA power output for each simultaneous imbalance test

Figure 31 confirms that the 1p PS magnitude of the power signal is dependent on both the mass and aerodynamic imbalance, as was demonstrated in the previous sections. Interestingly, it also reveals that the 1p response is greater if the mass addition and aerodynamic imbalance are on different blades, as can be seen by comparing the B3G16, B2 3° case to the B3G16 B3 3° case, for instance. A more intuitive response is found when looking at the 2p frequency in the order domain, as shown in Figure 32. It shows that the 2p PS magnitude is largely dependent on the pitch error; however, when the added mass is on a different blade than the one undergoing pitch error, the 2p response is higher, again as in the B3G16, B2 3° and B3G16, B3 3° cases, where the magnitude changes by about 3.5%. This trend follows for the other three sets of imbalances as well (for example see cases B3G40, B2 5° and B3G40 B3 5°). Furthermore, the 2p response also increases for increasing mass imbalance. Although the changes look fairly small when compared to the changes brought about by pitch error, the response increases by about 3% from B3G16, B2 5° to B3G40 B2 5°, for example. So, it may be possible to determine if there are simultaneous mass and aerodynamic imbalances from the generator power. However, it would likely require a fairly accurate simulation model to determine the response PS thresholds and this method is still ineffective in determining which blades are responsible for the mass or aerodynamic imbalance.

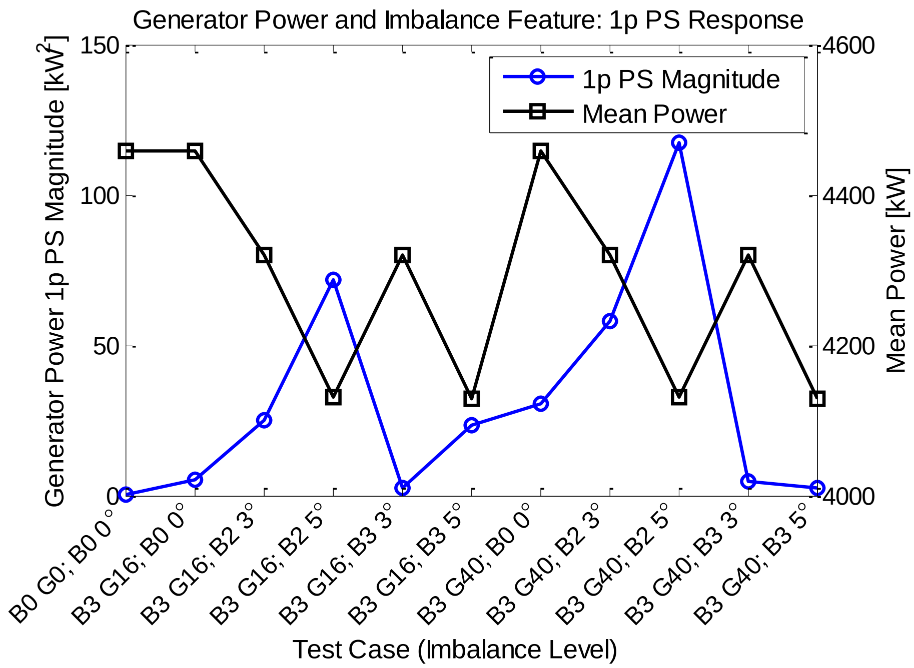

Figure 31. Mean generator power and 1p PS magnitude.

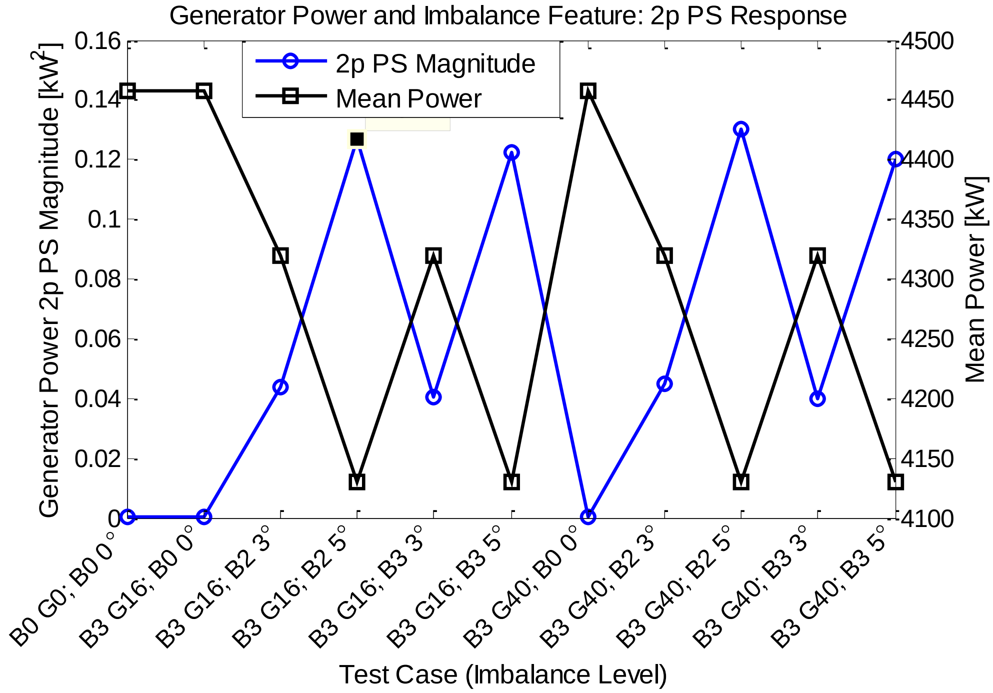

Figure 32. Mean generator power and 2p PS response.

4.4.3.2. Nacelle Inertial Measurements

To coincide with suggested methods from the literature, we again consider the 1p nacelle inertial responses. The axial nacelle acceleration and the two angular accelerations follow a very similar trend to the 2p generator power PS magnitude, as shown in Figure 33. The angular accelerations look nearly identical to the axial acceleration and have therefore been omitted. Pitch error accounted for the largest percentage differences in the response. When pitch and mass imbalances were applied to different blades, the response was higher than when the same imbalance levels were applied to the same blade. The transverse nacelle acceleration response is less clear. In theory, the transverse response should be more sensitive to mass imbalance than pitch error, but it is clearly affected largely by pitch error [41]. The response seems to follow an expected trend from the first test case up to B3 G16, B3 5°. After that point, it would seem that the trend should restart, but with a higher initial value due to the larger G40 mass imbalance. The B3 G40, B0 0° response is indeed higher than B3 G16, B0 0°, but the response takes an unexpected dip at B3 G40, B2 3° and 5°. The likely cause is that the B3G40 and B2 3° and 5° errors cause similar transverse nacelle accelerations, as indicated in Figure 22 and Figure 27, but these responses are out of phase when the imbalances are applied to different blades. Therefore, phase is another important consideration when examining non-blade measurements for simultaneous imbalances acting on different blades.

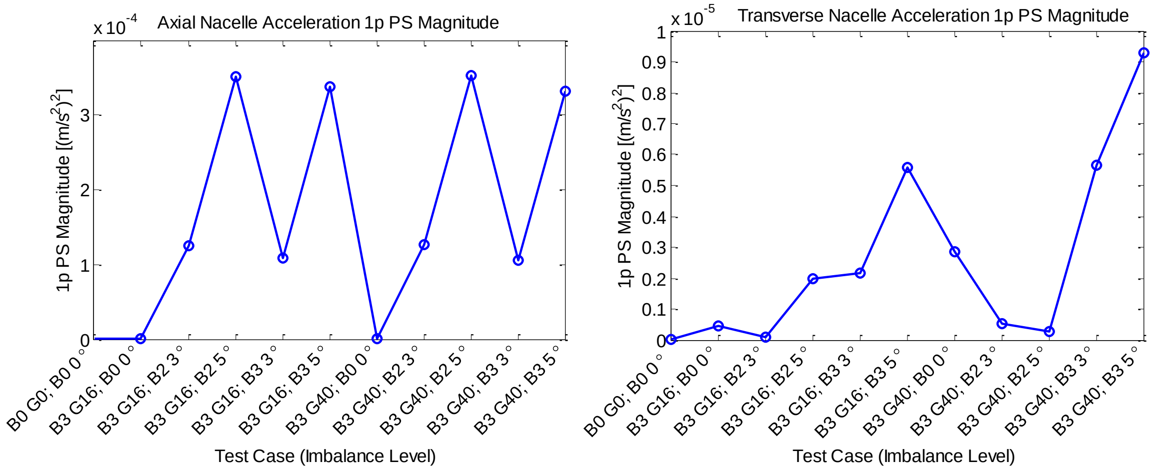

Figure 33. Nacelle axial and transverse accelerations for simultaneous imbalance

4.4.3.3. Low Speed Shaft Bending Moments

Similar to the other non-blade measurements considered thus far, the low speed shaft bending moment becomes less effective when trying to distinguish between mass imbalance and pitch error. Figure 34 demonstrates that different levels and locations of mass and aerodynamic imbalances produce very similar results. For instance, B3 G16, B3 5° has an RMS value nearly equal to that of the B3 G40, B2 5° imbalance.

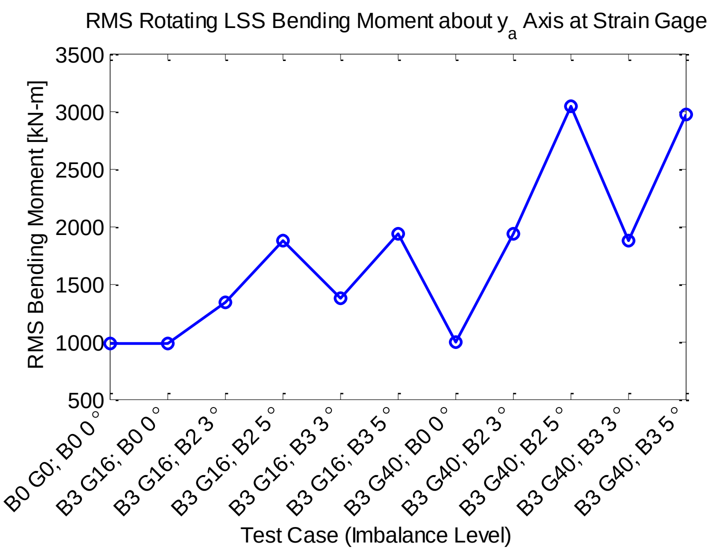

Figure 34. RMS rotating LSS bending moment vs. pitch error

4.5. Analysis of Imbalance with Blade Sensors

In Section 4.4, it was illustrated that some non-blade measurements provide good insight into detecting the presence of a mass or aerodynamic imbalance in the rotor and assessing its level of severity, but they lacked the ability to determine which blade(s) is the culprit (i.e location), and in general provided confounding results when mass and aerodynamic asymmetries were simultaneously present. The next sections will examine outputs from the FAST simulations that would depend on blade-mounted sensors in an operating turbine.

4.5.1. *Pitch Error Analysis Results*

The following sections summarize the trends in the results for pitch error, as measured in blade tip acceleration responses and blade root bending moments.

4.5.1.1. Blade Tip Acceleration Response

The mean flap, RMS flap and edge degree-of-freedom blade accelerations are shown in the left two plots of Figure 35. The mean flap response of the pitched blade three decreases significantly with increasing pitch error. As with some of the non-blade responses, the other two blade flap responses also begin to decrease around 7.5° as a result of reduced forcing from the slowed rotor. For that reason, it is helpful to examine the blade-to-blade differences in the response, shown in the right two plots in Figure 35. The plot legend indicates which two blade responses have been subtracted from one another; the first blade listed has been subtracted from the second one. For instance, the blue line, Blades 1 & 2, shows the result of subtracting blade two's response from blade one's response. If the blade responses were all the same or very close, then no pitch error is present. When two blade-to-blade differences change, it can indicate the problematic blade. Figure 36 illustrates which blade may be problematic (the terminal point of the arrows) based on which pair of blade-to-blade differences is different than the third (the starting point of the arrows). This method is also beneficial because it can eliminate the need for baseline data, but thresholds would still need to be set to determine what level of response difference indicates an error. Note that in the blade-to-blade differences in Figure 35, blades 1 and 3 and blades 2 and 3 are grouped together, correctly indicating that blade 3 is the pitched blade. The absolute value of the difference was not plotted in Figure 35 because in some cases, the sign of the difference can be an indicator of the pitch error. For instance, the lead-lag RMS tip acceleration is lower for the pitched blade until 7.5° pitch error but at 7.5° and above the pitch error is higher. Therefore the sign of the difference helps distinguish between a 5° and 7.5° pitch error, which are close in magnitude but opposite in sign. Finally, the response of blade 1 and 2 is slightly different; this is thought to be caused by blade 2 passing through the wake of the incorrectly pitched blade 3 as it rotates.

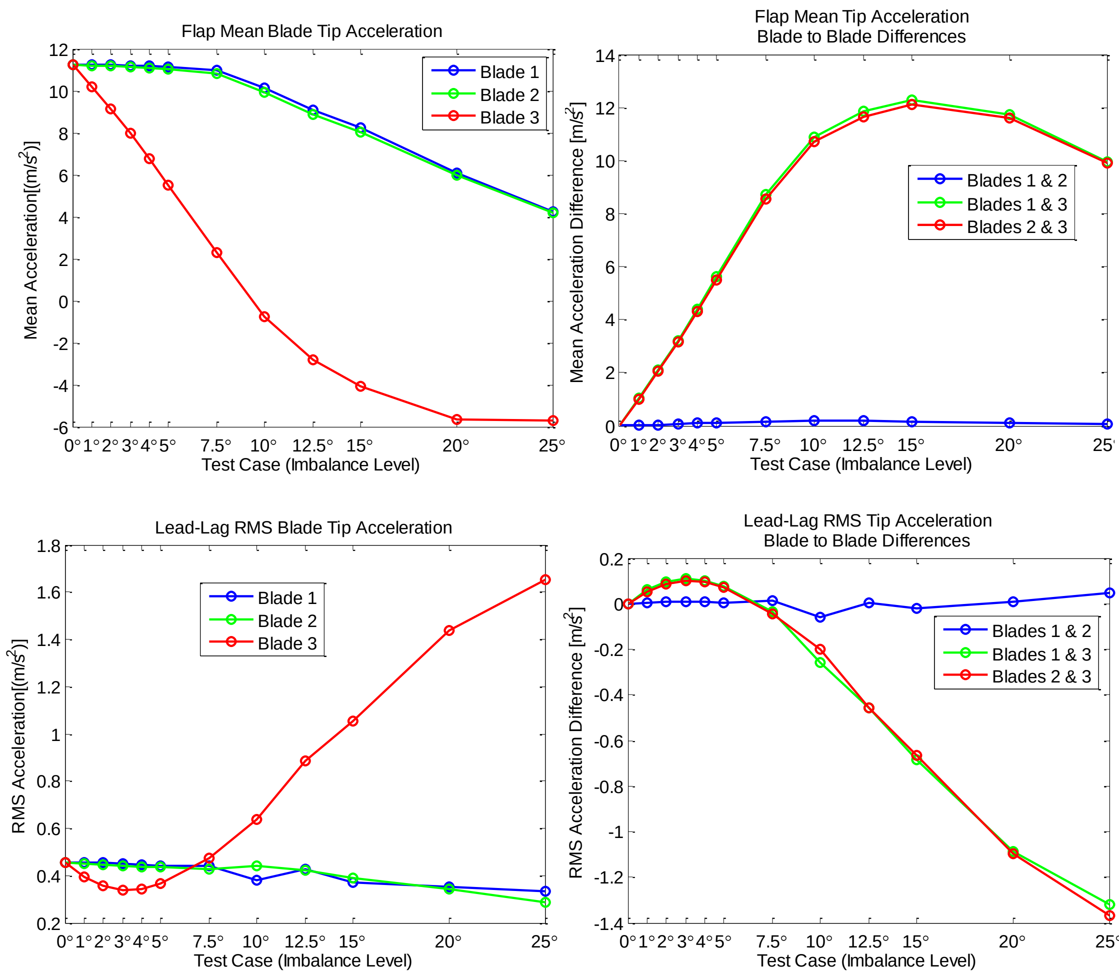

Figure 35. Span and edgewise blade tip accelerations and blade-to-blade differences for pitch error.

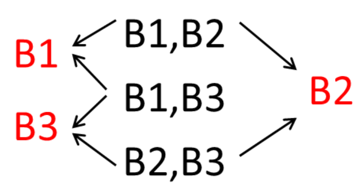

Figure 36. Diagram to determine faulty blade using blade-to-blade differences

Note that the flap response is much more sensitive to low pitch error, 5° or less, than the nacelle axial response shown previously in Figure 22. This makes the blade response a valuable tool in diagnosing aerodynamic imbalances. Lastly, Figure 37 demonstrates that the 1p PS magnitude of the edgewise blade tip acceleration is a fairly good indicator of pitch errors above about 3°. Again, the differences in the response magnitude of blade 1 and 2 are thought to be caused by blade 2 passing through the wake of the pitched blade 3 during rotation.

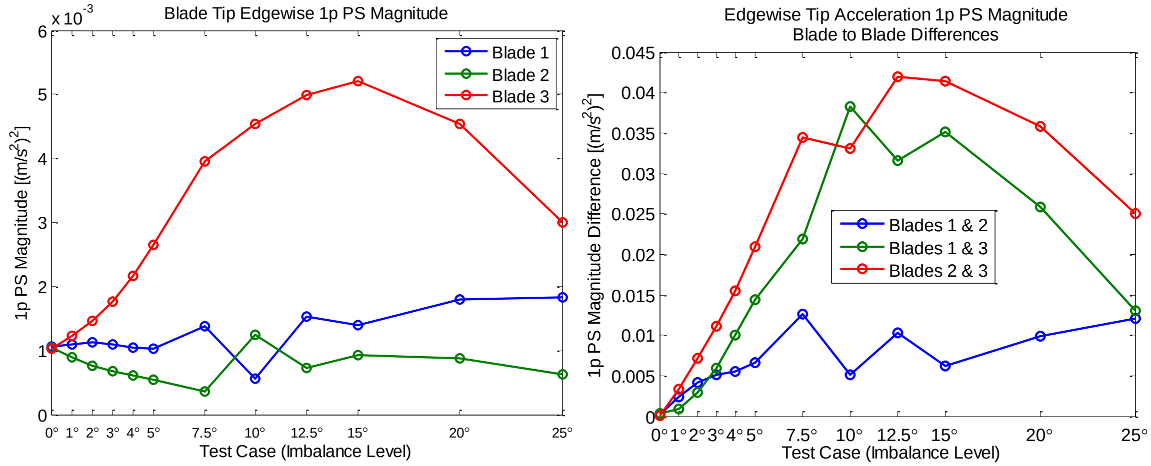

Figure 37. Blade tip edgewise 1p PS magnitude and blade to blade differences

4.5.1.2. Blade Root Pitching Moments

The moment of the blade about its pitch axis at the blade root is another good indicator of pitch error, as shown in Figure 38. It should be noted that the root pitching moment was also the most sensitive parameter to a trailing edge disbond, as shown in last year's work. This moment can be measured using strain gages located at the root of each blade. Again it is seen that the 1p PS magnitude tends to fall off due to reduced forcing from the slowed rotor for pitch errors greater than 10°, but the mean pitching moment of the pitched blade continues to decrease relative to the other two. Note that the plot in the lower right of Figure 38 displays the absolute value of the mean difference.

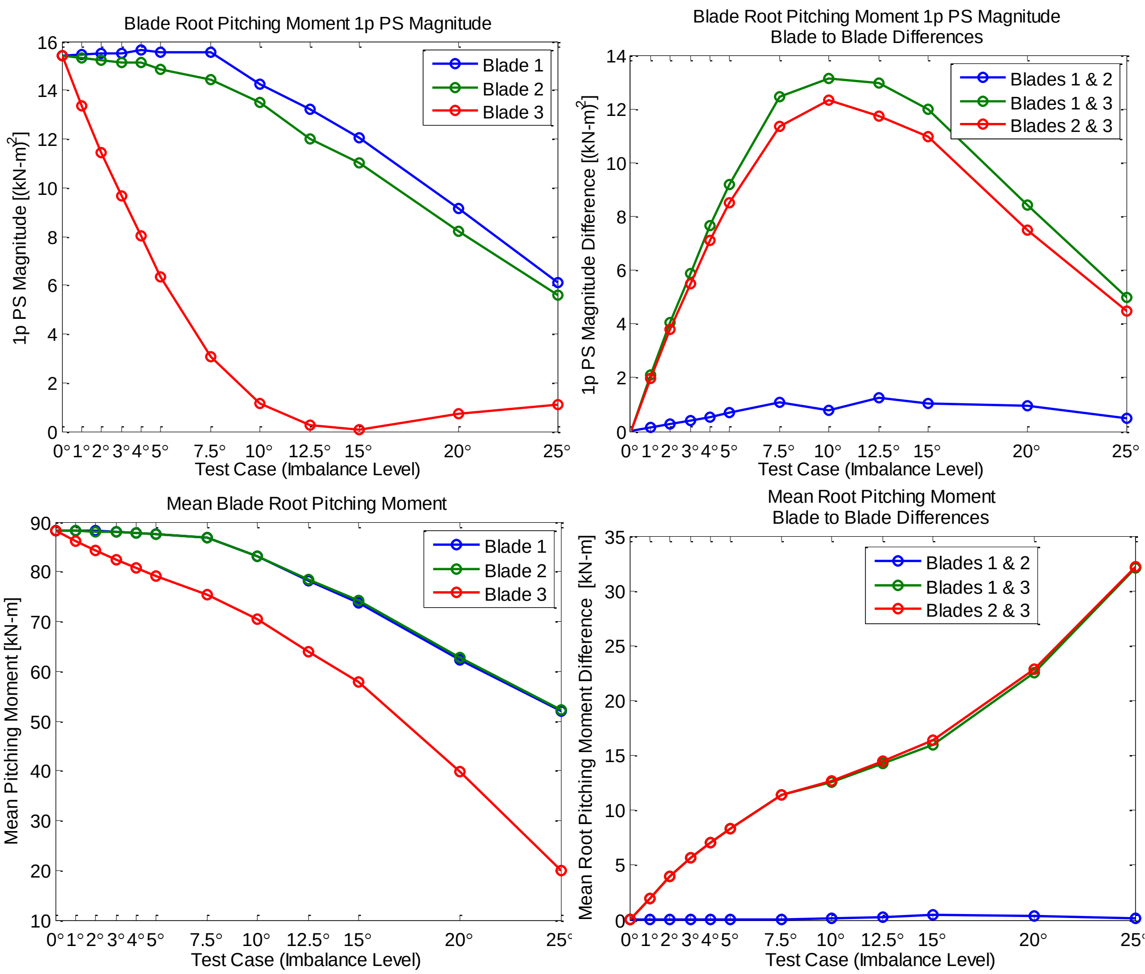

Figure 38. Blade root pitching moment 1p PS magnitude, RMS, and blade-to-blade differences

4.5.2. *Mass Imbalance Analysis Results*

4.5.2.1. Blade Root Axial Force

The mass imbalances produced essentially no differences in the blade tip accelerations or root bending moments. However, the axial (span-wise) force as measured in the blade root did increase for the blade containing increased mass, as shown in the RMS values and blade-to-blade differences in Figure 39. While axial force is the output variable from FAST, axial strain as measured by a strain gage or fiber optic sensor could provide the equivalent measurement on an operating turbine.

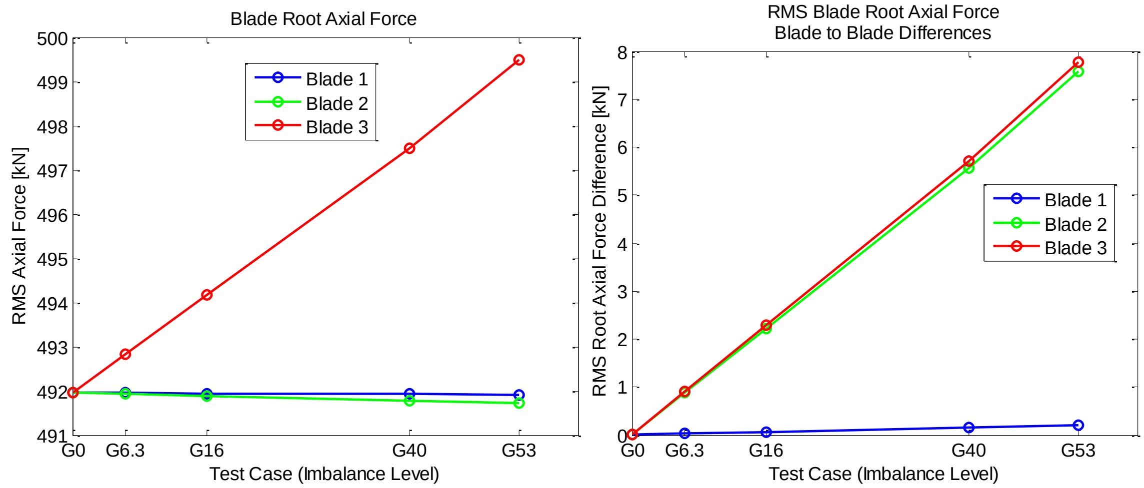

Figure 39. Blade root RMS axial force and blade-to-blade RMS differences

4.5.3. *Simultaneous Mass Imbalance and Pitch Error Results*

Section 4.4.3 demonstrated that it was difficult to distinguish simultaneous mass imbalance and pitch error using non-blade measurements. The following sections will demonstrate the advantages of blade measurements in detecting the presence of mass imbalance or pitch error, as well identifying which blade is responsible for each error.

4.5.3.1. Blade Tip Acceleration Response

As was indicated in section 4.5.1.1, the mean (or RMS) flap and edge blade tip acceleration responses were indicative of pitch error and could identify which blade was pitched incorrectly. This remained true even when mass imbalances were present, as shown in Figure 40. Note that the 1p lead-lag response was still a good indicator of pitch error, as was the span acceleration response, but both were left out for the sake of brevity. In experimental testing, the span and lead-lag degrees of freedom tend to exhibit less measurement noise and variance and therefore may be more beneficial than the flap degree of freedom measurement for use in statistics-based condition monitoring systems.

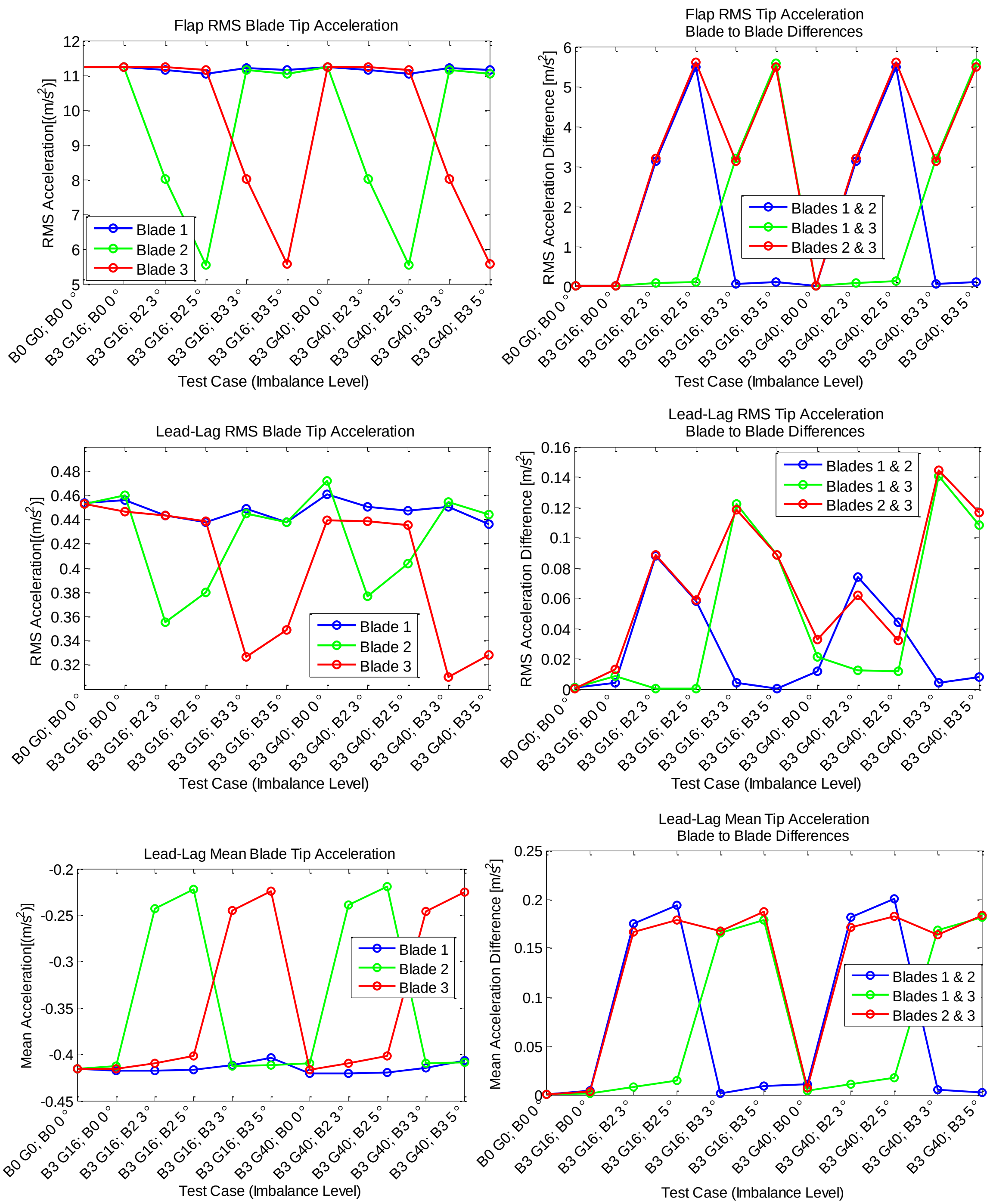

Figure 40. Span and edgewise blade tip accelerations and blade-to-blade differences for simultaneous mass imbalance and pitch error

4.5.3.2. Blade Root Pitching Moments

The RMS and 1p PS magnitude of the blade root pitching moments decreased very consistently for the pitched blade, as seen in Figure 41. For instance, the 1p PS magnitude of blade two's pitching moment when it had a pitch error of 3° is nearly the same as the pitching moment of blade three when it had the same pitch error. Note that the mass imbalances were evenly distributed throughout the affected blade section(s). If the mass imbalance were concentrated on the leading or trailing edge of the blade, it is feasible that this too may increase the pitching moment of the blade.

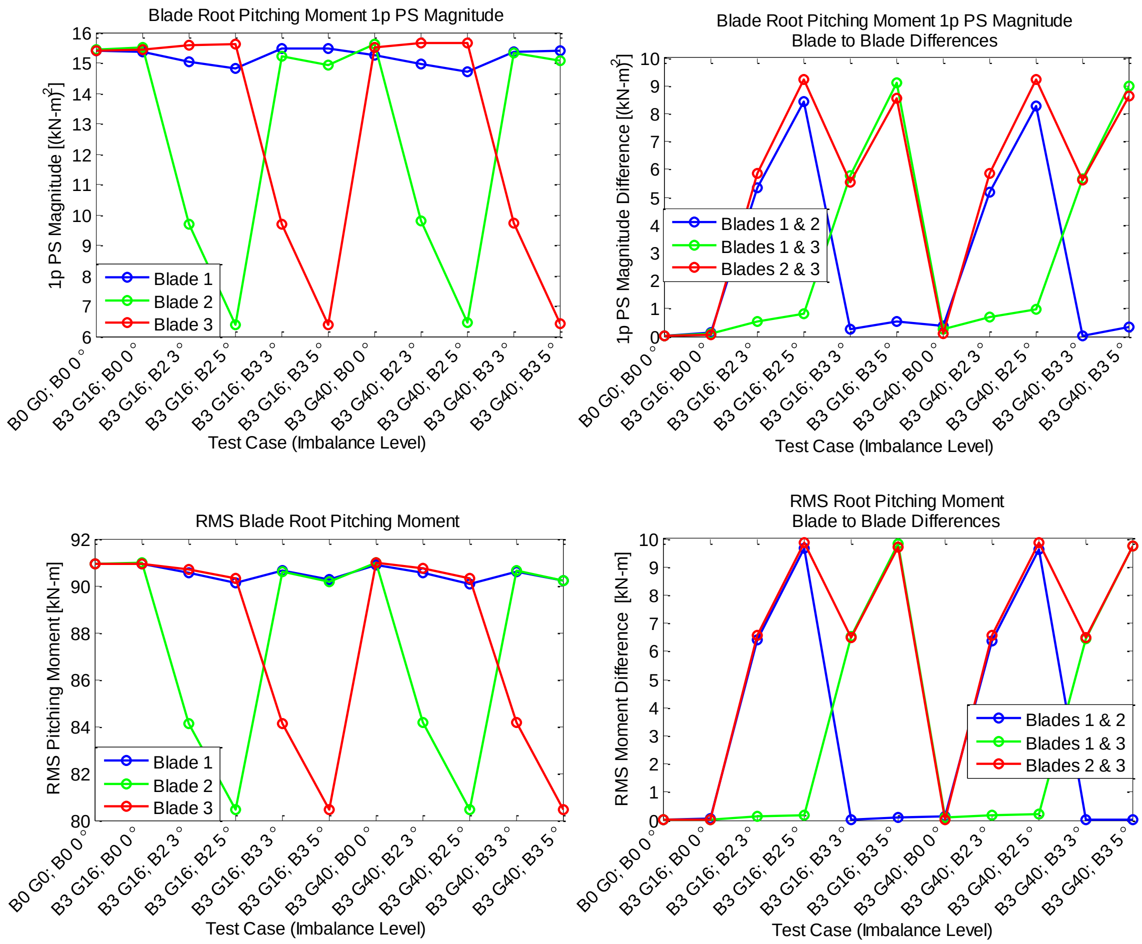

Figure 41. RMS, 1p PS, and blade-to-blade differences of blade root pitching moments for simultaneous mass imbalance and pitch error

4.5.3.3. Blade Root Axial Force

Figure 42 displays the blade root axial forces as well as the blade-to-blade differences in the measured forces. If the axial force was due entirely to centrifugal force, then the blade containing additional mass (blade 3) should always produce the largest axial force. However, this is not the case. When blade 2 is pitched, even for the larger G40 mass imbalance, the pitch error results in a larger axial force on the pitched blade than on the blade with increased mass. This effect results from the blade center of mass not being coincident with the pitch axis along which the axial force is being measured. As shown in Figure 43, the centrifugal force, F_c, is directed radially through the blade center of gravity. When the blade is pitched, θ_A, the angle from the hub to the pitch axis remains fixed, while θ_{CG}, the angle from the hub to the line of action through the center of gravity approaches θ_A. The axial force being measured is the projection of F_c onto the pitch axis, that is:

$$F_{Axial} = F_C \cos(\theta_A - \theta_{CG}). \quad (15)$$

Therefore, because the quantity (θ_A-θ_{CG}) decreases as a blade is pitched, the measured axial force increases. Consequently, blade root axial force is not effective in distinguishing between mass and aerodynamic imbalance, and unlike what the mass-imbalance-only results of section 4.5.2.1 may suggest, it would not be effective in locating which blade was producing a mass imbalance if there were also aerodynamic imbalances present.

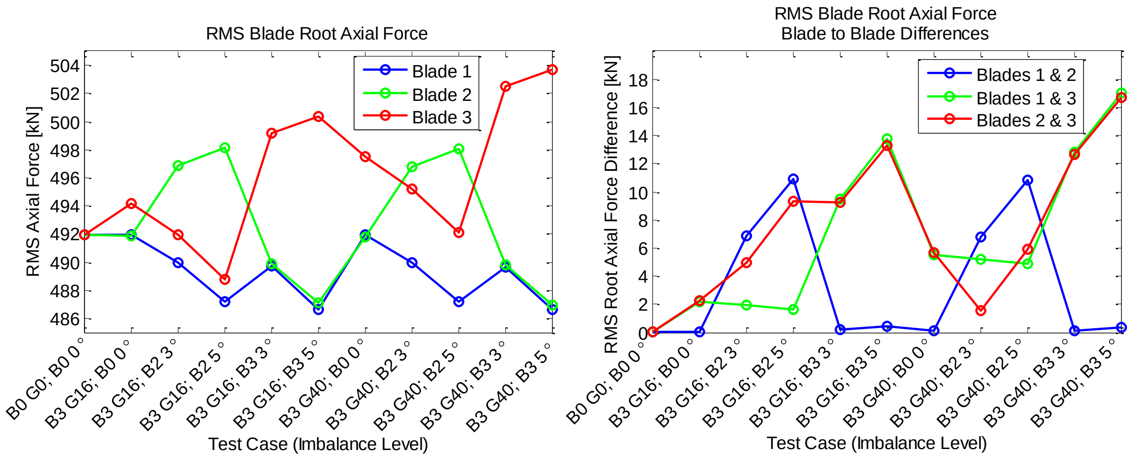

Figure 42. RMS blade root axial forces and blade-to-blade differences

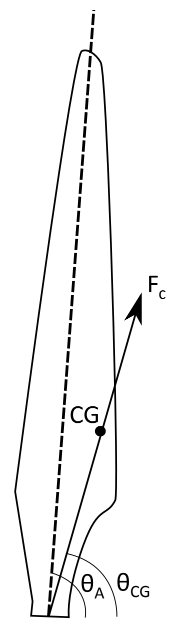

Figure 43. Blade center of gravity offset

4.6. Increased Loads due to Imbalances

An important result of rotor imbalances are the increased loads imparted to the turbine structure and drivetrain. The next three sections quantify load increases in the drivetrain, tower, and yaw joint as a result of pitch error, mass imbalance, and simultaneous pitch error and mass imbalance. The plots depict the percentage change in the forces and moments relative to the baseline simulation results.

4.6.1. *Pitch Error*

Pitch error resulted in significantly increased low speed shaft bending moments and shear forces. Figure 44 displays the low speed shaft bending moments at the shaft tip in the rotating reference frame about the y_a and z_a axes, LSSTipMya and LSSTipMza, respectively. It also shows the nonrotating low speed shaft shear force, LSShftFys, which is directed along the y_s axis and is constant along the shaft. All three forces and moments exhibited large increases due to pitch error, with percentage increases over 100% for as little as 2° error.

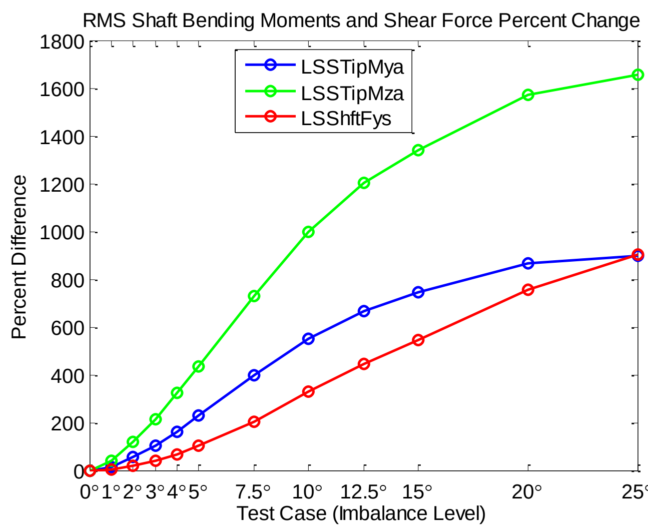

Figure 44. RMS Shaft bending moments and shear force percentage change due to pitch error

Several tower forces and moments also experience large increases, as indicated in Figure 45. The largest effect was on the tower yaw moment, labeled YawBrMzp in the figure. This moment increased from 124 kN-m to 434 kN-m for just a 1° pitch error, an increase of 250%, increasing by over 1700% for a pitch error of 5°. The plot on the right in Figure 45 adjusts the scale so the changes in the other forces are clearer. The tower-top/yaw bearing side-to-side shear force, YawBrFyp, as well as the moment about the y_p axis (see Figure 13 for coordinate system definitions), YawBrMyp, increase significantly as well. These forces and moments directly affect the yaw drive components in the turbine, which comprise a significant subsystem that experiences wear over a turbine's lifetime. The tower-top/yaw bearing roll moment (about the x_p) axis, YawBrMxp and the shear force at the tower top directed along the x_p axis decrease with pitch error, which may be expected due to decreased thrust from the pitched blade, as well as the slowed rotor for large pitch errors. These reductions, however, are much smaller than the increases in the other moments and forces.

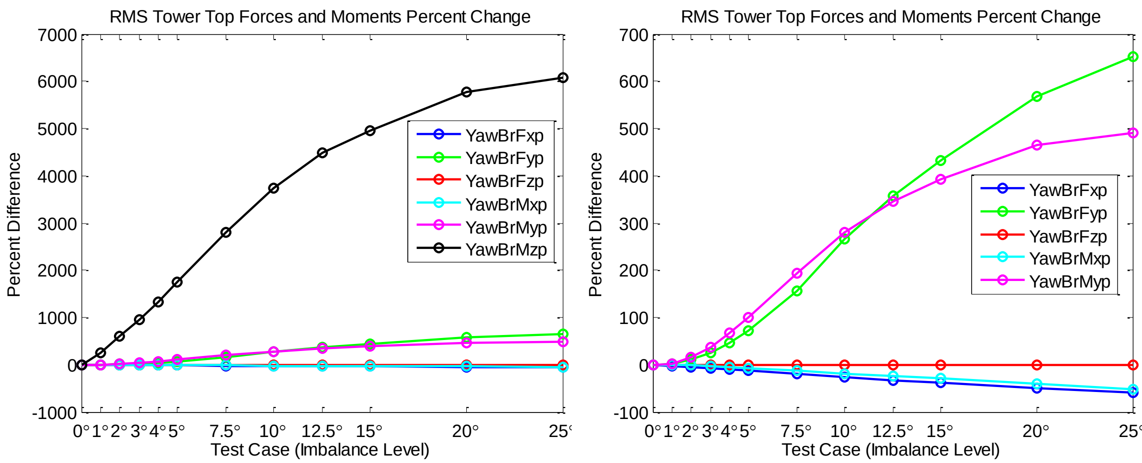

Figure 45. RMS tower top force and moment percent changes due to pitch error

The yaw (torsional) moment about the vertical tower axis at its base, TwrBsMzt, as well as the side-to-side shear force at the tower base, TwrBsFyt, also increase significantly due to pitch error as shown in Figure 46.

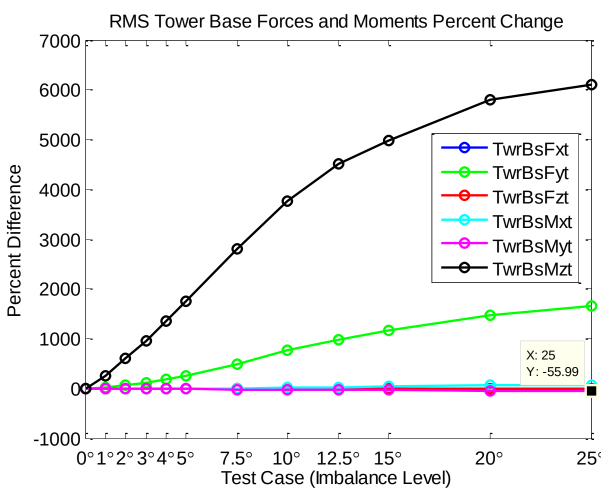

Figure 46. RMS tower base force and moment percent changes due to pitch error.

4.6.2. *Mass Imbalance*

As was shown previously, mass imbalances do not greatly affect the low speed shaft tip bending moments, but Figure 47 shows increases in the shear force. Even the permissible G16 imbalance grade produces an 8% increase, while the 0.5% blade mass imbalance, G53, results in a 60%

shear force increase. Moreover, Figure 48 indicates that the tower side-to-side shear force and yaw moment, YawBrFyp and YawBrMzp, respectively, increase due to mass imbalance.

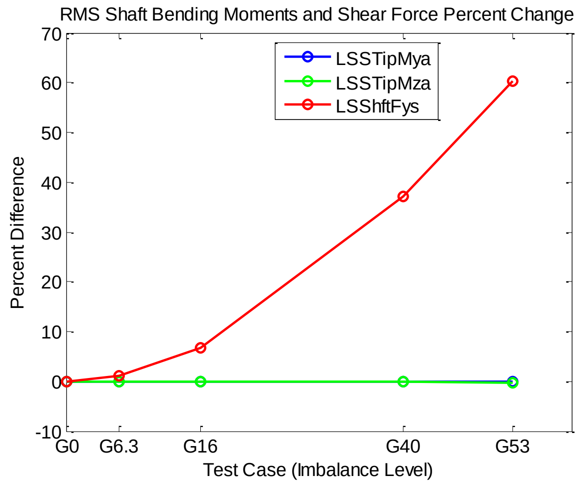

Figure 47. RMS Shaft bending moments and shear force percentage change due to mass imbalance

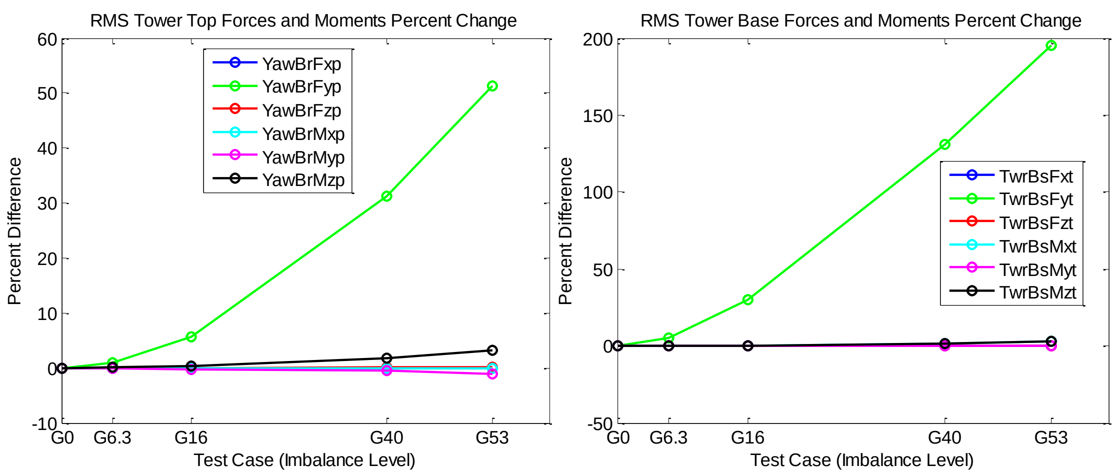

Figure 48. RMS tower force and moment percent changes due to mass imbalance

4.6.3. *Simultaneous Pitch Error and Mass Imbalance*

As would be expected, having both pitch errors and mass imbalances result in increased tower and drivetrain loads, as indicated in Figure 49, Figure 50, and Figure 51. These asymmetric loads propagate from the blades through the low speed shaft to the gearbox, tower, and other drivetrain components.

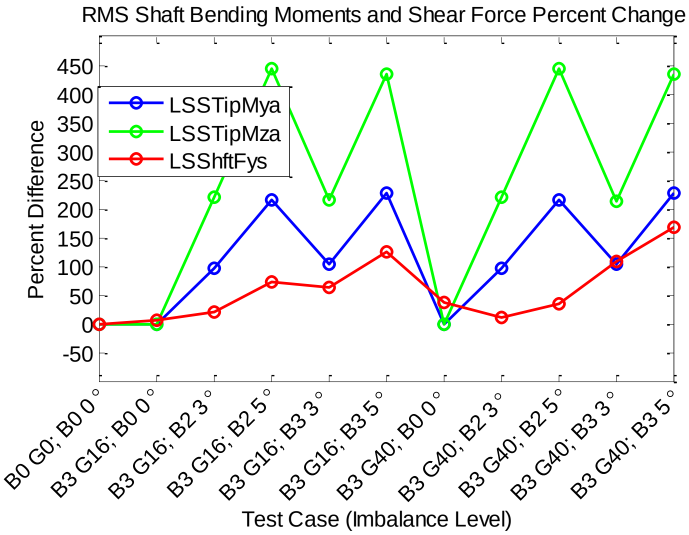

Figure 49. RMS shaft bending moments and shear force percentage change due to simultaneous pitch error and mass imbalance

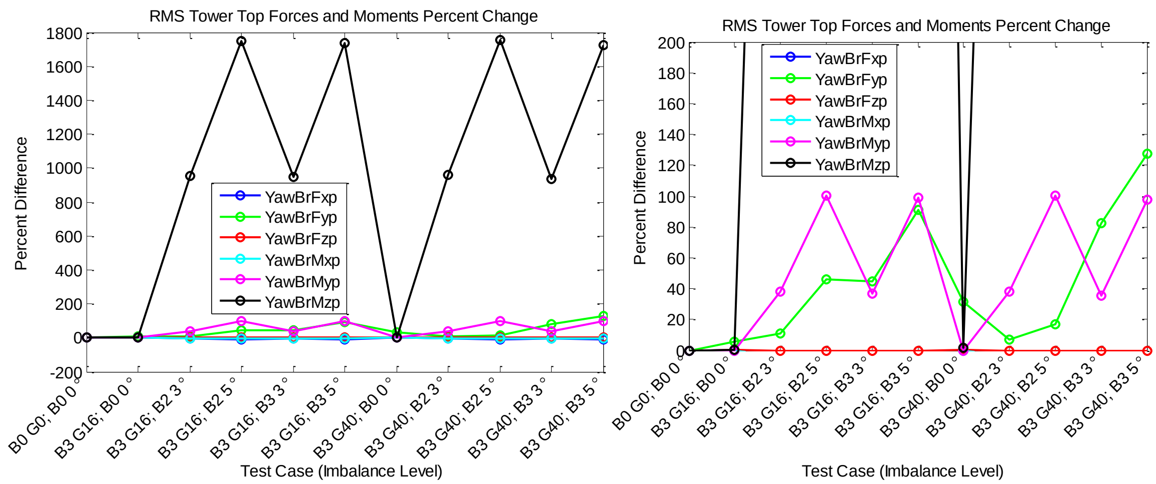

Figure 50. RMS tower top force and moment percent changes due to simultaneous pitch error and mass imbalance

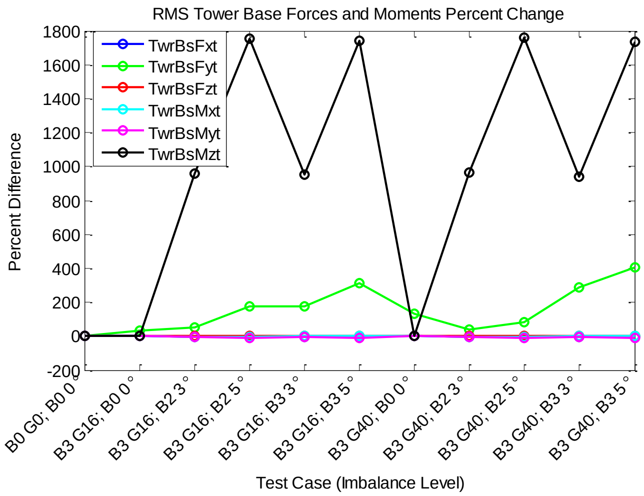

Figure 51. RMS tower base force and moment percent changes due to simultaneous pitch error and mass imbalance

4.7 Summary of Imbalance Detection Strategy

The results of these analyses of the operational response of a wind turbine rotor to various types and levels of rotor imbalance can be synthesized into a flow chart, as shown in Figure 52, for detection of rotor imbalances using a combination of sensors and analysis methods. This strategy utilizes both blade and non-blade sensor measurements. None of the methods evaluated thus far were successfully able to identify the blade having a mass imbalance; however, based on the above sensitivity studies of various imbalance conditions several methods have been developed to detect the presence of pitch error, its severity, as well as to identify which blade the pitch error is present. Therefore, and in summary, the strategy is as follows:

(1) Detect if an imbalance exists in the rotor

(2) Determine if the imbalance is strictly a mass imbalance, or whether it is a pitch or pitch and mass combination (it cannot yet be distinguished if there is just a pitch error or a simultaneous pitch error and mass imbalance at this stage)

(3) If the error is due to pitch or pitch and mass, determine which blade is pitched incorrectly and by how much. Correct this blade pitch through the blade control algorithm.

(4) Iterate until pitch error has been eliminated. If a mass imbalance is still present, it will then be identified, including which blade is the source of the imbalance.

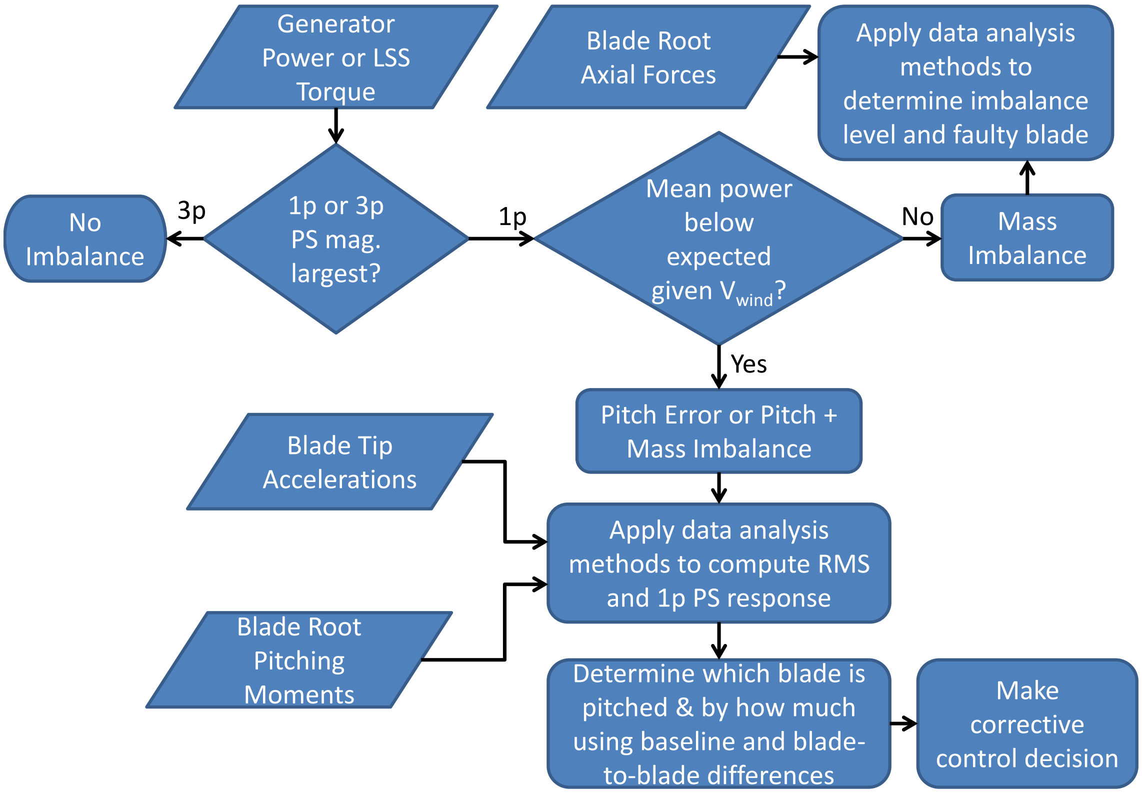

Figure 52. Pitch error and mass imbalance detection flow chart

5. SHEAR WEB DISBOND SENSITIVITY STUDY

5.1. Introduction

The developed multi-scale modeling methodology was utilized to investigate the sensitivity of a wide range of potential operational measurements to the presence of a shear web (SW) disbond. This representative form of damage was chosen because it is a damage mechanism that is routinely seen in the field. For this initial investigation all of the disbonds were assumed to have initiated at max chord of the blade (at the 14.35 meter span location) and propagated outwards toward the tip of the blade. This section includes a variety of different sensitivity analyses that were conducted at various stages throughout the modeling and simulation processes.

5.2. Shear Web Disbond Damage Modeling Methodology and Simulation Methods

To model the presence of a shear web disbond on a wind turbine blade, the NuMAD blade model was modified so that shear web nodes were split into two different nodes. This effectively split the blade model at the shear web in a similar way to how the blade is physically constructed through bonding the high pressure clam shell to the shear webs. To simulate a healthy bond across the blade, the top and bottom shear web nodes were connected using constraint equations in all six degrees of freedom. In the area of the blade in which the shear web disbond existed, the constraints were removed so that there was no connection between the top of the blade and the shear web. A similar approach was done by Griffith, et al. (2011, Reference [16]) to simulate a trailing edge disbond on the same blade model. While this modeling disbond methodology is effective in modeling a disbond in which the blade and shear web do not come into contact, it fails to take into account the possible interaction of the top and bottom surfaces of the disbond. For large cracks in which interaction between the top of the blade and the shear web may have a significant influence, the relative decrease in stiffness due to the disbond is likely over-estimated because the added stiffness due to the disbond face interaction was not taken into account. Modeling the interaction between the two surfaces could be achieved using nonlinear surface contact constraints between the top of the blade and the shear web but this was not accomplished during this initial investigation and remains as future work.

FAST simulations were performed for several wind profiles and turbine blade conditions. Among the wind profiles used were constant wind speed and direction, IEC Kaimal Model with A turbulence, IEC Kaimal Model with B turbulence, and the NREL NWTC wind model with a KHTEST intense disturbance. For the constant wind profile, the wind speed was set to 11.4 m/s, with a 1/7 power law vertical shear profile. The IEC Kaimal model is defined in IEC 61400-1 2nd ed. [29] and assumes neutral atmospheric stability. A mean wind speed of 13 m/s was used. The spectra for the three wind components, K = u, v, w, are given by

$$S_K(f) = \frac{4\sigma_K^2 L_K / \bar{u}_{hub}}{(1 + 6fL_K / \bar{u}_{hub})^{5/3}} \tag{16}$$

where f is the cyclic frequency and L_k is an integral scale parameter. More information can be found in IEC 61400-1 [29] or the *TurbSim User's Guide* [30].

The NREL NWTCUP model represents turbulent inflow characteristics at the NWTC, downwind of a major mountain range. A mean wind speed of 13 m/s was used. For neutral and stable flows, the NWTCUP spectra are defined by adding scaled versions of the SMOOTH-model spectra:

$$S_K(f) = \sum_{i=1}^{NumPeaks_K} p_{i,K} S_{K,SMOOTH}(F_{i,K} f) \tag{17}$$

where $NumPeaks_K = 2$ for all wind components $K = u, v, w$ and the function $S_{K,SMOOTH}$ is defined within the SMOOTH model. More information can be found in the *TurbSim User's Guide* [30].

The sample time spacing was 0.01 seconds, corresponding to a sample rate of 100 Hz. Since the per-revolution harmonics were mainly of interest and the maximum rotor speed was 12.1 rpm, or 0.2 Hz, this sample rate was sufficient. Simulations were conducted under three conditions: (1) all three blades are healthy, (2) one of the three blades having a 5-meter shear web disbond, (3) one of the three blades having a 10-meter shear web disbond. Two hundred output variables were recorded from the simulations, including generator power, blade root moments, tri-axial blade accelerations along the span, nacelle accelerations, and many others. The first 30 seconds of simulations were discarded in analyzing the data to allow any startup transients to damp out, which was also performed for the imbalance simulations. The total simulation time for each test, eliminating the first 30 seconds, was one hour, allowing for averaging to take place.

5.3. ANSYS Strain Field Results and Shear Web Disbond Sensitivity

As was done in FY11 (Reference [16]), aerodynamic loads from the full system aeroelastic simulation can be translated to a set of equivalent forces for application to finite element nodes in the blade model. This corresponds to the "Local Sensitivity" step in the multi-scale simulation methodology. Figure 53 shows the 5-MW blade model with force vectors representing the steady aerodynamic load for normal operation at 11.4 m/s wind speed.

Figure 53. Force vectors representing aerodynamic load applied to the 5-MW blade finite element model

A 5 meter long shear web disbond, representing 8.13% of blade span, has been modeled in the detailed blade model. The response of the blade structure to the applied aerodynamic forces was computed for both healthy blade and damaged blade and localized displacements were determined in each element for both scenarios. The displacements for healthy and unhealthy blade are shown in Figure 54. As a result, the displacements increased across the blade for the damaged blade model and the tip deflection increased from 4.31512 meters to 4.31937 meters (or 0.0985% increase). The span-wise strain field is shown in Figure 55 for the blade with the 5 meter shear web disbond. Near the disbond on the shear web there was a clear redistribution of strains (50-160 micro-strain).

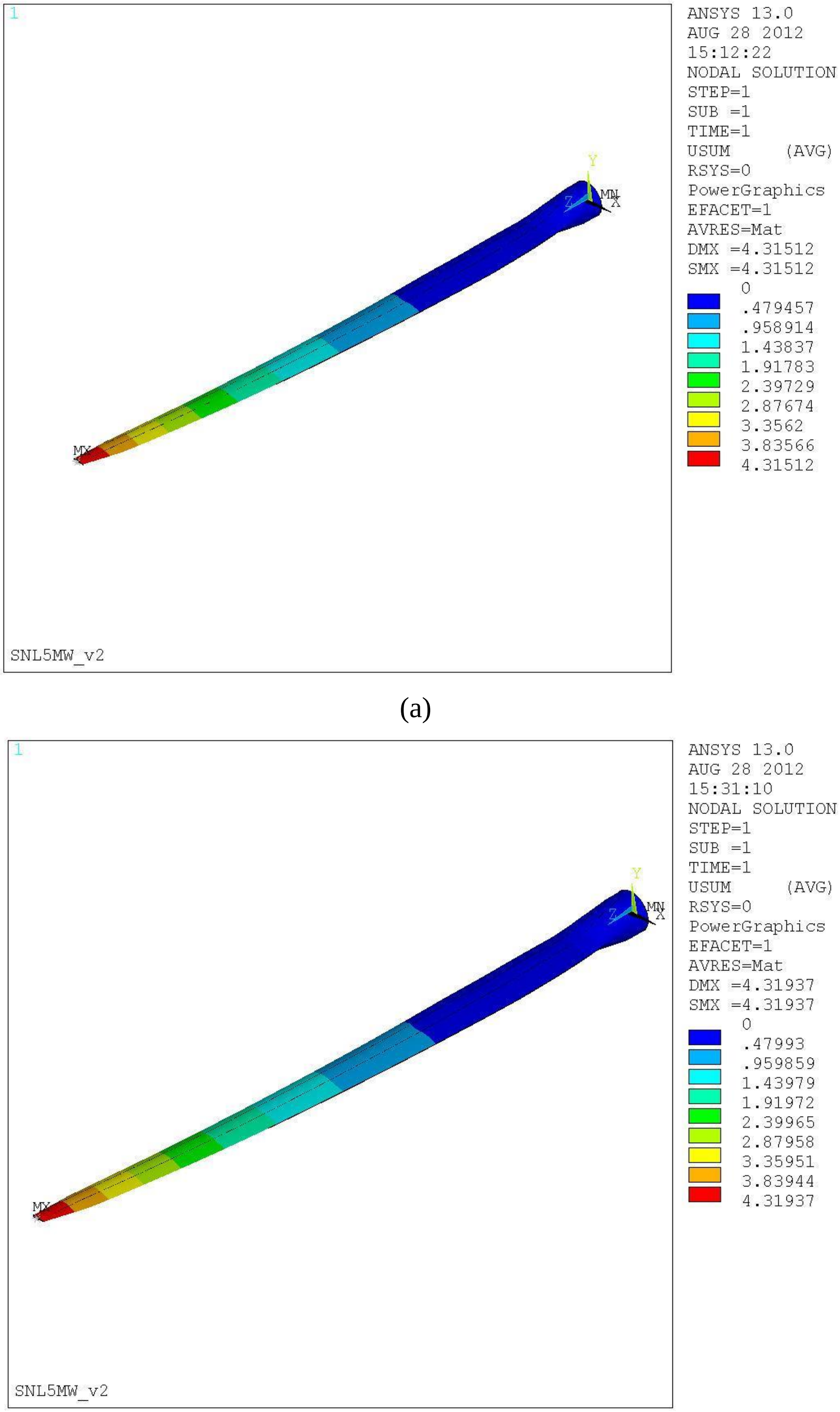

(a)

(b)

Figure 54. Blade deflections for (a) healthy blade and (b) blade with 5 meter SW disbond

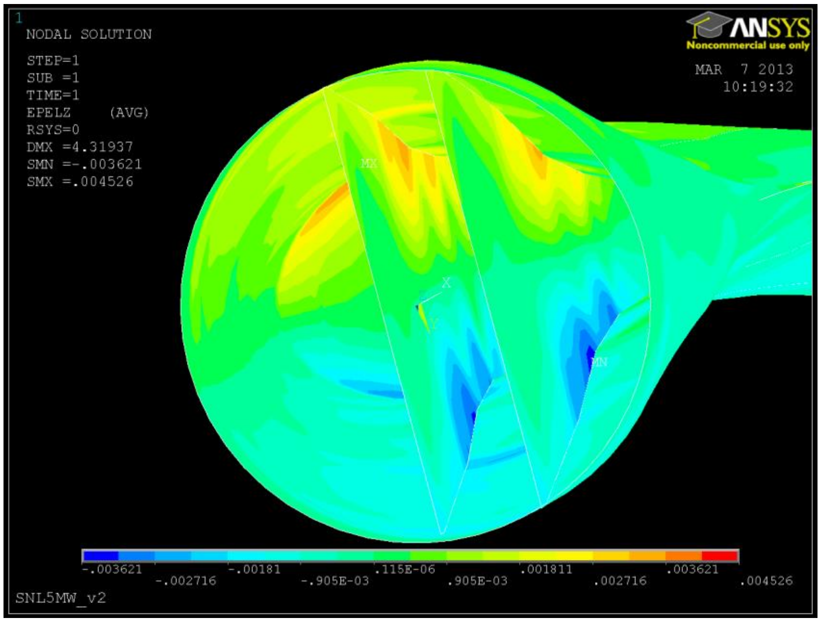

Figure 55. Span-wise strain field for blade with 5 meter SW disbond

The sensitivity of the extracted stiffness values to the shear web disbond was determined by calculating the percent decrease in each of the stiffness values for all of the sections in the reduced order model. Figures 56-59 show the percent decrease in flap-wise, edge-wise, torsional, and axial stiffness, respectively. The effect of the disbond is shown for the health (blue), 5 meter disbond (green) and 10 meter disbond cases (red). Clearly the effect of the disbond is localized at the location of the disbond and correlated in magnitude with the extent of the disbond. The blade with a 10 meter shear web disbond clearly showed an increase in percent decrease in all of the evaluated stiffness values for blade stations 10 and 11. The disbond had the largest effect on torsional stiffness in those blade sections, although the effect on flap-wise stiffness was nearly as large. The reduction in torsional stiffness in the model suggests that the torsional operational responses may be the best indicator in the case of SW disbond.

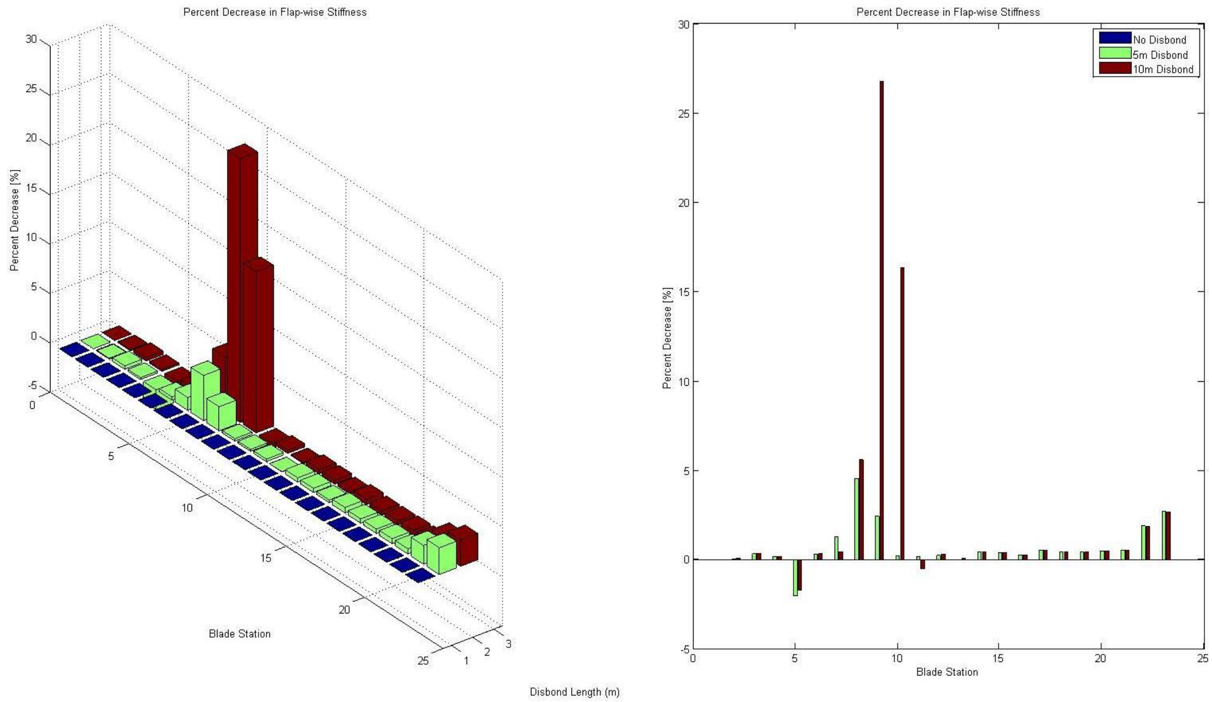

Figure 56. The percent decreases of the flap-wise stiffness value for varying length disbonds for segments spaced along the length of the blade.

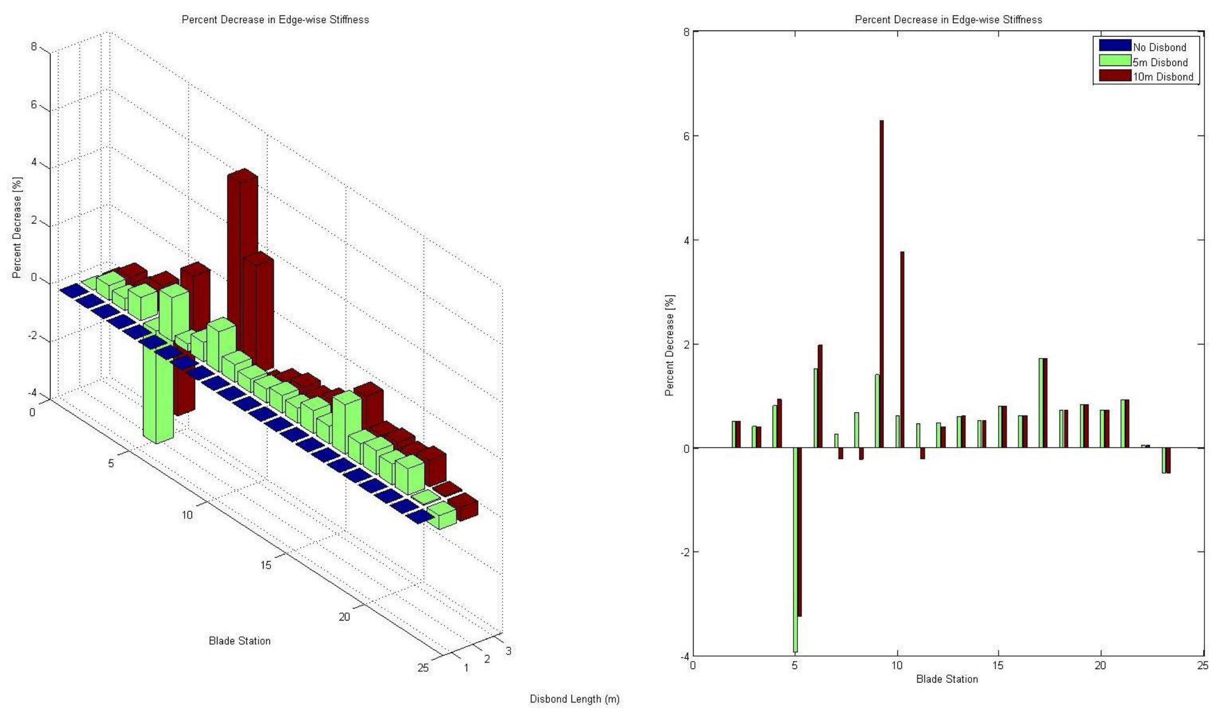

Figure 57. The percent decreases of the edge-wise stiffness value for varying length disbonds for segments spaced along the length of the blade.

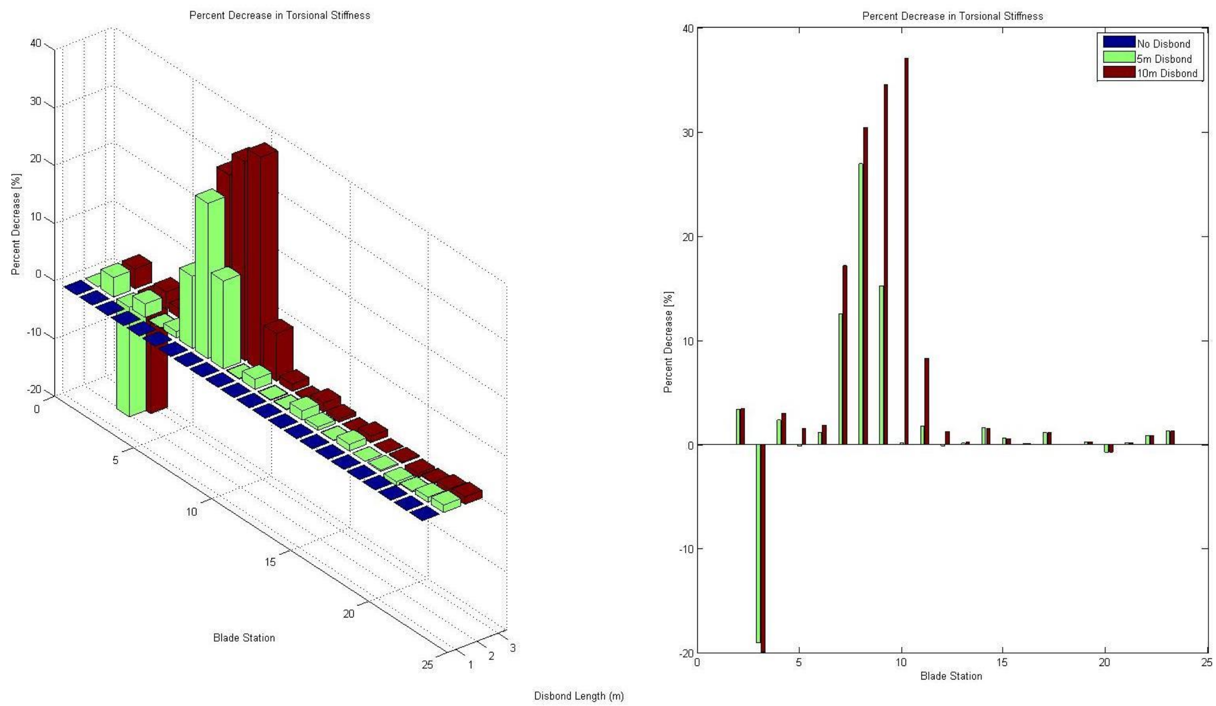

Figure 58. The percent decreases of the torsional stiffness value for varying length disbonds for segments spaced along the length of the blade.

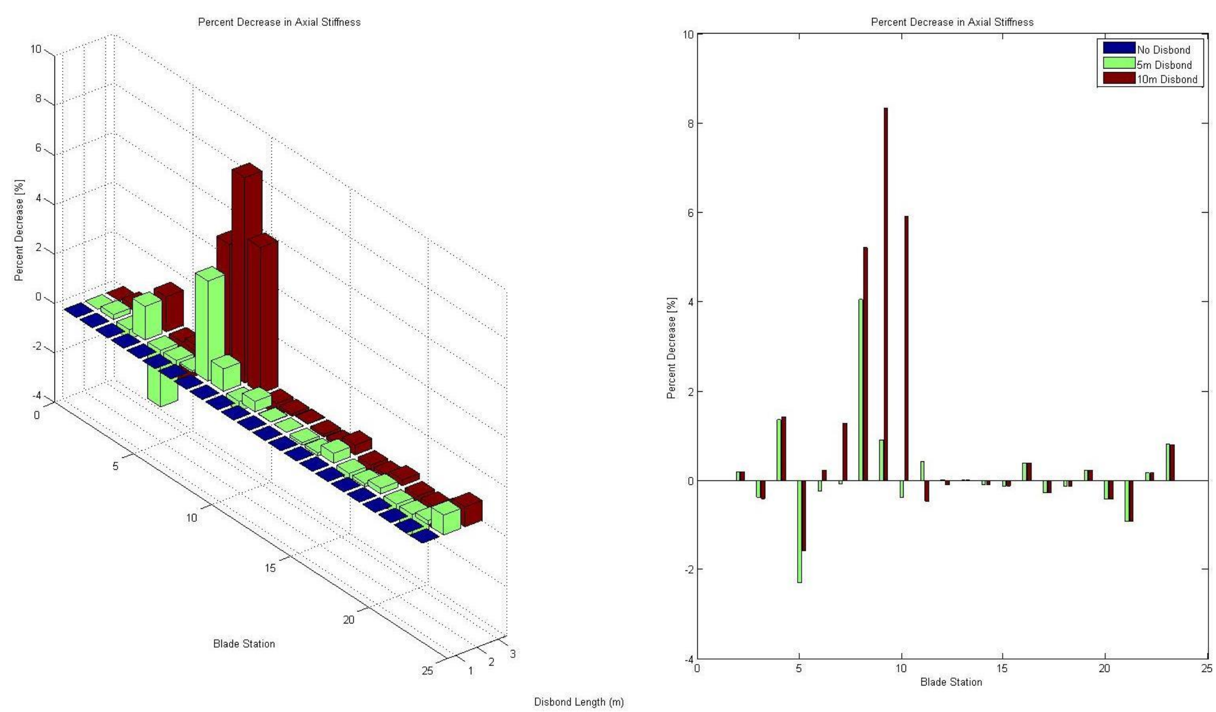

Figure 59. The percent decreases of the axial stiffness value for varying length disbonds for segments spaced along the length of the blade.

5.5. Analysis of Shear Web Disbond without Blade Sensors

In order to compare the effectiveness of shear web disbond detection methods with and without blade sensors, algorithms were first generated for determining the disbond using only the outputs from FAST that would not require blade-mounted sensors. From the 200 variables that are provided as output from the FAST simulation, those which displayed significant percentage changes in their RMS value or frequency response magnitude at the operating speed given a shear web disbond were identified as key measurement channels. The rotor azimuth position output from FAST was used as the reference signal for time synchronous averaging. The rotational resampling was performed in the same way as described above in the rotor imbalance studies. The azimuth signal was converted to radians, unwrapped and then the measurement signal was interpolated so that each revolution contained the same number of data samples with each sample corresponding to the same azimuth position of the rotor's rotation. Finally, blocks of three revolutions of data were averaged together. More than one revolution was used in the block size to increase the length of the block's time history, thereby increasing the frequency resolution of the DFT of the averaged signal. The shear web disbond detection algorithms for non-blade sensors all functioned in a similar way: detecting changes from baseline measurements either in the RMS response or 1p power spectral density magnitude.

5.5.1. *Shear Web Disbond Analysis Results*

The following sections summarize the trends in the results for shear web disbond, as measured in the generator power output and nacelle inertial sensors.

5.5.1.1. Generator Power

Overall, the generator power output did not change significantly between the healthy model and those models with a shear web disbond. Interestingly, a phase shift occurred in the synchronously averaged power output under the presence of a SW disbond. However, the RMS power output did not change more than ~0.035% when the three turbine models were examined under the four different wind profiles.

5.5.1.2. Nacelle Inertial Measurements

For all of the following discussion, axial nacelle acceleration will refer to acceleration in the x_s direction, vertical nacelle acceleration (or tower axis) will refer to acceleration in the y_s direction, and transverse (or side-to-side) nacelle acceleration will refer to acceleration in the z_s direction (all directions as defined in Figure 11). For all wind cases, nacelle accelerations increased in all three directions with the presence of the shear web disbond. In addition, the percent changes were correlated with the extent of damage (i.e. length of the disbond). In addition, the x_s and y_s 1p response differences as well as the RMS differences in the z_s direction indicated the presence and severity of disbond. However, no feature could be extracted to indicate which blade contained the damage. Figure 60 shows the 1p PS magnitude percent change of nacelle acceleration in the z_s direction and Figure 61 shows the RMS percent change of nacelle acceleration in the y_s direction.

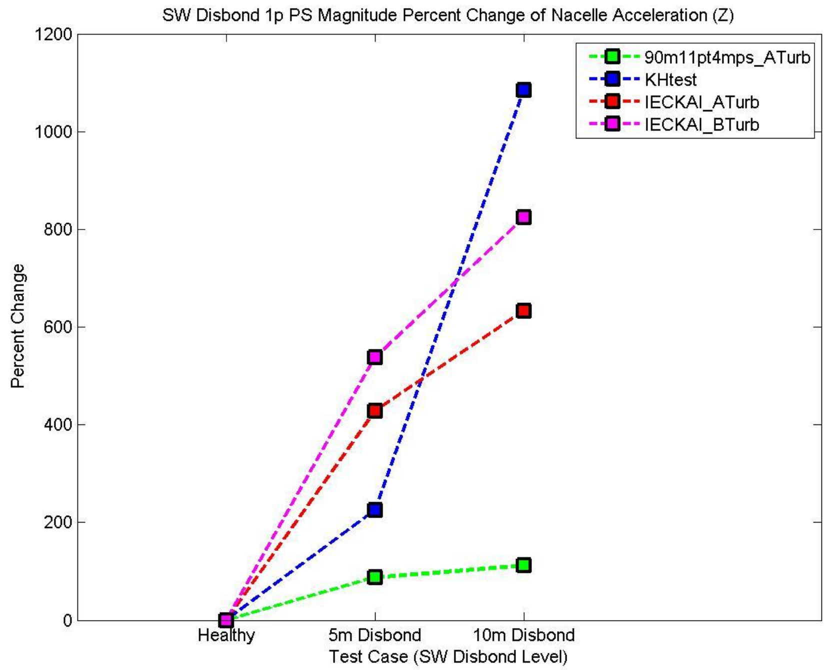

Figure 60. 1p magnitude percent change of nacelle acceleration in the z_s direction for shear web disbond

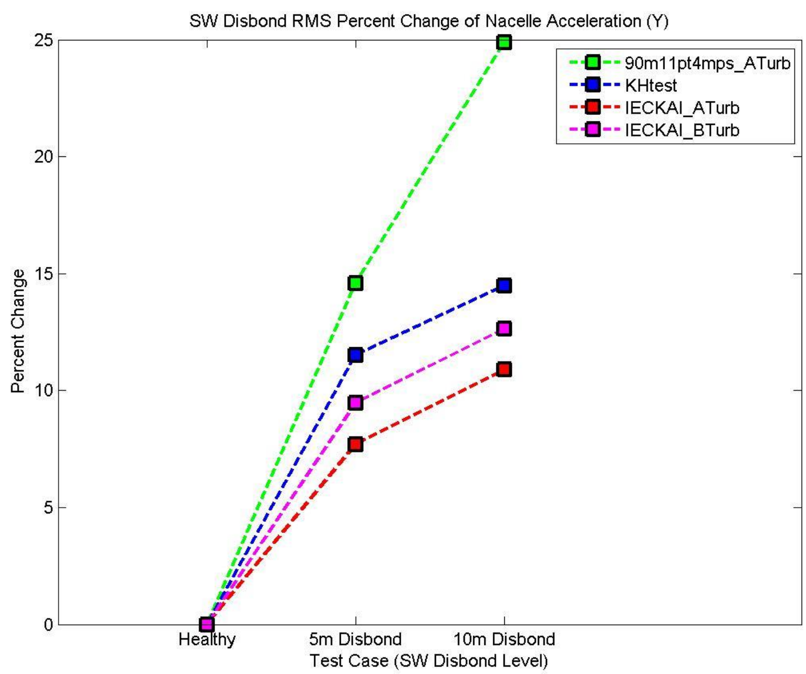

Figure 61. RMS percent change of nacelle acceleration in the y_s direction for shear web disbond

5.6. Analysis of Shear Web Disbond with Blade Sensors

Section 5.5 illustrated that some non-blade measurements are sensitive to the presence of a shear web disbond in one of the three blades, but they lacked the ability to determine which blade(s) contains the disbond. The next sections will investigate outputs from the FAST simulations that would depend on blade-mounted sensors in an operating turbine.

5.6.1. *Shear Web Disbond Analysis Results*

The following sections summarize the trends in the results for shear web disbond, as measured in blade tip acceleration responses, blade root bending moments and flap-wise acceleration response.

5.6.1.1. Blade Tip Acceleration Response

The blade tip acceleration response in all three directions showed positive trends as the shear web disbond was introduced and increased in length. The 1p edge-wise blade acceleration response differences are shown in Figure 62. These 1p response differences increased significantly with increasing shear web disbond (as much as a 25% increase for a 10 meter SW disbond). The blade tip span-wise acceleration 1p response differences (shown in Figure 63) and flap-wise acceleration RMS response differences (shown in Figure 64) also increase in the presence and increase of a shear web disbond. Note that the 1p magnitude percent change in the side-to-side nacelle acceleration was the most sensitive parameter to a shear web disbond, but the trend lines vary for the different wind profiles. On the other hand, the blade tip acceleration responses follow very similar trends for all four wind profiles.

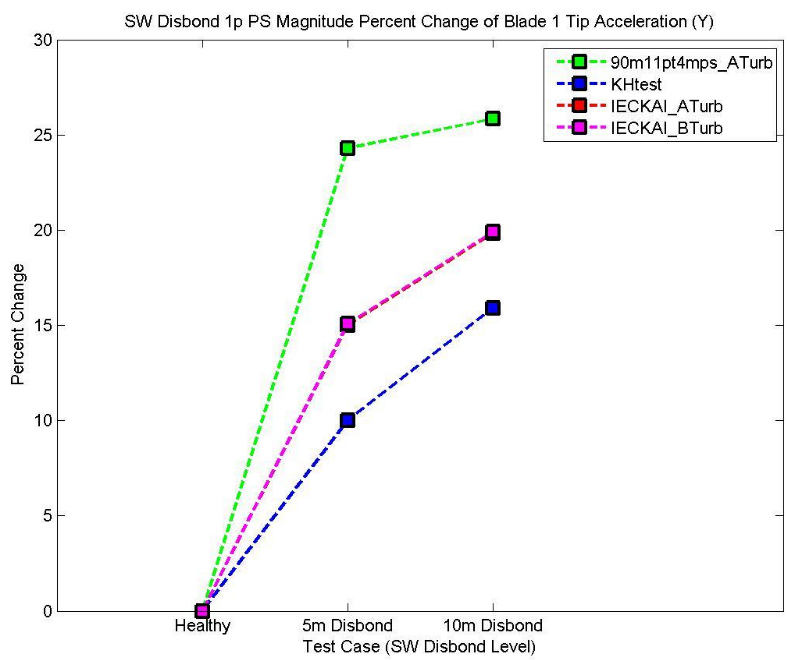

Figure 62. 1p magnitude percent change of edge-wise blade tip acceleration for shear web disbond

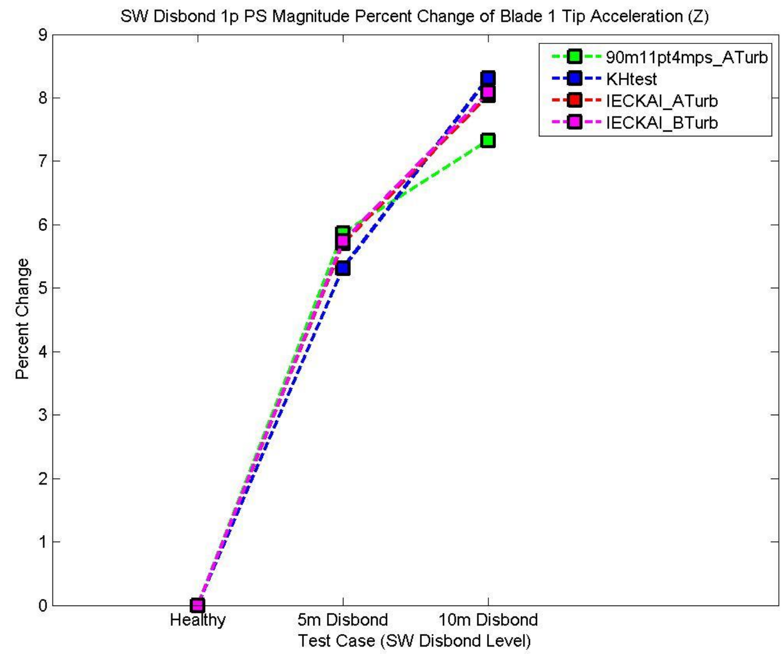

Figure 63. 1p magnitude percent change of span-wise blade tip acceleration for shear web disbond

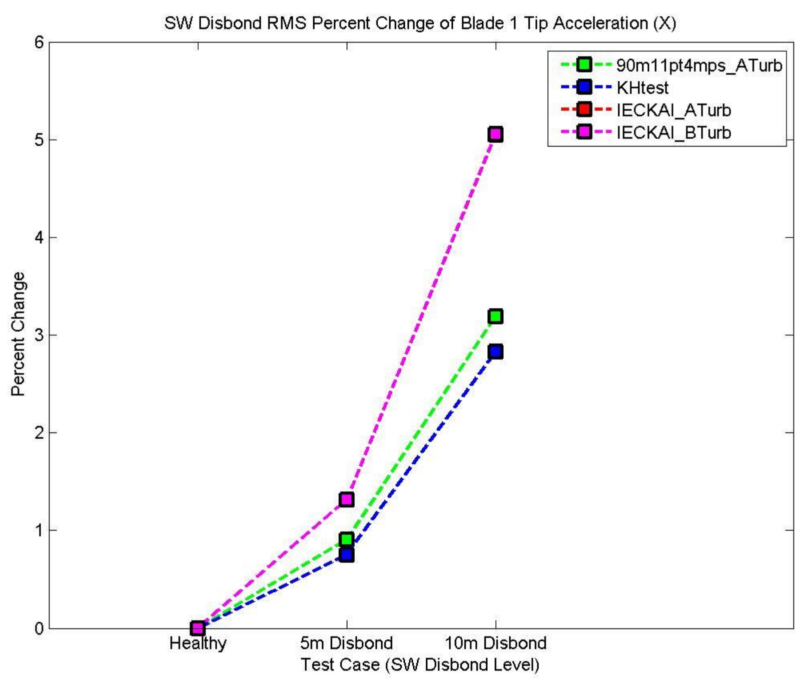

Figure 64. RMS response percent change of flap-wise blade tip acceleration for shear web disbond

5.6.1.2. Blade Root Pitching Moments

The moment of the blade about its pitch axis at the blade root is another good indicator of a shear web disbond, as shown here. This moment can be measured using strain gages located at the root of each blade and this parameter was also shown to be a good indicator of pitch error, as shown in Section 4.5.1.2. In addition, the FY11 report [16] detailed how the blade root pitching moment is also a good indicator of the presence of a trailing edge disbond. The blade root pitching moment 1p response differences (shown in Figure 65) increase while the RMS response differences (shown in Figure 66) are small and decrease with increased disbond length. The RMS response difference is very small, however the increase in the root pitching moment 1p response is expected since a shear web disbond would cause a reduction in torsional stiffness and the disbond originates at max chord, relatively close to the root of the blade. Both measurement sets also follow very similar trends for all four wind profiles as the shear web disbond is increased.

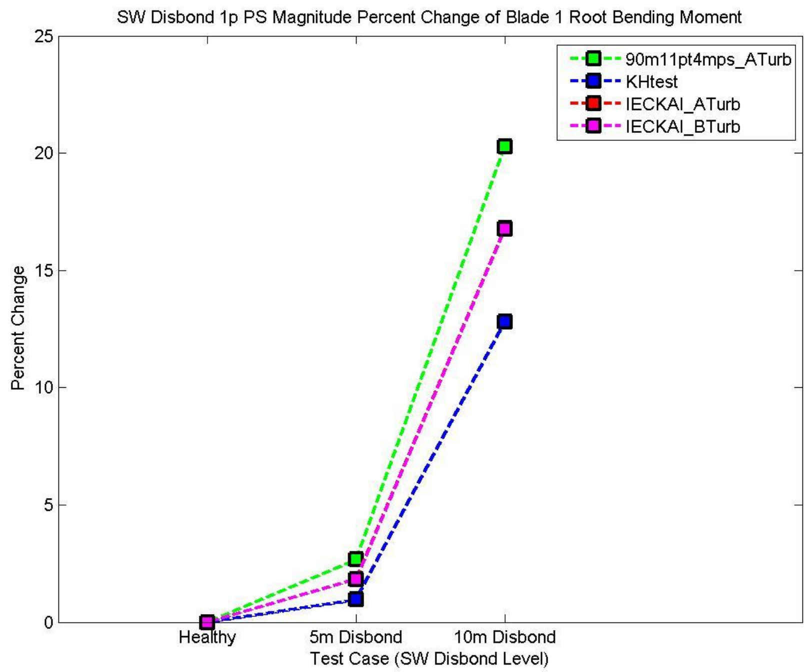

Figure 65. 1p magnitude percent change of blade root pitching moment for shear web disbond

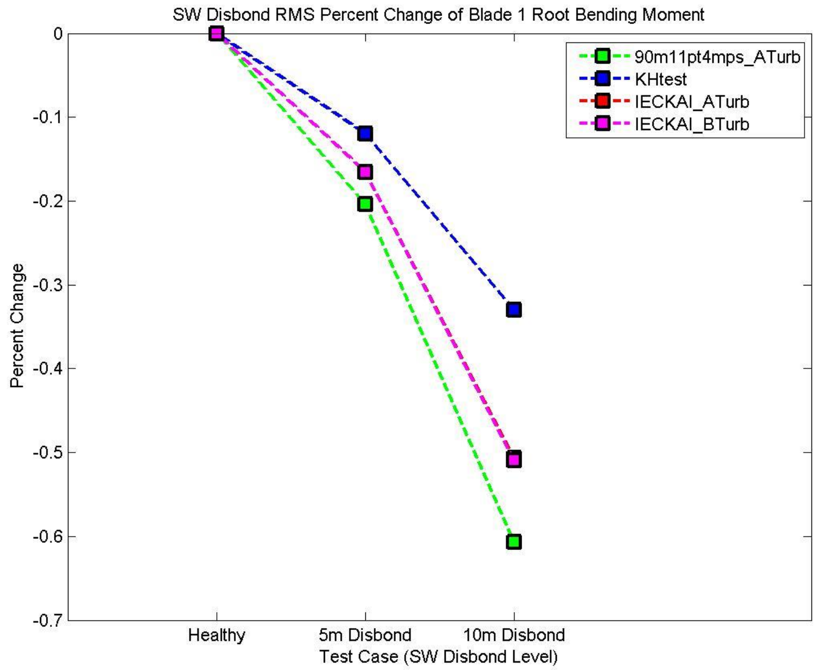

Figure 66. RMS response percent change of root blade pitching moment for shear web disbond

5.6.1.4. Blade Root Acceleration Response

The shear web disbonds produced notable differences in the blade root acceleration response in the flap-wise direction (see Figure 67). However, it is not yet clear how sensitive this parameter would be to a disbond located further down the span of the blade. Future work involving the analysis of shear web disbonds at different locations along the blade would provide better insight.

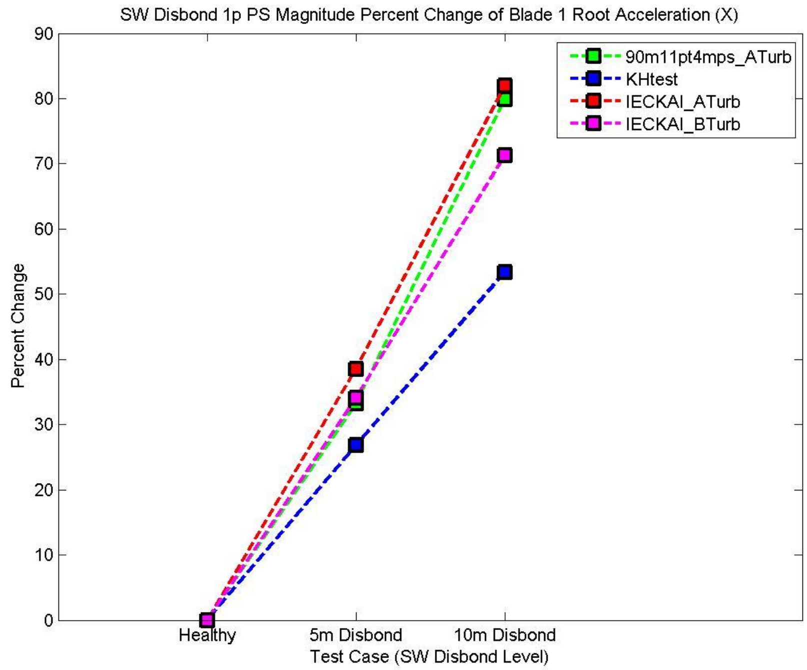

Figure 67. Blade root 1p flap-wise acceleration response differences for shear web disbond

5.7 Summary of Shear Web Disbond Detection Strategy

The results of these analyses can be synthesized into a flow chart, as shown in Figure 68, for detection of shear web disbonds using a combination of sensors and analysis methods. The proposed strategy is to:

(1) Detect if a shear web disbond exists in one of the blades

(2) Determine the severity of the shear web disbond

(3) Notify turbine operator of the disbond and severity so that a repair can be scheduled or coordinated with other maintenance

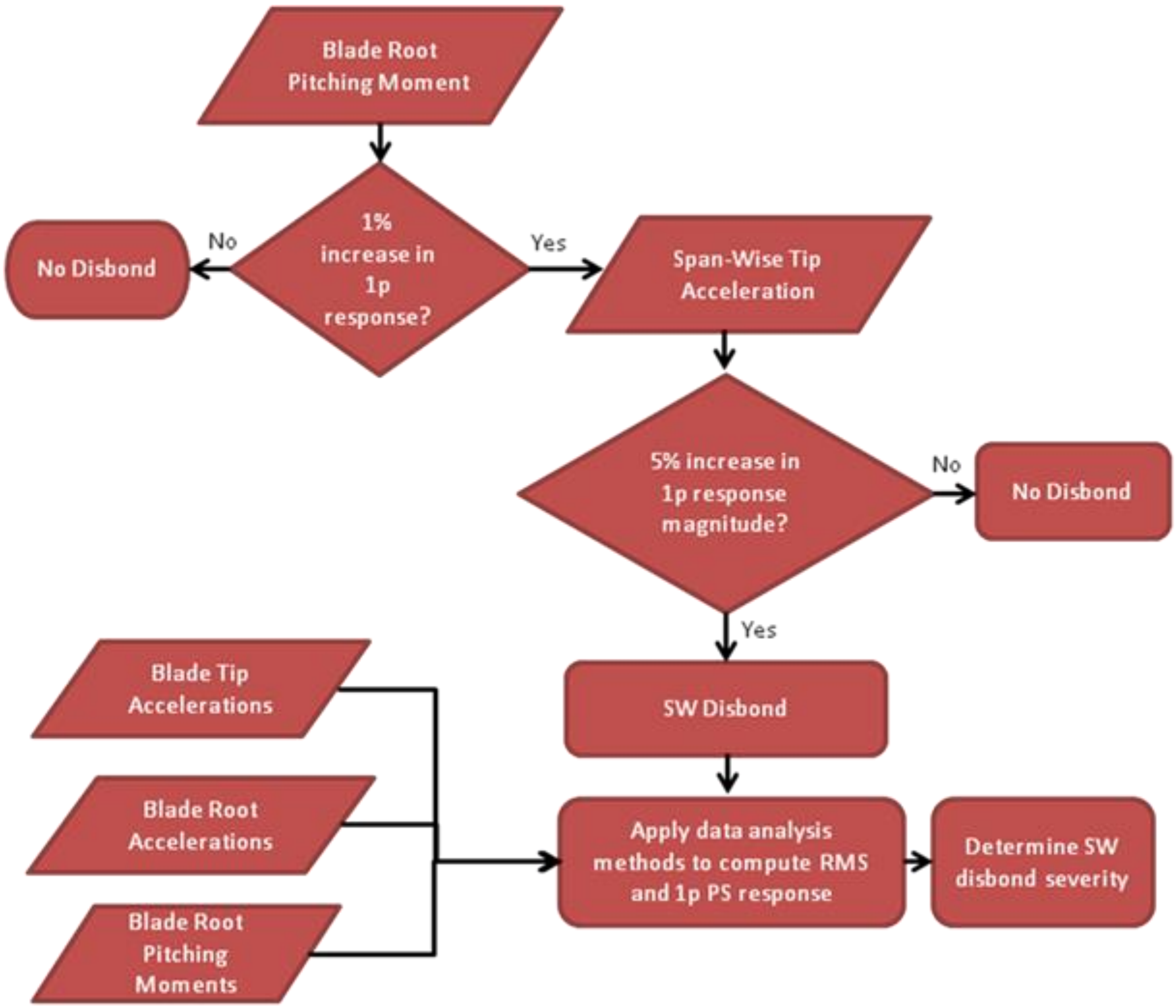

Figure 68. Shear web disbond detection flow chart

6. OPERATIONS AND MAINTENANCE COST MODEL DEVELOPMENT

This section covers the initial development of a cost model to determine the cost-benefit of the proposed blade SHPM system. Shear web disbond and mass imbalance were the defect mechanisms used to exercise the preliminary case studies for this cost model.

6.1 Literature Review

6.1.1 Wind Turbine Blade Cost Drivers

As noted earlier, determining the cost-benefit of the proposed SHM system is one of the key elements of this research. To better understand wind turbine SHPM costs, there needs to be an understanding of how the costs related to blade damage are calculated. Wind turbine researchers use the equation shown in Figure 69 to calculate the cost of energy [31].

$$COE = \frac{ICC*FCR + LRC}{AEP_{net}} + O\&M$$

COE- Cost of Energy ($/kWh)
ICC- Initial Capital Cost ($)
FCR- Fixed Charge Rate (%/yr)
LRC- Levelized Replacement Cost ($/year)
O&M- Operations and Maintenance Costs($/kWh)
AEP- Annual Energy Production (kWh/yr)

Figure 69. Cost of Energy Equation

Blade failures impact three categories of this equation: Levelized Replacement Cost (LRC), Operations and Maintenance Cost (O&M), and Annual Energy Production (AEP). Levelized replacement costs are impacted because total blade failures require a blade replacement. Operations & maintenance costs rise if blade repairs are unscheduled and require special equipment such as a crane. These costs also rise if there are more blade repairs than initially estimated. Annual energy production is decreased if the turbine is not operating due to damage in a blade or if there is a condition such as a pitch error that causes sub-optimal energy capture.

6.1.1.1 Levelized Replacement Cost

Wind turbine blades account for roughly 22% of the cost for a 5MW wind turbine [32], so the corresponding levelized replacement costs can increase significantly as blade replacements increase. The main driver of LRC is component life estimates [31]. If these estimates are lower than what is experienced in the field, then the LRC will be higher than expected.

6.1.1.2 Operations and Maintenance Cost

Operations and Maintenance costs account for 10 – 20% of the total COE for an onshore wind project; however, there is significant uncertainty in O&M Cost [31]. In fact, the difference between low and high estimates regarding impact on COE is approximately 10%. These uncertainties are cause by factors such as:

- Lack of data relating to component reliability since manufacturers maintain records of warranty claims
- Limited information on the root cause of failure
- Difficulty obtaining useful component failure
- Many variations on the basic horizontal-axis configuration

These factors are also present in offshore operations and maintenance where O&M can constitute as much as 30% of overall project costs [32].

6.1.1.3 Annual Energy Production

When the wind turbine is being repaired (or has failed) the AEP is lowered -- unless the wind is below the cut-in speed. Increased amounts of wind turbine repairs can cause a reduction of energy production during downtime which will increase the COE.

6.1.2 Cost Models

There are a number of cost models that have been created to try to quantify and understand the cost associated with wind turbines. For ease of review, these cost models have been assigned to three categories: general, component reliability, and decision models. The general cost models evaluate costs by generalizing costs such as maintenance costs across the wind turbine/farm and do not incorporate multiple decisions. The component reliability models evaluate cost through the use of component failure rates and component repair costs. Finally, the decision models evaluate cost by incorporating the decisions to be made into the model.

6.1.2.1 General Models

One of the general cost models uses average 5 year maintenance costs to determine the cost of energy over a 20 year period [33]. The model calculates the costs of maintaining the wind farm with a repair or replace strategy that performs maximum maintenance (returns the turbines to like new condition) and/or minimal maintenance (may only replace some parts). This model was the basis of the cost model for this study. Other models emphasized varying costs by geographic region or state (i.e. Wyoming) [34], wind farm layout or by the size of wind turbines used. The Monte Carlo Markov Chain was also used in studies. This process leverages state space analysis to determine turbine states (i.e. new, deteriorated, and failed), wind speeds, and other stochastic features.

6.1.2.2 Component Reliability Models

The studies that used component reliability either used values from reviewing field experiences or from industry contacts [35]. This highlights the fact that it is difficult to obtain reliability data without information from industry. The Weibull distribution was used in one of the studies to model turbine reliability and other studies used the exponential distribution. There were more general reliability models found than component reliability models and many of the component reliability models dealt with the gearbox.

6.1.2.3 Decision Models

The studies that employed decision-making models incorporated the possible decisions that could be made. For instance, one of the studies incorporated the weather conditions in the model to determine the feasibility of maintenance as part of the decision [36]. A few of the studies incorporated the Partially Observed Markov Decision Process (POMDP). This process can accommodate decisions where the outcome is partly probabilistic (i.e. weather conditions and turbine state) and partly deterministic (i.e. decision on whether to perform maintenance).

6.1.3 Wind Turbine Blade Reliability

Reliability is "the probability that an item will perform a required function without failure under the stated conditions for the stated period of time [37]." The mathematical definition of reliability can be found in Equation 18 where f(t) is the failure probability density function.

$$R(t) = 1 - F(t) = 1 - \int_0^t f(t)dt \quad (18)$$

Figure 70 shows a hypothetical bathtub curve. In reliability, the bathtub curve depicts the life of an average part. The beginning infant mortality failures are usually caused by manufacturing defects and many are caught in house by quality control methods. This first portion usually has a decreasing failure rate as manufacturers resolve the quality or material issues. The second portion is called the normal or useful life. This is the longest portion of a product's life and it has a constant failure rate. The end of life wear rate is an increasing rate and occurs when a product is at the end of its useful life. The Weibull distribution can characterize all three portions of the bathtub curve.

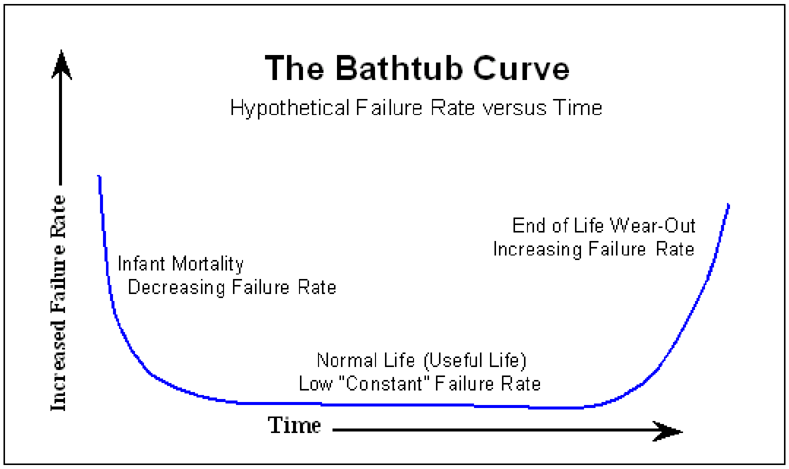

Figure 70. Bathtub Curve

The Weibull distribution is shown in Equation 19. A special case of the Weibull distribution where β equals 1, the exponential distribution, can characterize the useful life. The exponential distribution is shown in Equation 20.

$$f(t) = \lambda^{\beta} \beta t^{\beta-1} e^{-(\lambda t)^{\beta}} \quad (19)$$

$$f(t) = \lambda e^{-\lambda t} \quad (20)$$

For wind turbines, European studies indicate that electrical systems, blades/pitch, control system, hydraulics, and have the most number of failures [38]. In the United States, the top failures are reported as rotor/blades, electric generator, controls, yaw, and gearbox [39]. Blade failures are a concern since they are expensive and more time consuming than some other component repairs. The percentage of blade failures varies by manufacturer and location; however, blade failures are notable and shear web disbond and mass imbalance are two causes of blade failure.

6.2 SHPM Cost Model Description and Assumptions

The cost model used for this study is a state-space Matlab model that calculates O&M costs ($/MWh) of a wind turbine with and without a blade condition monitoring system for a period of 20 years. This preliminary cost model was developed to determine when and under what conditions a particular structural health monitoring system option will be economically viable. Figure 71 below shows the cost model flow chart and the following sections describe the inputs and outputs of each major portion of the cost model.

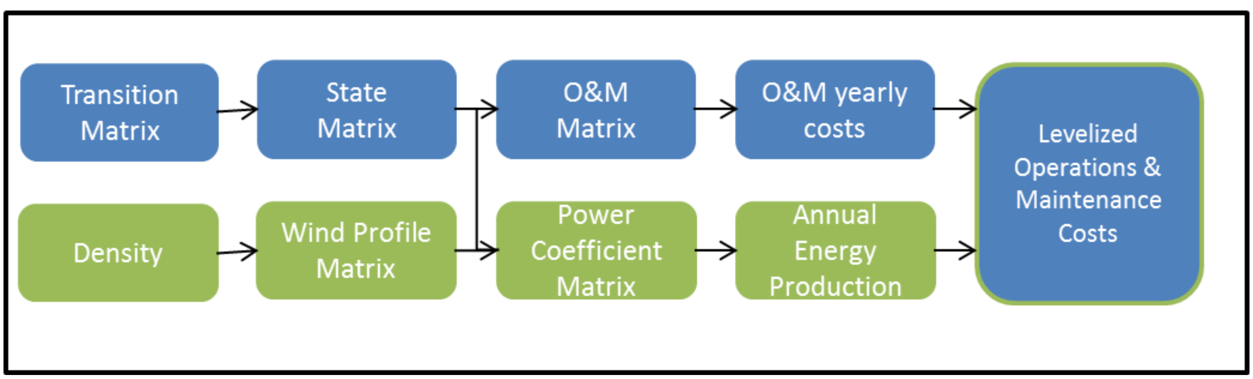

Figure 71. Cost Model Flowchart

6.2.1 Transition Matrix

The transition matrix is comprised of the probabilities (a_{ij}) shown in Figure 72 that dictate the probability of going from state i to state j, where state in this case refers to a state of health. A conceptual representation of the defect size versus the cost of repair for each of the four states of health used in this model is shown in Figure 73. State 1 is defined as small defects that do not need to be repaired, state 2 are moderate defects which can be repaired up-tower, state 3 are large defects which require blade removal, and state 4 are very large defects that require blade removal and replacement. The model moves from state to state based upon a random number (from 0 to 1) and the resulting states are for each step of one hour.

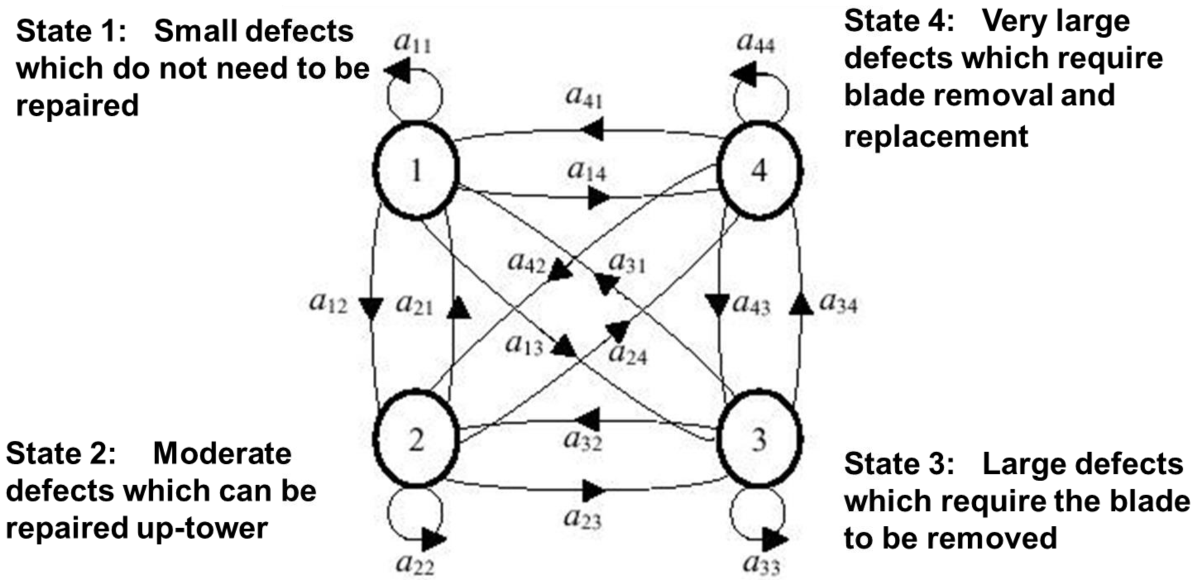

Figure 72. Markov Chain with Transition Matrix elements

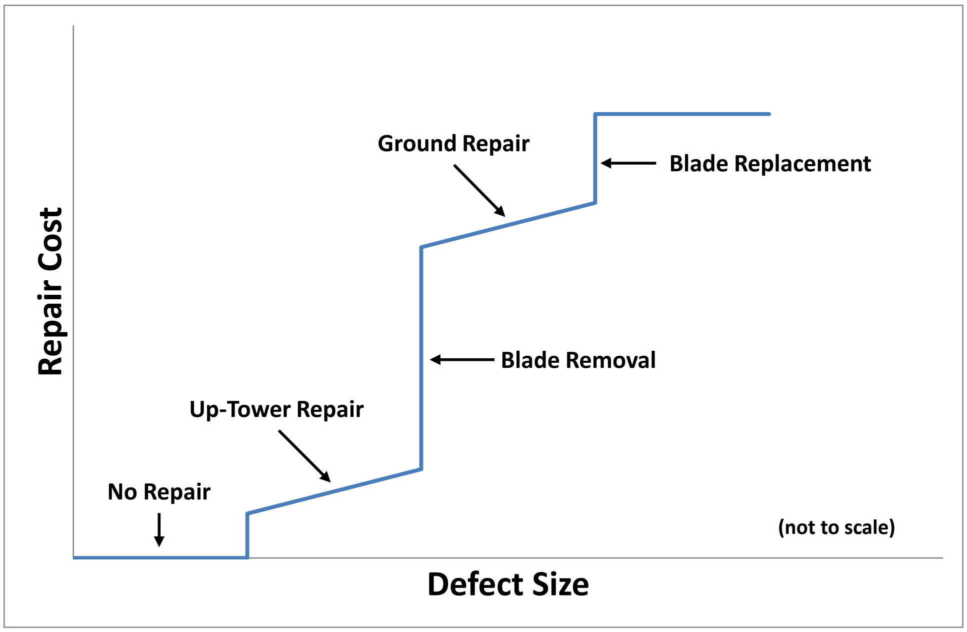

Figure 73. Example defect-cost model demonstrating the piecewise nature of defect size versus repair cost.

Figure 74 shows the transition matrix for the baseline SHM case. As seen below, there is a 0.88 probability that a blade at state 1 will remain in state 1 (a_{11}). There is a 0.175 probability that a blade at state 2 will remain in state 2 (a_{22}). A zero probability is inputted to prevent the blade from returning to a lower state without being repaired as seen by a_{32}. If a blade is currently at state 3, there is a 0.135 probability of it remaining in state 3, a 0.015 probability of it degrading further to state 4, and a 0.85 probability that it will be detected and fixed (returning it to state 1). The zero does not allow the turbine to spontaneously fix itself by going back to state 2 since one of the model assumptions is the turbine will be repaired once detected. Therefore, column 1 contains all of the probabilities of detection (a_{11}-State 1, a_{21}- State 2, a_{31}- State 3, a_{41}- State 4)

a_{11}	a_{12}	a_{13}	a_{14}
a_{21}	a_{22}	a_{23}	a_{24}
a_{31}	a_{32}	a_{33}	a_{34}
a_{41}	a_{42}	a_{43}	a_{44}

General transition matrix

0.88	0.07	0.046	0.004
0.75	0.175	0.06	0.015
0.85	0	0.135	0.015
0.96	0	0	0.04

Baseline Non-SHM transition matrix

Figure 74. Baseline SHM transition matrix

6.2.2 State Matrix

The inputs for the state matrix are the random number for that time interval and the transition matrix. The output is a matrix that shows the state of the turbine for each hour during a twenty year period. This matrix consisting of the previously described four states is used later to generate both the O&M and power coefficient matrices.

6.2.3 Operations & Maintenance Matrix

The inputs for the O&M matrix are the state matrix and a matrix that indicates the cost to return the blade from state 2 and higher to state 1. At state 1 the matrix has a value of 0 since no repairs are done at state 1. Table 3 shows the O&M matrix values that were used for the baseline case (both SHM and Non-SHM).

Table 3. O&M values for Baseline case

State	O&M
1	0
2	30
3	72.5
4	100

6.2.4 Wind Profile Matrix

The wind profile matrix was created with a random Weibull distribution with k=2 and c=11.4. The graph in Figure 75 shows the probability distribution function using the parameters from this study (average wind speed of 11.4 m/s). The values of the wind profile matrix are altered for the wind turbine used in this study. The wind speed is changed to zero for values below the cut-in speed and above the cut-out speed. Also, the speed is changed to the rated speed for all values between the rated speed and the cut-out speed.

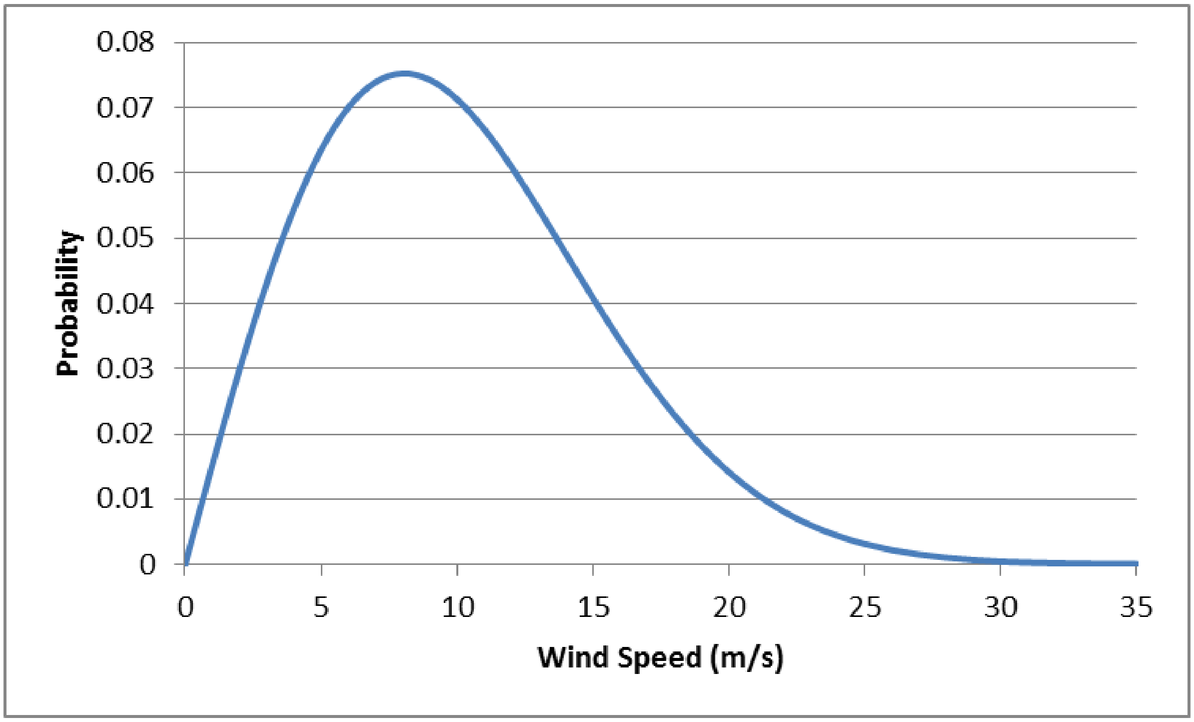

Figure 75. Wind speed versus Probability

6.2.5 Power Coefficient Matrix

Similar to the O&M matrix, the power coefficient matrix inputs the state matrix and a matrix that indicates the power coefficients at each state. The output is a power coefficient matrix. Table 4 shows the power coefficient matrix values for the baseline case.

Table 4. Power coefficient matrix for baseline case

State	Power Coefficient
1	0.45
2	0.4
3	0.36
4	0

6.2.6 AEP – Annual Energy Production

The inputs for the annual energy production are the power coefficient matrix and the air density calculated using equation 21 where p is the pressure at the hub height, M is the molar mass of dry air, R is the ideal gas constant, and T is temperature at the hub height. Equation 22 shows the calculation for the hourly energy production. As seen in equation 22, the power is calculated using the density (ρ), wind speed (V), and power coefficient (C_p) for each hour.

$$\rho = \frac{pM}{RT} \quad (21)$$

$$P_T = \frac{1}{2}\rho A V^3 C_p \quad (22)$$

6.2.7 Levelized Operations & Maintenance Cost

Both the O&M matrix and the Power Coefficient matrix are summed to obtain the yearly O&M costs and annual energy production. The O&M yearly costs are divided by the AEP to obtain the O&M Costs in $/MWh/yr. These values are calculated for the blades with and without the structural health monitoring (SHM). The resulting cost savings comes from subtracting the SHM costs from the Non-SHM costs to determine the savings of having the system.

6.2.8 Cost Model Assumptions

There were several assumptions for this model which are listed below. First, the blade is repaired when the defect is detected which means that the probability of detection is also the repair rate. For simplicity, pitch error and shear web disbond are considered equally likely in these initial calculations to exercise the model. As stated earlier, the wind was modeled as a Weibull distribution since it has been accepted as a good wind profile in the literature. Although a state space system is used, each increment is assumed to be one hour. In addition, the probabilities (rate of degradation) remains constant throughout the simulation since a transition matrix is used. This assumption is reasonable since many products have a constant useful life as seen in Figure 65. The average time for a repair is assumed to be one hour which corresponds well to Sandia's CREW estimate of one hour and fifteen minutes [39]. There are four states assumed as described in section 6.2.1.

6.3 Cost Model Simulation Methods

6.3.1 Cost Model Input Values

A summary table of the cost model input values is shown below in Table 5. The first category is noted as reliability and it is the probability that a turbine currently in state 1 will remain in state 1. A more reliable wind turbine will have a higher state 1 probability, while a less reliable wind turbine will have a lower state 1 probability. The O&M costs have been scaled with a total failure (State 4) noted at a value of 100 (100%) and can be refined later using actual costs. The power coefficient values are the power coefficient responding with each state. The power coefficient is at its maximum for state 1 and 0 for state 4 since no power will be generated if the rotor must be parked due to a failure. The probability of detection is also the repair rate since one of the assumptions is to repair the blade when the defect is found. This means that a higher probability of detection (repair rate) may have more repairs. All of these assumptions will be revisited as the model is matured and also due to changing conditions for different site location characteristics, different turbine characteristics, and variation in maintenance strategies.

Table 5. Cost Model Input Values Table

	State 1	State 2	State 3	State 4
Reliability	.75-L, .88-B, .9-H	NA	NA	NA
Operations & Maintenance Costs	0	10-L, 30-B, 50-H	50-L, 72.5-B, 95-H	100
Power Coefficient	0.45	.35-L, .4-B, .44-H	.29-L, .36-B, .43-H	0
Probability of Detection (Non CM)	NA	0.75	0.85	0.95
Probability of Detection (CM)	NA	.8-L, .95-B, .98-H	.88-L, .98-B, .99-H	.9-L, .99-B, 1-H

L=”Low”, B=“Baseline”, H=“High”

6.3.1 Cost Model Sample

In this section, a sample set of conditions is used to demonstrate how the model calculates the yearly levelized O&M costs for the baseline case. Table 6 shows a sample set of random numbers generated for the first five hours of a year. The first hour of each year defaults to state 1; therefore, a random number is not needed for the first hour.

Table 6. Random numbers for sample set

Hour	Random Number
1	NA
2	0.913
3	0.885
4	0.617
5	0.980

Both the Non-SHM and SHM cumulative assumed transition matrices are shown below in Table 7.

Table 7. Cumulative Transition Matrices

Non-SHM CumulativeMatrix

0.88	0.95	0.996	1
0.75	0.925	0.985	1
0.85	0.85	0.985	1
0.96	0.96	0.96	1

SHM Cumulative Matrix

0.88	0.95	0.996	1
0.95	0.985	0.997	1
0.98	0.98	0.998	1
0.99	0.99	0.99	1

Table 8 shows the resulting states for the first 5 hours of the sample case. Note that the SHM system detects the defect during hour 2.

Table 8. State matrices for sample set

Hour	Non-SHM State	SHM State
1	1	1
2	2	2
3	2	1
4	1	1
5	3	3

The state matrix is used to create a power coefficient matrix. As seen in Table 9 below, all of the state 1 values are changed to .45, all of the state 2 values are changed to .4 and all of the state 3 values are changed to .36.

Table 9. Power Coefficient matrices for sample set

Hour	Non-SHM State	Non-SHM Power Coeff
1	1	0.45
2	2	0.4
3	2	0.4
4	1	0.45
5	3	0.36

Hour	SHM State	SHM Power Coeff
1	1	0.45
2	2	0.4
3	1	0.45
4	1	0.45
5	3	0.36

This power coefficient matrix is combined with the random Weibull wind profile to determine the hourly energy production for each hour of the year. As noted earlier in section 6.2.3, the state matrix is also used to create an O&M cost matrix that is dependent upon the level or repair. In the sample set, there was one repair from state 2 to state 1. This corresponds to a value of 30 in the O&M costs matrix. The other values are 0 since there is no cost incurred unless there is a repair. The yearly O&M costs are then divided by the AEP to obtain the LRC.

6.4 Cost Model Simulation Results

6.4.1 Results as percent cost savings

As seen in Table 3, the input parameters such as O&M costs and performance coefficients were varied between baseline, low, and high values. The results from this cost sensitivity analysis can be seen in Figures 76-78 for the baseline, low, and high reliability cases. The results have been changed to percent change to facilitate comparison. The percent savings is calculated by subtracting the ratio of the SHM output divided by the Non-SHM output from 1. Figure 76 is the cost savings analysis for the baseline reliability case and the baseline percent savings is 2.68% per year for each turbine. Section 6.4.2 shows how this percentage can be used to obtain an annual cost savings estimate for each turbine using cost averages published by the National Renewable Energy Laboratory (NREL).

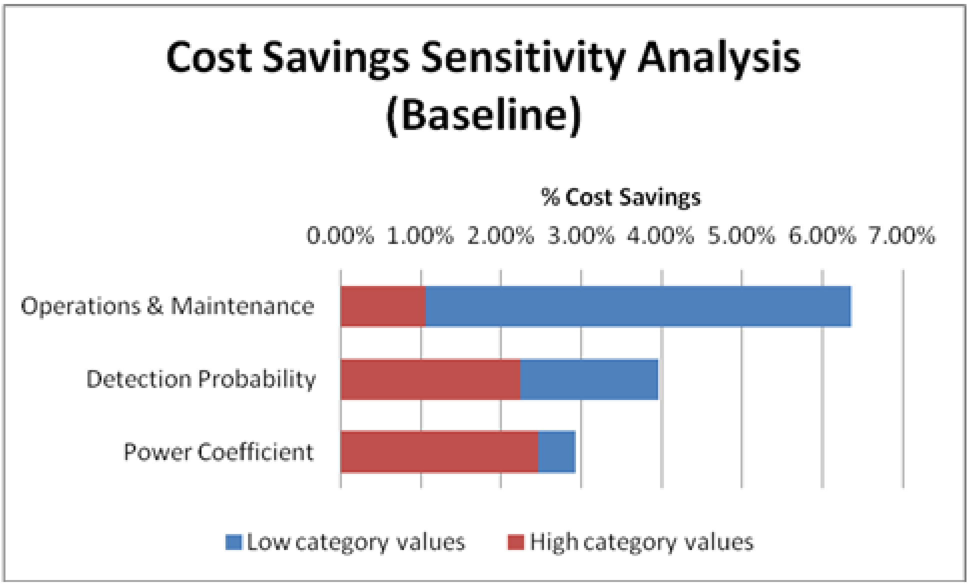

Figure 76. Cost Savings Sensitivity Analysis Results- Baseline Case

Figure 77 is the cost savings analysis for the baseline reliability case and the baseline percent savings is 3.42% per year for each turbine.

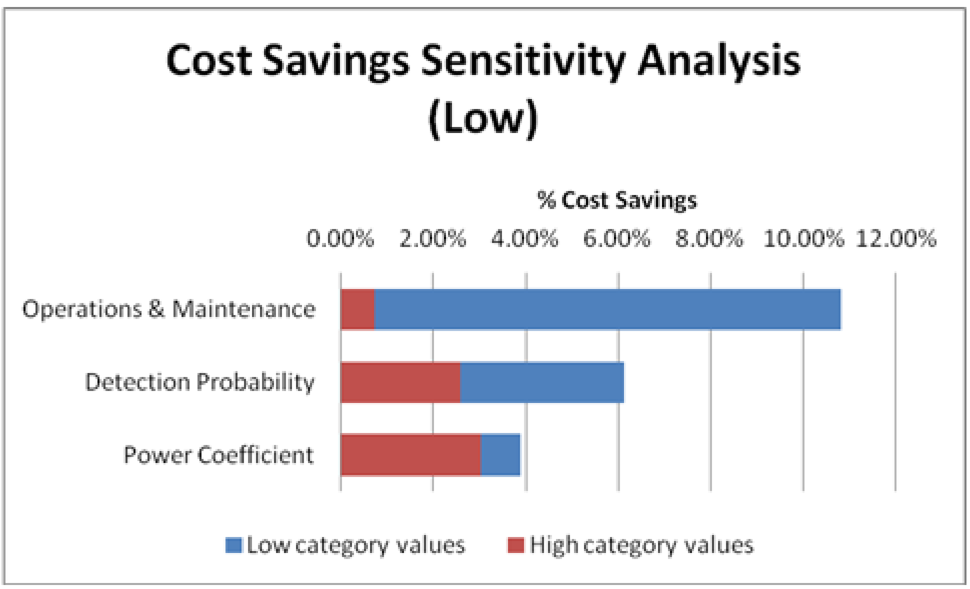

Figure 77. Cost Savings Sensitivity Analysis Results- Low Reliability Case

Figure 78 is the cost savings analysis for the baseline reliability case and the baseline percent savings is 4.19% per year for each turbine.

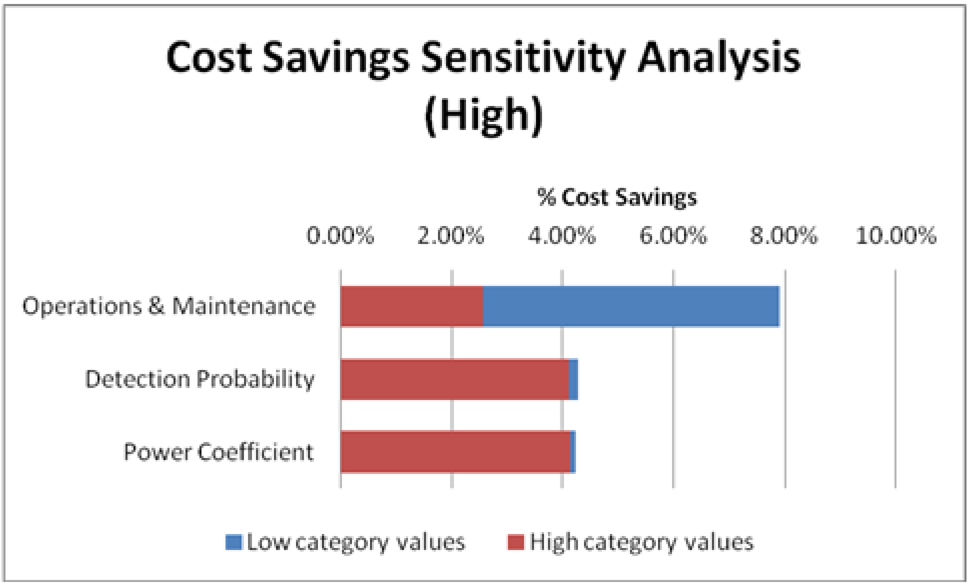

Figure 78. Cost Savings Sensitivity Analysis Results- High Reliability Case

All of the cost savings sensitivity analyses had the same trend of increasing cost savings for lower O&M costs, lower detection probabilities (repair rates), and lower power coefficient values.

6.4.2 Results using NREL values

The 2010 Cost of Wind Energy Review was used to determine estimates of cost savings for the baseline reliability case [40]. Only the LRC and O&M costs are considered for the model since they are the only parameters in the cost of energy equation that are affected by the SHM system. Table 10 shows all of the values used to determine the yearly LRC and O&M costs for the blades of a 5MW offshore wind turbine. The LRC & O&M costs for the blades was determined to be 7% of the total from the 2011 Sandia CREW benchmark results showing 7% unavailability due to blade failures [38].

Table 10. NREL values for estimate

NREL 2010 Cost of Wind Energy	Values
Offshore Levelized replacement cost	$40/kW/yr
Offshore Labor, equipment, facilities (O&M)	$46/kW/yr
Yearly LRC & O&M for 5 MW	$ 430,000
7% of Yearly LRC & O&M for 5 MW	$ 30,100

The yearly cost of $30,100 is then taken to be the cost for the Non-SHM system. With a percent savings of 2.68%, the SHM system will yield an $807/yr per turbine cost benefit over the Non-SHM system.

6.5 Summary of CM System Cost Benefit

This section contains the preliminary analysis summary using the cost benefit model. The current model produced a good initial analysis of the cost benefits for the SHPM system, showed cost trends, and highlighted parameters that should be further investigated. All of the cases used in this study resulted in a cost savings with the SHPM system. With more accurate operations and maintenance costs from the field, the model can be refined to yield better cost savings estimates. The trends that were observed with the sensitivity analysis were O&M COE was most sensitive to the O&M repair and replacement costs followed by the level of detection (point at which the blade is repaired). The O&M COE was the least sensitive to changes in the performance coefficient. All of these results show a greater cost savings at the lower values of these parameters. These sensitivity analysis results show that obtaining field data is very important since the initial results show a strong sensitivity of the resulting cost savings to the repair costs. Including the actual time to repair can further refine the cost model since averages have been used. Further development of the cost model can be accomplished by incorporating factors such as seasonal affects and multiple decisions. Seasonality can affect the cost savings since offshore wind farms have periods when performing maintenance can be difficult or impossible. Decisions such as derating the turbine can extend the life of the blade and reduce the occurrence of unscheduled maintenance. In addition, deciding to wait to perform maintenance can also produce an additional cost savings. This initial cost model has provided insight about the potential cost savings of the proposed SHM system and further work will be done to improve the model.

7. CONCLUSIONS

A multi-scale simulation of damage methodology has been expanded for the investigation and development of SHPM methods for offshore wind turbine blades. Two cases studies were performed to further demonstrate the methodology in analyzing the sensitivity of blade damage in the operating response of the rotor. The method utilizes the propagation of damage from a high fidelity component level model up to a reduced order model of a full turbine so that the changes in the turbine's operational responses due to the damage can be examined. Furthermore, these full turbine simulations can be used to replicate fault mechanisms such as pitch error and estimate the loads on the turbine blades which can then be propagated back to the high fidelity model to allow for further local analyses to be conducted. By investigating the effects of damage on multiple scales, the developed methodology takes advantage of available software to investigate the underlying physical consequences of damage/faults on both a local and global level which leads to the identification of operational responses that are most sensitive to these physical changes.

This document has described the application of the developed methodology to investigate the effects of rotor imbalance and a shear web disbond on an offshore 5-MW wind turbine. The 61.5 meter blade model was developed in SNL's NuMAD software and exported to ANSYS where the shear web disbond was simulated by separating the nodes of the shear web from the blade at the location of the disbond. The reduced order blade models with varying levels of damage were included into a model of an offshore turbine on a fixed monopole in 20 meters of water. The response of these offshore turbine models with varying levels of damage/imbalance was then simulated in FAST. From these simulations it was apparent that the measurements which were the most sensitive to the present and extent of the shear web disbond or pitch error were the blade tip accelerations and the root pitching moments. The aerodynamic loads from the FAST simulations were calculated and applied to the high fidelity ANSYS model which also demonstrated an increased blade tip deflection and increased localized strains due to the presence of a shear web disbond.

To examine how the structural health of each turbine could be used to optimize the operation and maintenance practices of an offshore wind plant, an initial cost model was developed and used to investigate the operations and maintenance costs due to the fault/damage. The combination of the repair cost information and the structural health of each turbine could be utilized in the optimization of damage mitigating control strategies and maintenance schedule to reduce the operations and maintenance costs associated with running an offshore wind energy plant.

8. FUTURE WORK

In FY13, the presently reported work of FY12 documented in this report will be expanded including further integration of the sensitivity of damage study with the cost analysis. A cost benefit analysis of SHPM systems including an assessment of uncertainty of the SHPM system to important sources of variability (including inflow and sensor options). The expanded cost model will use a larger set of representative parameters so that the SHPM cost benefit figures are more realistic. Laboratory experiments to validate the detection strategies outlined in the report will be pursued.

9. REFERENCES

[1] A.C. Levitt, W. Kempton, A.P. Smith, W. Musial and J. Firestone, "Pricing offshore wind power." *Energy Policy* (In Press) 2011.

[2] W. Musial and B. Ram, *Large-Scale Offshore Wind Energy for the United State: Assessment of Opportunities and Barriers*, NREL Report No. TP-500-49229, Golden, CO, September 2010.

[3] U.S. Department of Energy, *A National Offshore Wind Strategy: Creating an Offshore Wind Energy Industry in the United States*, Washington: Wind & Hydropower Technologies Program Report No. 5040, February 2011.

[4] R. Wiser and M. Bolinger, *2010 Wind Technologies Market Report*, Lawrence Berkeley National Laboratory: Lawrence Berkeley National Laboratory. LBNL Paper LBNL 4820E, June 2011.

[5] B. Snyder and M.J. Kaiser, "Ecological and economic cost-benefit analysis of offshore wind energy." *Renewable Energy* 34(6), pp. 1567-1578, 2009.

[6] G. van Bussel, A.R. Henderson, C.A. Morgan, B. Smith, R. Barthelmie, K. Argyriadis, A. Arena, G. Niklasson, and E. Peltola, "State of the Art and Technology Trends for Offshore Wind Energy: Operation and Maintenance Issues," *Offshore Wind Energy EWEA Special Topic Conference*, Brussels, Belgium, December 2001.

[7] L.W.M.M. Rademakers, H. Braam, M.B. Zaaiger, and G.J.W. van Bussel, "Assessment and optimisation of operation and maintenance of offshore wind turbines," in *Proceedings of the European Wind Energy Conference*, Madrid, Span, June 2003.

[8] Y. Amirat, M.E.H Benbouzid, B. Bensaker, and R. Wamkeue, "Condition monitoring and fault diagnosis in wind energy conversion systems: a review." In *Proceedings 2007 IEEE International Electric Machines and Drives Conference*, Vol 2., pp. 1434-1439, 2007.

[9] J. Nilsson and L. Bertling, "Maintenance management of wind power systems using condition monitoring systems – Life cycle cost analaysis for two case studies," *IEEE Transactions on Energy Conversion* 22(1), pp. 223-229, 2007.

[10] C.C. Ciang, J.R. Lee, and H.J. Bang, "Structural health monitoring for a wind turbine system: a review of damage detection methods." *Measurement Science and Technology* 19(12), pp. 1-20, 2008.

[11] F. Besnard, K. Fischer, and L. Bertling, "Reliability-centred asset maintenance – A step towards enhanced reliability availability and profitability of wind power plants" in *2010 IEEE PES Innovative Smart Grid Technologies Conference Europe (ISGT Europe)*, 2010.

[12] Z. Hameed, S.H. Ahn, and Y.M. Cho, "Practical aspects of a condition monitoring system for a wind turbine with emphasis on its design, system architecture, testing and installation," *Renewable Energy*, 35(5), pp. 879-894, May 2010.

[13] NWTC Design Codes (FAST by Jason Jonkman, Ph.D.). http://wind.nrel.gov/designcodes/simulators/fast/. Last modified 05-November-2010; accessed 05-November-2010.

[14] R.R. Ryan, ADAMS – Multibody System Analysis Software, Multibody Systems Handbook. Berlin: Springer-Verlag, 1990.

[15] J. Jonkman, S. Butterfield, W. Musial, and G. Scott, "Definition of a 5-MW Reference Wind Turbine for Offshore System Development," NREL/TP-500-38060, Golden, CO: National Renewable Energy Laboratory, February 2009.

[16] D.T. Griffith, N. Yoder, B. Resor, J. White, and J. Paquette, "Structural Health and Prognostics Management for Offshore Wind Turbines: An Initial Roadmap," Sandia

National Laboratories Technical Report, SAND2012-10109, Sandia National Laboratories; Albuquerque, NM, Printed December 2012.
[17] J. Jonkman and L. Buhl, “FAST User’s Guide,” NREL/EL-500-38230, Golden, CO: National Renewable Energy Laboratory, August 2005.
[18] J. Losi, and E. Becker, "Imbalance: A danger to components," Erneuerbare Energien, August 2009.
[19] J. Giebhardt and WP7 Partners, “Condition Monitoring for Wind Turbines ‘State of the Art’ Report,” Kassel, Germany: European Commission, 2007.
[20] J. Niebsch, R. Ramlau, and T. Nguyen, "Mass and Aerodynamic Imbalance Estimates of Wind Turbines," Energies, 2010: 696-710.
[21] M. Adams, Jr., Rotating Machinery Vibration. New York, NY: Marcel Dekker, 2001.
[22] J.P. Borg R.H. Kirchoff, "The Effects of Static and Dynamic Imbalance on a Horizontal Axis Wind Turbine," Journal of Solar Energy Engineering (ASME) 119 (1997): 261-262.
[23] B. Petersen, et al., “Evaluate the Effect of Turbine Period of Vibration Requirements on Structural Design Parameters: Technical Report of Findings,” Technical Report, Groton, CT: Applied Physical Sciences, 2010.
[24] M. MaCamhaoil, “Bruel & Kjaer Application Notes: Static and Dynamic Balancing of Rigid Rotors,” n.d. http://www.bksv.com/doc/bo0276.pdf (accessed March 2012).
[25] P. Caselitz and J. Giebhardt, "Rotor Condition Monitoring for Improved Operational Safety of Offshore Wind Energy Converters," ASME Journal of Solar Energy Engineering (ASME Journal of Solar Energy Engineering), 2005: Vol. 127 (261).
[26] IRD Balancing, Balance Quality Requirements of Rigid Rotors - The Practical Application of ISO 1940/1, Louisville, KY: IRD Balancing, 2009.
[27] Moog Incorporated, Rotor Monitoring Systems, June 2011. http://www.moog.com/literature/ICD/Moog-Wind-Rotor-Monitoring-System-Overview-en.pdf (accessed March 13, 2012).
[28] J.P. Borg and R.H. Kirchoff, "Mass and Aerodynamic Imbalance of a Horizontal Axis Wind Turbine," Journal of Solar Energy Engineering 120 (Feburary 1998): 66-74.
[29] IEC 61400-1, “Wind turbine generator systems-Part 1: Safety requirements,” 2nd edition, Geneva, Switzerland: International Electrotechnical Commission, 1999.
[30] B.J. Jonkman and L. Kilcher, “TurbSim User’s Guide: Version 1.06.00,” NREL/TP-xxx-xxxx (Draft Version), Golden, CO: National Renewable Energy Laboratory, September 2012.
[31] C. A. Walford, Wind turbine reliability: understanding and minimizing wind turbine operation and maintenance costs: United States. Department of Energy, 2006.
[32] M. I. Blanco, "The economics of wind energy," Renewable and Sustainable Energy Reviews, vol. 13, pp. 1372-1382, 2009.
[33] K. Fernandes and K. Marais, "Value of Energy Model," ed, 2012.
[34] A. Olson, M. Chait, and A. Pacheco, "Wind Costing Model," State of Wyoming Revenue Committee of the State Legislature, http://legisweb.state.wy.us/2010/WyomingWindModel_7_01_2010.pdf2010.
[35] Vachon, W. (2002). “Long-Term O&M Costs of Wind Turbines Based on Failure Rates and Repair Costs.” Presented at Windpower 2002, American Wind Energy Association, Annual Conference, June 2-5.
[36] E. Byon and Y. Ding, "Season-dependent condition-based maintenance for a wind turbine using a partially observed Markov decision process," Power Systems, IEEE Transactions on, vol. 25, pp. 1823-1834, 2010.
[37] P. O'Connor and A. Kleyner, Practical reliability engineering: Wiley, 2011.

[38] J. Ribrant, "Reliability performance and maintenance, a survey of failures in wind power systems," Unpublished doctoral dissertation, XR-EE-EEK, 2006.
[39] V. Peters, B. McKenney, A. Ogilvie, and C. Bond, "Continuous Reliability Enhancement for Wind (CREW) Database," Sandia National Laboratories, 2011.
[40] S. Tegen, M. Hand, B. Maples, E. Lantz, P. Schwabe, and A. Smith, "2010 Cost of Wind Energy Review," National Renewable Energy Laboratory2012.
[41] Y. Nam, T. Yoon, K. Kim, and H. Cuong, 41. “Estimation of a Nacelle Dynamic Motion of a Wind Turbine,” *Contorl, Automation, Robotics and Vision, 2008, ICARCV 2008. 10th International Conference on* , pp. 1017-1020, 2008.

DISTRIBUTION:

5 Cecelia Sterling
Office of Wind and Hydropower Technologies
EE-2B Forrestal Building, U.S. DOE
1000 Independence Ave. SW
Washington, DC 20585

5 Professor Douglas Adams, Purdue University
Purdue Center for Systems Integrity
1500 Kepner Drive
Lafayette, IN 479905

5 Library NWTC
NREL/NWTC
1617 Cole Boulevard
Golden, CO 80401

Internal Distribution

10	MS1124	D.T. Griffith	Org. 6122
10	MS1124	Wind Library	Org. 6121
1	MS0899	Technical Library	9536 (electronic copy)

Sandia National Laboratories